Advancing Neuroimaging-Based Brain Network Models in Neurodegenerative Diseases

Doctoral thesis

to obtain a doctorate (PhD)

from the Faculty of Medicine

of the University of Bonn

Riccardo Leone

from Borgomanero, Italy

2026

Written with authorization of

the Faculty of Medicine of the University of Bonn

First reviewer: Prof. Dr. Med. Xenia Kobeleva

Second reviewer: Prof. Dr. Med. Henning Boecker

Day of oral examination: 27/02/2026

From the Department of Neurology, Medical Faculty, University Hospital Bonn

Table of Contents

List of abbreviations

Aβ	Amyloid-Beta
AD	Alzheimer's Disease
ADAD	Autosomal Dominant Alzheimer's Disease
CSF	Cerebrospinal Fluid
CSVD	Cerebrovascular Disease
EEG	Electroencephalography
FLAIR	Fluid-attenuated Inversion Recovery
fMRI	Functional Magnetic Resonance
MEG	Magnetoencephalography
MRI	Magnetic Resonance Imaging
PET	Positron Emission Tomography
PVS	Perivascular spaces
Rs	Resting-state
SWS	Slow wave sleep
WM	White Matter
WMH	White Matter Hyperintensities

1. Abstract

In this thesis I contribute to the broader scientific effort of advancing neuroimaging-based brain network models for neurodegenerative diseases, with a particular focus on Alzheimer's disease (AD). First, I provide novel insights on the multifactorial and heterogeneous pathophysiology of AD by investigating the role of co-occurring pathologies (e.g., cerebrovascular disease, CSVD). Second, I introduce these concepts into brain network models. By doing so, I advance our current understanding of the impact of co-pathologies on functional brain activity, providing information needed to build more biologically realistic brain network models.

In the first project, I demonstrate that alterations in perivascular spaces - an emerging biomarker of CSVD – are observed in young individuals with a genetic form of AD. This finding suggests that CSVD is an intrinsic feature of AD rather than a coincidental consequence of aging. In the second project, I show in a cohort of late-onset AD the crucial role that white matter hyperintensities – a key biomarker of CSVD - have on cortical neurodegeneration. These insights confirm the role of CSVD in AD, beyond traditional AD biomarkers, such as amyloid and tau. In the third project, using a brain network model, I demonstrate the detrimental effect of white matter hyperintensities on global brain network communication in wakeful resting-state. In the fourth project, I show that a reduction in inter-hemispheric white matter connectivity, which is commonly observed in aging, AD, and CSVD, explains brain alterations observed during slow-wave sleep.

By providing novel insights into the complex and multifactorial nature of AD pathophysiology and by introducing these newly developed concepts into brain network models, this thesis effectively advances their biological plausibility. This step is needed to increase the overall reliability of these models, which will help to translate them from the laptop to the bedside. An effective clinical translation of brain network models could potentially provide new tools to improve diagnosis, prognosis and treatment personalization in neurodegenerative diseases.

2. Introduction and aims with references

Neurodegenerative diseases represent a growing public health challenge, driven largely by an aging global population (Knopman et al., 2021). Among them, Alzheimer's disease (AD) is the most prevalent, accounting for most dementia cases worldwide. Despite its prevalence, and although recently introduced therapies targeting amyloid accumulation have sparked hope to slow its development, AD still does not have a definitive cure. A possible reason for this lack of a curative treatment is that the pathophysiology of AD is still incompletely understood. Biomarkers assessing amyloid and tau have improved diagnostic precision, yet they do not fully capture the complex heterogeneity of the disease, which also involves other pathologies (co-pathologies) (Karanth et al., 2020). Novel neuroimaging-based computational approaches (brain network models) offer a promising avenue for bridging the gap between biological mechanisms and functional alterations observed in AD. These models allow us to realistically simulate the activity of the brain across different brain states (e.g., wakefulness, sleep) and to integrate multimodal imaging information on pathology. Therefore, brain network models have the potential to allow us to better understand the multifactorial nature of AD, and to build novel diagnostic and prognostic tools that could be translated to the clinic.

2.1 On the multifactorial nature of Alzheimer's disease pathogenesis

The leading hypothesis of AD pathogenesis is the "amyloid cascade" hypothesis, which posits that the accumulation of misfolded amyloid-beta (Aβ) initiates a sequence of events leading to the deposition of tau tangles and subsequent neurodegeneration in specific brain regions (Knopman et al., 2021). While this hypothesis has shaped decades of research, it has increasingly been criticized for failing to account for the heterogeneity and complexity of the disease (Frisoni et al., 2022). Notably, many individuals with AD also exhibit additional brain pathologies, in addition to amyloid and tau (Karanth et al., 2020). These co-pathologies - such as TDP-43, α-synuclein, and cerebral small vessel disease (CSVD) (Karanth et al., 2020) - may act synergistically or independently of amyloid and tau in driving neurodegeneration and brain network dysfunction. Among them,

CSVD is particularly prevalent (Ter Telgte et al., 2018). CSVD primarily affects small cerebral arterioles, leading to impaired blood flow, blood–brain barrier dysfunction, and abnormal fluid clearance through perivascular spaces (PVS) (Wardlaw et al., 2019). Although small brain vessels themselves cannot be visualized directly in vivo, CSVD can be inferred using MRI markers such as white matter hyperintensities (WMH) and alterations in PVS (Duering et al., 2023). WMH appear as regions of increased signal on fluid-attenuated inversion recovery (FLAIR) and T2-weighted images, typically reflecting chronic ischemic damage to the white matter (WM). PVS are fluid-filled spaces that surround small penetrating vessels and appear as tubular-shaped hypointense structures on T1-weighted images (Duering et al., 2023). These microvascular changes are often associated with tissue injury, mostly involving the WM, and may contribute to neurodegeneration and brain network dysfunction (Ter Telgte et al., 2018). However, the precise mechanisms linking WM damage and CSVD to alterations in brain structure (e.g., brain atrophy) and function (e.g., functional connectivity patterns), and how these effects interact with amyloid and tau pathology, remain poorly understood.

2.2 Brain network dysfunction in AD

AD is characterized by large-scale brain network dysfunction that manifests both during resting wakefulness and sleep (Pievani et al., 2014). Resting-state-fMRI (rs-fMRI) studies show variable functional connectivity changes depending on disease stage (Pievani et al., 2014). Increased functional connectivity may be observed in the early stages of mild cognitive impairment, while reduced connectivity within the default mode network and impaired inter-network connectivity occur as the disease progresses to the dementia stage (Pievani et al., 2014). These changes are associated with amyloid-β deposition in default-mode network hubs and tau accumulation in medial temporal regions (Pievani et al., 2014). Beyond wakefulness, AD is characterized by alterations in the generation and propagation of slow oscillations during non-REM sleep (slow wave sleep, SWS). Aging-related neurodegeneration and WMH, particularly involving inter-hemispheric WM tracts, may exacerbate network alterations during wake

and sleep by amplifying the breakdown of large-scale brain synchrony (Lavanga et al., 2023). However, the precise mechanisms linking WM damage to the observed brain network dysfunction are still unclear. Addressing this gap requires computational brain network models, which provide a mechanistic framework to test how different pathological processes may drive network alterations in AD.

2.3 Brain network models allow to reproduce empirical brain activity

Brain network models are a promising tool to understand how WM alterations, such as those linked to CSVD, are linked to brain network dysfunction. Brain network models allow us to realistically simulate, in-silico, the dynamic activity of the brain observed empirically across various modalities, such as electroencephalography (EEG) and rs-fMRI both during wakefulness and sleep (Deco et al., 2019; Sanz-Leon et al., 2015). The process of building brain network models begins by parcellating the brain into distinct regions using anatomical or functional criteria, typically guided by a brain atlas. These regions are then interconnected via a structural connectivity matrix, which quantifies the density of WM fibers linking each pair of regions, as derived from diffusion-weighted imaging. To simulate neural activity over time, a mathematical model is assigned to each region, capturing its local dynamics. Regional activities are then coupled through the structural connectivity matrix, which determines how strongly each brain region influences others. The potential of brain network models to understand mechanisms underlying brain function has been already shown in healthy individuals (Deco et al., 2011). For instance, they have been used to explore how structural connectivity shapes functional connectivity (Honey et al., 2009), how spatial and temporal scales influence information transmission (Kobeleva et al., 2021), and to simulate transitions between brain states such as wakefulness and sleep (Deco et al., 2019). However, these models allow a further mechanistic way to connect biological observables (e.g., accumulation of pathological proteins) with brain structure and function. Therefore, recent studies have started to use brain network models to evaluate hypotheses regarding how pathological changes may influence brain activity in AD.

2.4 Brain network models in Alzheimer's disease

By weighting regional model parameters based on biological observables (e.g., amyloid and tau), previous studies have bridged scales between AD pathology and functional alterations. Brain network models incorporating information about the heterogenous distribution of amyloid and tau into heterogeneous model parameters reproduce empirical brain activity more realistically compared to unweighted or homogeneously weighted models (Patow et al., 2023; Stefanovski et al., 2019). These weighted models have provided in-vivo support for the hypothesis that amyloid-induced hyperexcitability is responsible for functional alterations observed in early AD patients in various modalities, such as MEG (van Nifterick et al., 2022), EEG (Sanchez-Rodriguez et al., 2024; Stefanovski et al., 2019) and fMRI (Patow et al., 2023). Additionally, using brain network models whose regional parameters were weighted either on amyloid, tau, or a combination of the two, Patow et al. (2023) showed that amyloid-induced effects are confined to the initial disease stages, while tau-related effects predominate when dementia ensues. Parameters obtained from brain network models may assist with AD diagnosis, since they have been associated with cognitive scores (Zimmermann et al., 2018) and AD plasma biomarkers (Sanchez-Rodriguez et al., 2024). Furthermore, brain network models may provide a useful tool for testing potential treatments for AD in silico. For example, de Haan et al. (2017) used a brain network model to theoretically test how treatment strategies involving the modulation of the excitation/inhibition balance may slow down AD-typical network degeneration. Similarly, Stefanovski et al (2019) used a brain network model to mimic the effects of memantine, an NMDA-receptor antagonist, showing how this drug may revert the typical oscillatory slowing observed in late-stage AD. However, previous research has only focused on traditional AD-related biomarkers, overlooking the pathological heterogeneity of AD, particularly regarding co-pathologies. Therefore, the impact of co-pathologies, such as CSVD, in shaping functional alterations in AD is still unclear. This is an important limitation, as overlooking the high prevalence of co-pathologies means current models may fail to capture the full biological complexity of AD, thus reducing their clinical utility for diagnostic and prognostic purposes.

2.5 Aims

The overall aims of this work are to investigate the role of co-pathologies, particularly CSVD, in the multifactorial pathophysiology of AD and to integrate these pathological mechanisms to advance the biological realism of brain network models. The sections that follow detail the specific aims of the individual projects included in this thesis.

2.5.1 Project 1: Is CSVD an intrinsic component of AD pathogenesis?

CSVD is commonly observed in aging-associated AD. However, it is currently unknown if CSVD is an intrinsic component of AD pathogenesis or a co-occurring phenomenon due to aging. In this study, I considered a sample of individuals with a genetic autosomal dominant form of AD (ADAD), who develop dementia at a young age. While limited previous work has explored WMH as a CSVD biomarker in ADAD, PVS - another key marker of small vessel pathology - have not yet been investigated. Here I compared PVS characteristics between mutation carriers and non-carrier family members. Based on previous work on late-onset AD (Barisano et al., 2025), I hypothesized that mutation carriers would show fewer but enlarged PVS compared with non-carriers, and that PVS metrics would be associated with amyloid and tau. This study provides evidence that CSVD is not a mere co-pathology, but an intrinsic pathophysiological process in AD. This suggests an even greater relevance for modeling its effects on brain structure and function.

2.5.2 Project 2: Is CSVD-linked WM damage associated with neurodegeneration beyond amyloid and tau?

The amyloid cascade hypothesis posits a linear progression in AD pathogenesis, with amyloid and tau driving neurodegeneration. Evidence from Project 1 and other studies suggest that CSVD, especially WMH, may independently contribute to neurodegeneration. In this study, I hypothesized that WMH would be associated with reduced cortical thickness, particularly in AD-vulnerable temporal brain regions. I tested the association between WMH and cortical thinning using cross-sectional and longitudinal MRI and positron emission tomography (PET) data from more than 500 individuals. Using linear regression for cross-sectional and linear

mixed models for longitudinal data, I also tested whether the association between WMH and cortical thinning depended on whole-brain diffuse cerebrovascular processes or tract-specific axonal damage. This study provides information on the effects of CSVD on neurodegeneration and its link with amyloid and tau.

2.5.3 Project 3: How does WM damage influence brain dynamics during awake resting-state?

As shown in Project 2, WMH play a key role in driving neurodegeneration through pathological processes affecting the whole brain. In this study, I investigated the effects of WMH on brain network dynamics using a brain network model. As in the previous study, I hypothesized that WMH could lead to brain network dysfunction either through whole-brain diffuse cerebrovascular processes or via tract-specific axonal damage. To test this hypothesis, I built a brain network model (i.e., the Hopf model) and combined it with a virtual-lesioning (disconnectome) approach. This disconnectome approach allows to map the effects of focal WM lesions onto specific WM tracts and the cortical regions they connect to, thereby tracing how localized structural damage propagates at the brain network level. This study provides information on how CSVD-linked structural WM damage leads to alterations in brain network activity in early AD. This study lays the groundwork for incorporating the effects of CSVD into more realistic brain network models of AD.

2.5.4 Project 4: How does WM damage impact slow wave sleep?

Results from Project 3 suggest a role for WM damage in influencing brain activity during awake resting state. Disrupted slow wave sleep (SWS) is another prominent finding in aging and AD. In this study, we hypothesized that inter-hemispheric WM damage, commonly observed in aging and AD, and exacerbated by CSVD, could explain SWS alterations. First, I collaborated in creating a brain network model able to accurately replicate physiological sleep slow waves. Then, a simulation of the effects of increasing levels of WM damage was obtained by reducing the strength of inter-hemispheric connections. This study provides valuable information connecting structural WM damage to sleeping alterations

seen in aging and AD, showing that brain network models can reproduce pathological alterations observed across different brain states.

2.6 References

Barisano, G., Iv, M., Choupan, J., Hayden-Gephart, M., Weiner, M., Aisen, P., Petersen, R., Jack, C. R., Jagust, W., Trojanowki, J. Q., Toga, A. W., Beckett, L., Green, R. C., Saykin, A. J., Morris, J., Shaw, L. M., Liu, E., Montine, T., Thomas, R. G., … Raj, B. A. (2025). Robust, fully-automated assessment of cerebral perivascular spaces and white matter lesions: A multicentre MRI longitudinal study of their evolution and association with risk of dementia and accelerated brain atrophy. eBioMedicine, 111, 105523. https://doi.org/10.1016/j.ebiom.2024.105523

Deco, G., Cruzat, J., Cabral, J., Tagliazucchi, E., Laufs, H., Logothetis, N. K., & Kringelbach, M. L. (2019). Awakening: Predicting external stimulation to force transitions between different brain states. Proceedings of the National Academy of Sciences, 116(36), 18088–18097. https://doi.org/10.1073/pnas.1905534116

Deco, G., Jirsa, V. K., & McIntosh, A. R. (2011). Emerging concepts for the dynamical organization of resting-state activity in the brain. Nature Reviews Neuroscience, 12(1), 43–56. https://doi.org/10.1038/nrn2961

Duering, M., Biessels, G. J., Brodtmann, A., Chen, C., Cordonnier, C., Leeuw, F.-E. de, Debette, S., Frayne, R., Jouvent, E., Rost, N. S., Telgte, A. ter, Salman, R. A.-S., Backes, W. H., Bae, H.-J., Brown, R., Chabriat, H., Luca, A. D., deCarli, C., Dewenter, A., … Wardlaw, J. M. (2023). Neuroimaging standards for research into small vessel disease—Advances since 2013. The Lancet Neurology, 22(7), 602–618. https://doi.org/10.1016/S1474-4422(23)00131-X

Frisoni, G. B., Altomare, D., Thal, D. R., Ribaldi, F., van der Kant, R., Ossenkoppele, R., Blennow, K., Cummings, J., van Duijn, C., Nilsson, P. M., Dietrich, P.-Y., Scheltens, P., & Dubois, B. (2022). The probabilistic model of Alzheimer disease: The amyloid hypothesis revised. Nature Reviews Neuroscience, 23(1), 53–66. https://doi.org/10.1038/s41583-021-00533-w

Haan, W. de, Straaten, E. C. W. van, Gouw, A. A., & Stam, C. J. (2017). Altering neuronal excitability to preserve network connectivity in a computational model of Alzheimer's disease. PLOS Computational Biology, 13(9), e1005707. https://doi.org/10.1371/journal.pcbi.1005707

Honey, C. J., Sporns, O., Cammoun, L., Gigandet, X., Thiran, J. P., Meuli, R., & Hagmann, P. (2009). Predicting human resting-state functional connectivity from structural connectivity. Proceedings of the National Academy of Sciences, 106(6), 2035–2040. https://doi.org/10.1073/pnas.0811168106

Karanth, S., Nelson, P. T., Katsumata, Y., Kryscio, R. J., Schmitt, F. A., Fardo, D. W., Cykowski, M. D., Jicha, G. A., Van Eldik, L. J., & Abner, E. L. (2020). Prevalence and Clinical Phenotype of Quadruple Misfolded Proteins in Older Adults. JAMA Neurology, 77(10), 1299–1307. https://doi.org/10.1001/jamaneurol.2020.1741

Knopman, D. S., Amieva, H., Petersen, R. C., Chételat, G., Holtzman, D. M., Hyman, B. T., Nixon, R. A., & Jones, D. T. (2021). Alzheimer disease. Nature Reviews Disease Primers, 7(1), Article 1. https://doi.org/10.1038/s41572-021-00269-y

Kobeleva, X., López-González, A., Kringelbach, M. L., & Deco, G. (2021). Revealing the Relevant Spatiotemporal Scale Underlying Whole-Brain Dynamics. Frontiers in Neuroscience, 15. https://www.frontiersin.org/articles/10.3389/fnins.2021.715861

Lavanga, M., Stumme, J., Yalcinkaya, B. H., Fousek, J., Jockwitz, C., Sheheitli, H., Bittner, N., Hashemi, M., Petkoski, S., Caspers, S., & Jirsa, V. (2023). The virtual aging brain: Causal inference supports interhemispheric dedifferentiation in healthy aging. NeuroImage, 283, 120403. https://doi.org/10.1016/j.neuroimage.2023.120403

Patow, G., Stefanovski, L., Ritter, P., Deco, G., Kobeleva, X., & for the Alzheimer's Disease Neuroimaging Initiative. (2023). Whole-brain modeling of the differential influences of amyloid-beta and tau in Alzheimer's disease. Alzheimer's Research & Therapy, 15(1), 210. https://doi.org/10.1186/s13195-023-01349-9

Pievani, M., Filippini, N., van den Heuvel, M. P., Cappa, S. F., & Frisoni, G. B. (2014). Brain connectivity in neurodegenerative diseases—From phenotype to proteinopathy. Nature Reviews Neurology, 10(11), 620–633. https://doi.org/10.1038/nrneurol.2014.178

Sanchez-Rodriguez, L. M., Bezgin, G., Carbonell, F., Therriault, J., Fernandez-Arias, J., Servaes, S., Rahmouni, N., Tissot, C., Stevenson, J., Karikari, T. K., Ashton, N. J., Benedet, A. L., Zetterberg, H., Blennow, K., Triana-Baltzer, G., Kolb, H. C., Rosa-Neto, P., & Iturria-Medina, Y. (2024). Personalized whole-brain neural mass models reveal combined Aβ and tau hyperexcitable influences in Alzheimer's disease. Communications Biology, 7(1), 528. https://doi.org/10.1038/s42003-024-06217-2

Sanz-Leon, P., Knock, S. A., Spiegler, A., & Jirsa, V. K. (2015). Mathematical framework for large-scale brain network modeling in The Virtual Brain. NeuroImage, 111, 385–430. https://doi.org/10.1016/j.neuroimage.2015.01.002

Stefanovski, L., Triebkorn, P., Spiegler, A., Diaz-Cortes, M.-A., Solodkin, A., Jirsa, V., McIntosh, A. R., Ritter, P., & for the Alzheimer's Disease Neuroimaging Initiative. (2019). Linking Molecular Pathways and Large-Scale Computational Modeling to Assess Candidate Disease Mechanisms and Pharmacodynamics in Alzheimer's Disease. Frontiers in Computational Neuroscience, 13. https://www.frontiersin.org/articles/10.3389/fncom.2019.00054

Ter Telgte, A., Van Leijsen, E. M. C., Wiegertjes, K., Klijn, C. J. M., Tuladhar, A. M., & De Leeuw, F.-E. (2018). Cerebral small vessel disease: From a focal to a global perspective. Nature Reviews Neurology, 14(7), 387–398. https://doi.org/10.1038/s41582-018-0014-y

van Nifterick, A. M., Gouw, A. A., van Kesteren, R. E., Scheltens, P., Stam, C. J., & de Haan, W. (2022). A multiscale brain network model links Alzheimer's disease-mediated neuronal hyperactivity to large-scale oscillatory slowing. Alzheimer's Research & Therapy, 14(1), 101. https://doi.org/10.1186/s13195-022-01041-4

Wardlaw, J. M., Smith, C., & Dichgans, M. (2019). Small vessel disease: Mechanisms and clinical implications. The Lancet Neurology, 18(7), 684–696. https://doi.org/10.1016/S1474-4422(19)30079-1

Zimmermann, J., Perry, A., Breakspear, M., Schirner, M., Sachdev, P., Wen, W., Kochan, N. A., Mapstone, M., Ritter, P., McIntosh, A. R., & Solodkin, A. (2018). Differentiation of Alzheimer's disease based on local and global parameters in personalized Virtual Brain models. NeuroImage. Clinical, 19, 240–251. https://doi.org/10.1016/j.nicl.2018.04.017

3. Publications

3.1 Publication 1: Alterations in MRI-visible perivascular spaces precede dementia diagnosis by 18 years in autosomal dominant Alzheimer's disease

Received: 2 June 2025 | Revised: 17 July 2025 | Accepted: 18 July 2025

DOI: 10.1002/alz.70588

Alzheimer's & Dementia®
THE JOURNAL OF THE ALZHEIMER'S ASSOCIATION

RESEARCH ARTICLE

Alterations in MRI-visible perivascular spaces precede dementia diagnosis by 18 years in autosomal dominant Alzheimer's disease

Riccardo Leone[1,2,3] | **Xenia Kobeleva**[1,3] | **Bryan Rowe**[4] | **Jeiran Choupan**[5,6] | **John M. Ringman**[4] | **Giuseppe Barisano**[7]

[1]Computational Neurology Group, Ruhr University Bochum, Bochum, Germany

[2]Faculty of Medicine, University of Bonn, Bonn, Germany

[3]German Center for Neurodegenerative Diseases (DZNE), Bonn, Germany

[4]Department of Neurology, Keck School of Medicine, University of Southern California, Los Angeles, California, USA

[5]Laboratory of Neuro Imaging (LONI), Mark and Mary Stevens Neuroimaging and Informatics Institute, Keck School of Medicine, University of Southern California, Los Angeles, California, USA

[6]NeuroScope Inc., Scarsdale, New York, USA

[7]Department of Neurosurgery, Stanford University, Stanford, California, USA

Correspondence
Giuseppe Barisano, Department of Neurosurgery, Stanford University, 1201 Welch Road, Stanford, CA 94305, USA.
Email: barisano@stanford.edu

Funding information
Alzheimer's Drug Discovery Foundation, Grant/Award Number: RC-202405-2026586; Helene and Lou Galen Professorship; National Institute on Aging, Grant/Award Numbers: K01AG22228, R01AG070825, R01AG062007, U01AG051218, P30AG066530, U19AG032438; National Institute of Mental Health, Grant/Award Number: RF1MH123223; National Institute of Neurological Disorders and Stroke, Grant/Award Number: R01NS128486; Alzheimer's Association, Grant/Award Number: SG-20-690363-DIAN; German Center for Neurodegenerative Diseases (DZNE); Raul Carrea Institute for Neurological Research (FLENI); Japan Agency for Medical Research and Development (AMED); Korea Health Industry Development Institute (KHIDI); Korea Dementia Research Center (KDRC); Ministry of Health & Welfare and Ministry of Science ICT, Republic of Korea,

Abstract

INTRODUCTION: Perivascular space (PVS) alterations are traditionally linked to cardiovascular risk factors and aging, but may also play a direct role in Alzheimer's disease (AD). To reduce confounding from age-related comorbidities, we examined PVSs in autosomal dominant AD (ADAD).

METHODS: In this cross-sectional study of 96 non-demented individuals (62 mutation carriers), we quantified PVS count fraction and mean diameter in white matter and basal ganglia using automated magnetic resonance imaging analysis. Linear mixed models assessed group differences along the disease course, adjusting for cardiovascular risk factors.

RESULTS: Compared to non-carriers, mutation carriers showed lower PVS count fraction in white matter and basal ganglia, and larger PVS diameter in basal ganglia and the temporal lobe. Changes were evident up to 18 years before expected dementia onset and followed trajectories similar to amyloid beta 42 and tau biomarkers.

DISCUSSION: ADAD is associated with early PVS alterations, suggesting perivascular changes may be integral to primary AD pathology.

KEYWORDS
Alzheimer's disease, autosomal dominant Alzheimer's disease, cerebral small vessel disease, dominantly inherited Alzheimer's disease, magnetic resonance imaging, perivascular spaces

Grant/Award Number: RS-2024-00344521; Spanish Institute of Health Carlos III (ISCIII)

Highlights

- Autosomal dominant Alzheimer's disease (ADAD) mutation carriers have reduced magnetic resonance imaging–visible perivascular space (PVS) count fraction in the white matter and basal ganglia.
- ADAD mutation carriers show enlarged PVS in the basal ganglia and temporal white matter.
- PVS alterations start 18 years before the estimated time of dementia diagnosis.
- The spatial localization of PVS changes overlaps with regions of amyloid beta (Aβ) accumulation.
- The temporal evolution of PVS alterations aligns with Aβ and tau changes in the cerebrospinal fluid.

1 | BACKGROUND

Cerebral small vessel disease (CSVD) is frequently observed in association with Alzheimer's disease (AD) pathology in *post mortem* analyses of individuals with late-onset AD[1] (LOAD), and may represent a significant contributor to neurodegeneration and cognitive impairment.[2] Similarly, in vivo neuroimaging markers of CSVD, such as white matter lesions (WMLs), lacunes, and perivascular space (PVS) alterations, often co-occur with abnormalities of AD biomarkers in elderly individuals.[3–5] However, CSVD markers are strongly associated with aging and cardiovascular risk factors. Therefore, whether the involvement of small brain vessels is an intrinsic component of AD pathogenesis or an independent pathological process is still unclear.

Autosomal dominant AD (ADAD)—a genetic form of AD determined by fully penetrant mutations in the genes coding for amyloid precursor protein (*APP*), presenilin 1 (*PSEN1*), or presenilin 2 (*PSEN2*)—provides a unique model for studying AD pathogenesis. ADAD mutations appear to cause disease through aberrant metabolism of amyloid beta (Aβ), leading to excessive production of long forms of Aβ.[6] Individuals with ADAD typically develop symptoms from a younger age (30–50 years),[7] when the confounding effects of aging and cardiovascular risk factors on brain pathology are limited. Additionally, the highly heritable age of symptom development in ADAD[7] allows one to approximate the estimated disease trajectory, which can be used as a reference to evaluate the timing of AD biomarker changes.[8–12] Identifying evidence of CSVD biomarker changes in ADAD would strongly suggest that they reflect primary AD-related pathological mechanisms rather than mechanisms secondary to aging or vascular comorbidities.

To date, a few studies have investigated WML in individuals with ADAD, reporting higher WML volume in mutation carriers compared to non-carriers. [9,13,14] Other vascular-related neuroimaging markers, such as PVS, remain understudied in ADAD. PVS are fluid-filled tubular spaces surrounding cerebral blood vessels, especially within the white matter (WM) and basal ganglia (BG).[15] PVS visibility on magnetic resonance imaging (MRI) depends on the presence of fluid within PVS,[16] which is driven by arterial pulsatility and vasomotion.[17–21] Current methods allow us to obtain whole-brain quantitative measures regarding the count and diameter of MRI-visible PVS in vivo, improving sensitivity in detecting subtle and early PVS alterations.[5] While the pathophysiology underlying PVS alterations remains unclear, it was proposed that blood–brain barrier breakdown, arteriolosclerosis, cerebral amyloid angiopathy (CAA), and/or glymphatic impairment may lead to alterations in fluid flow through PVS and subsequent modifications of PVS structure.[22] Previous *post mortem* studies in ADAD have described a higher prevalence of CAA[23] and other indices of cerebrovascular disease.[24] However, only one *post mortem* study investigated PVS in ADAD, reporting enlarged PVS diameter and suggesting that AD-specific mechanisms might involve the perivascular compartment.[25] In vivo evidence for PVS structural alterations in ADAD is lacking, and the regional and temporal course of these pathophysiological alterations remains unexplored.

In this study, we used a robust, fully automated, and clinically feasible MRI-based approach for PVS quantification,[5] to investigate, in vivo, PVS characteristics in ADAD mutation carriers versus non-carriers. We focused on two previously established markers of PVS pathology,[5] namely, PVS count fraction (i.e., the number of PVSs in a brain region divided by its volume), and PVS mean diameter. Lower PVS count and higher PVS diameter have recently been associated with increased risk of incident dementia and accelerated neurodegeneration in elderly individuals.[5] We thus hypothesized that mutation carriers would have a reduced PVS count fraction and increased PVS mean diameter, and that between-group changes in these biomarkers would be noticeable before dementia diagnosis. Furthermore, we also compared the observed trajectories of PVS changes to those of other well-established AD biomarkers.

Identifying novel in vivo pathologic features in ADAD, such as PVS alterations, has the potential to provide new insights into the pathophysiology of AD, to improve early diagnosis and monitoring of disease progression, and to offer new opportunities for the development of preventative or treatment strategies.

2 | METHODS

2.1 | Participants

We performed a retrospective cross-sectional analysis of individuals enrolled in prior and ongoing studies of ADAD being conducted by principal investigator J. M. Ringman. The data analyzed in this study were acquired between June 2005 and July 2022. Each participant was a member of a pedigree with a known mutation for ADAD in the *APP*, *PSEN1*, or *PSEN2* genes. Given the small number of participants at risk for inheriting *PSEN2* mutations, we treated *PSEN1* and *2* mutations together as a single *PSEN* group.

Though prior studies use parental- or mutation-based estimates of the age of symptom onset,[9,26,27] we have found variability among family members with regard to the report of symptom onset. More reliable is the age of dementia diagnosis, namely the age at which affected family members meet criteria for dementia by history. A mean age of dementia diagnosis was calculated for each mutation based on family member reports and the published literature (Table S1 in supporting information).[7] We calculated the estimated years from dementia diagnosis (EDD) by subtracting from the participant's age the expected age of dementia diagnosis associated with the mutation they were at risk for inheriting. Based on data freeze 17 of the Dominantly Inherited Alzheimer Network (DIAN) dataset, the average difference between the DIAN-determined age of first symptom onset and our determined age of dementia diagnosis is ≈ 2.6 years.

We gathered data from 121 subjects with available MRI and clinical information obtained during the same visit. We limited our analyses to subjects without dementia, as defined by having a Clinical Dementia Rating scale score ≤ 1 and assessed before their expected age of dementia diagnosis (EDD ≤ 0). This choice was performed to focus on the earliest stages of the disease to avoid potential confounding effects due to severe brain atrophy, which could bias estimations of PVS. Ninety-six subjects met the inclusion criteria and had full availability of clinical covariates of interest (see next section). All participants or their caregivers provided informed consent.

2.2 | Covariates of interest

Covariates of interest included EDD; reported sex; history of hypertension, hypercholesterolemia, and diabetes; apolipoprotein E (*APOE*) genotype; and mutation status. *APOE* status was coded categorically (presence or absence of an ε4 allele). Cardiovascular risk was quantified by summing scores for hypertension, hyperlipidemia, and diabetes presence (1 point for each risk factor, total range: 0–3).

2.3 | MRI data acquisition and processing

Brain MRI was performed on 1.5 Tesla (N = 13), or 3 Tesla (N = 83) Siemens scanners using T1-weighted magnetization-prepared rapid gradient echo (MPRAGE) sequence (parameters in Table S2 in supporting information). All imaging analyses were completed with fully automated algorithms without knowledge of mutation status, or demographic or clinical data.

Images were preprocessed and resampled to 1 mm isotropic resolution with FreeSurfer v7.4,[28] as previously described.[5] PVS were automatically segmented on preprocessed T1-weighted images in the whole-brain normal appearing WM (obtained by subtracting the WML voxels from the WM mask), and in the BG. The PVS segmentation method enhances vessel-like structures by applying a Frangi filter,[29] which assigns a "vesselness" value based on the eigenvalues of the Hessian matrix. The value of the 85th percentile of the total number of voxels with non-zero "vesselness" is used as a threshold, and only voxels with a "vesselness" value above this threshold are retained and binarized to generate a PVS mask. MATLAB's "regionprops3" was used to compute count and mean diameter across all PVS clusters with an in-plane size of at least 2 voxels in each region. PVS count was standardized by the volume of each region, yielding a PVS count fraction, as per previous recommendations.[16] Both PVS metrics have excellent intraclass correlation coefficients (≥ 0.9 for WM-PVS and ≥ 0.8 for BG-PVS) regarding inter-scanner reproducibility, interfield–strength reproducibility, and test–retest repeatability.[5] We also performed exploratory analyses considering PVS characteristics in the normal-appearing WM of each brain lobe (frontal, parietal, temporal, insular, and occipital), as parcellated with FreeSurfer v7.4.[28] Values were averaged between the left and right hemispheres before further

RESEARCH IN CONTEXT

1. **Systematic review**: We conducted a systematic review of PubMed through December 1, 2024, and found only one prior *post mortem* study reporting enlarged perivascular spaces (PVSs) in autosomal dominant Alzheimer's disease (ADAD).
2. **Interpretation**: Whether PVS alterations reflect primary Alzheimer's disease (AD) pathology or age-related vascular comorbidities remains unclear. Here, we provide the first in vivo evidence that ADAD mutation carriers exhibit significantly lower PVS count fraction in the white matter and basal ganglia, alongside increased PVS diameter in the basal ganglia and temporal lobe, compared to non-carriers. These differences emerged up to 18 years before expected dementia onset and followed a temporal and spatial trajectory similar to established AD biomarkers such as amyloid beta and tau. PVS alterations were independent of cardiovascular risk factors.
3. **Future directions**: Our findings support a direct involvement of the vascular/perivascular compartment in ADAD pathophysiology and suggest that magnetic resonance imaging–visible PVSs may serve as an early, accessible biomarker of disease progression.

analysis. WML were segmented on preprocessed T1-weighted images with a fully automated algorithm,[30] robust in terms of interscanner and test–retest reproducibility, and whose results strongly correlated with those obtained from fluid-attenuated inversion recovery (FLAIR) sequences.[5]

All segmentation masks were visually checked for accuracy in a blinded fashion by an expert physician scientist (G.B., 10 years of experience in neuroimaging). Individual PVS segmentations for all subjects are available at https://gbarisano.shinyapps.io/pvs-dementia/ (select project: "Autosomal Dominant Alzheimer Disease – EEAJ").

2.4 | Statistical analysis

Descriptive statistics are presented for categorical data as numbers (percentages) and for continuous data as mean ± standard deviation for normally distributed variables, or as median (interquartile range) for not-normally distributed variables. Categorical variables were compared between the mutation status group based on the chi-squared test, while continuous variables were compared with the two-sample independent *t* test or Mann–Whitney *U* test for normally and not-normally distributed variables, respectively.

A linear mixed model, with family membership as a random factor,[8] was used to estimate the association of mutation status versus PVS count fraction or PVS mean diameter as dependent variables in each considered region. Analyses were adjusted for EDD and its interaction with mutation status, cardiovascular risk, *APOE* status, and sex, as fixed factors. A similar model was also run with WML volume (log-transformed) as the dependent variable. Total intracranial volume was not significantly associated with PVS metrics nor with WML and was not included as a covariate (Figure S1 in supporting information). Following previous studies,[8,31] we assessed PVS biomarker differences at various age points using an approximate Student *t* test on results derived from linear mixed models. This allowed us to assess the trajectories of PVS changes over time and to identify the time point of the first significant differences between groups.

Most subjects lacked cerebrospinal fluid (CSF) and positron emission tomography (PET) imaging data. Given the highly heritable age of symptom development in ADAD, which allows one to approximate the estimated disease trajectory,[7] we compared PVS metrics to other well-established biomarkers of ADAD using data from Bateman et al.[8] These data represent the standardized differences in each biomarker between mutation carriers and non-carriers as a function of estimated years from symptom onset (EYO). To reconcile the difference between the definition of EYO used in Bateman et al.[8] and our definition of EDD, we added 2.6 years—the average time difference between DIAN-determined EYO and our-determined EDD—to EDD and used this surrogate EYO when comparing our PVS metrics with the other ADAD biomarkers. Following Bateman et al.,[8] we calculated estimates for PVS metrics using the previously described linear mixed models.

A p value of < 0.05 was considered statistically significant for analyses of WM or BG. Exploratory analyses were also performed for each brain lobe.

TABLE 1 Subject characteristics divided by the presence or absence of mutations leading to autosomal dominant Alzheimer's disease.

	Non-carriers ($n = 34$)	Carriers ($n = 62$)	p value
Age	35.0 (28.2 - 39.0)	32.5 (26.2–41.8)	0.930
EDD (years)	−15.32 ± 9.83	−13.32 ± 8.34	0.319
WML volume (log)	1.8 (0.0 - 2.3)	2.3 (1.8–2.6)	**0.006**
Sex			0.91
Male	12 (35.29%)	24 (38.71%)	
Female	22 (64.71%)	38 (61.29%)	
APOE ε4+ (%)			1.00
0	26 (76.47%)	48 (77.42%)	
1	8 (23.53%)	14 (22.58%)	
CV risk (%)			0.12
0	26 (76.47%)	54 (87.1%)	
1	8 (23.53%)	6 (9.68%)	
2	0 (0.0%)	2 (3.23%)	
Gene (%)			1.00
APP	7 (20.59%)	12 (19.35%)	
PSEN1/2	27 (79.41%)	50 (80.65%)	

Note: Categorical data are reported as a number (percentages), and the corresponding *p* value refers to differences between the mutation status groups based on the chi-squared test. Continuous data are reported as mean ± standard deviation for normally distributed variables or as median (interquartile range) for variables that are not normally distributed. Corresponding *p* value refers to the two-sample independent *t* test or Mann–Whitney *U* test for normally and not normally distributed variables, respectively. Statistically significant comparisons are highlighted in bold.
Abbreviations: ADAD, Autosomal dominant Alzheimer's disease; *APOE*, apolipoprotein E; *APP*, amyloid precursor protein; CV, cardiovascular; EDD, estimated years from dementia diagnosis; *PSEN*, presenilin; WML, white matter lesion.

3 | RESULTS

We analyzed data from 96 subjects (median age: 33 [interquartile range: 27–40], 62.5% females). Among them, 62 (64.6%) were carriers of ADAD mutations: 50 (80.6%) had *PSEN* mutations and 12 (19.4%) had *APP* mutations (Table 1). In unadjusted comparisons, mutation carriers showed a significantly greater volume of WML ($p = 0.006$). After adjusting for other covariates in a linear mixed model, no significant associations between WML volume and mutation status were found ($p = 0.18$, Table S3 in supporting information). There were no other significant differences between groups in clinical or demographic variables. In mutation carriers, the BG–PVS count fraction was significantly correlated with WM–PVS count fraction, as well as with regional values in the frontal and insular lobes. Similarly, the mean BG-PVS diameter showed significant correlations with mean WM–PVS diameter in the white matter and in all cortical lobes except the occipital lobe (Table S4 in supporting information).

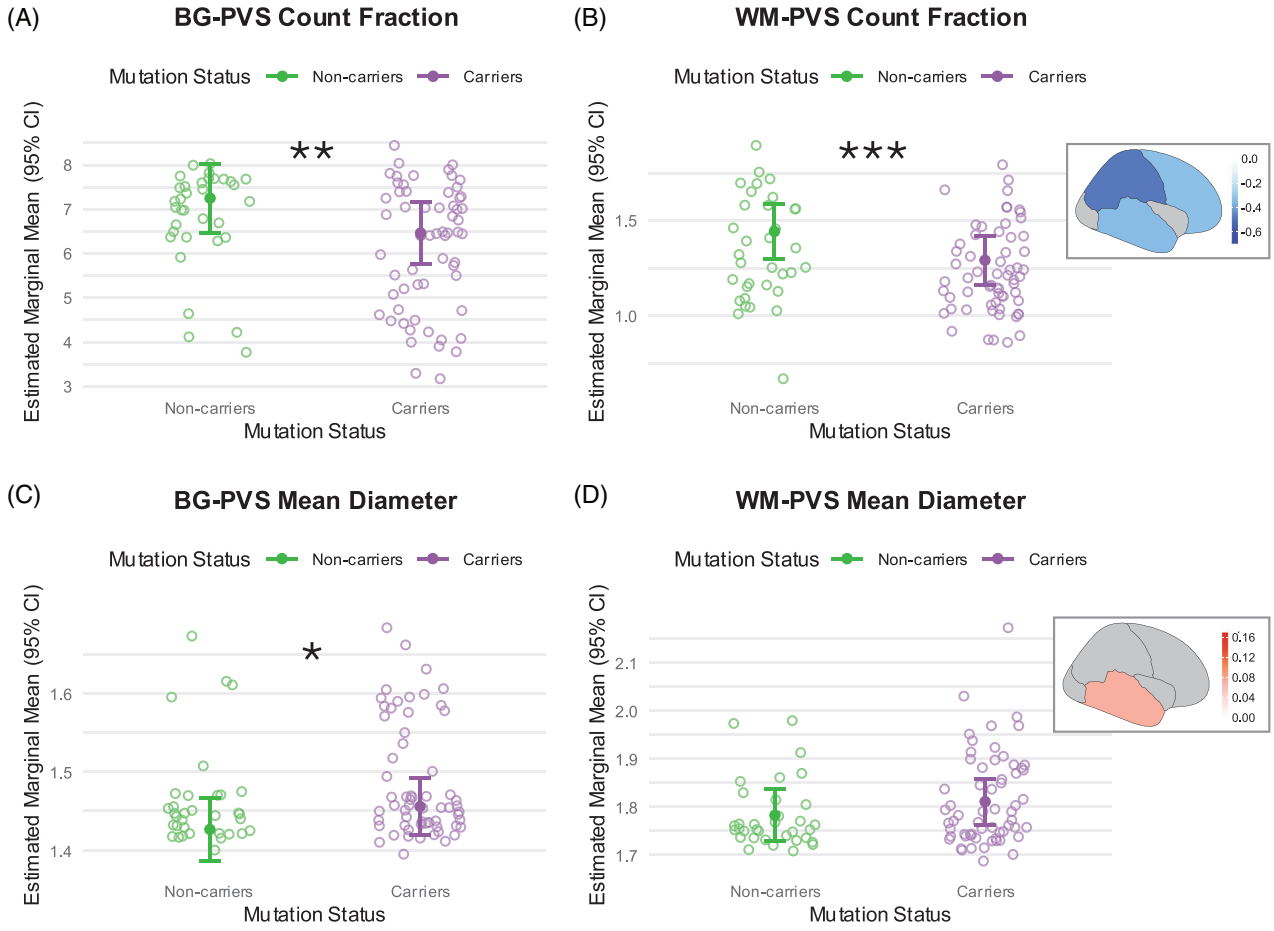

FIGURE 1 Differences in perivascular space count fraction and mean diameter in the white matter and basal ganglia. Estimated marginal means (solid dots) and 95% confidence intervals (error bars) for PVS count fraction (A, B) and PVS mean diameter (C, D) in non-carriers (green) and mutation carriers (violet) in the BG (A, C) and WM (B, D). Mean estimates were obtained using linear mixed models including mutation status, estimated years from dementia diagnosis, and their interaction; sex, cardiovascular risk score; and presence of an *APOE* ε4 allele as fixed effects, while family membership was included as a random effect. Empty colored dots correspond to individual empirical observations. The asterisk(s) refer to the *p* value for the variable "mutation status" obtained from the adjusted linear mixed model. Insets in (B) and (D) show color-coded brain maps illustrating model coefficients for "mutation status" in various brain regions against PVS count fraction or PVS mean diameter, respectively. Cooler colors (e.g., darker blue) represent regions with stronger negative associations, while warmer colors (e.g., red) indicate regions with stronger positive associations between mutation status and PVS biomarkers. Only regions with uncorrected *p* value < 0.05 are shown, while others are grayed out.*: $0.01 \leq p < 0.05$; **: $0.001 \leq p < 0.01$; ***: $0.0001 \leq p < 0.001$. *APOE*, apolipoprotein E; BG, basal ganglia; CI, confidence interval; PVS, perivascular space; WM, white matter.

We first estimated overall differences in PVS metrics in mutation carriers compared to non-carriers (Figure 1, Table S3). Mutation carriers showed significantly lower PVS count fraction in the WM ($\beta = -0.33$, 95% confidence interval [CI]: −0.5 to −0.17, $p = 0.00013$)—particularly in the frontal, parietal, and temporal lobes (exploratory regional analyses summarized in Table S5 in supporting information)—and in the BG ($\beta = -1.5$, 95% CI: −2.4 to −0.65, $p = 0.0011$). PVS mean diameter was significantly higher in mutation carriers versus non-carriers in the BG ($\beta = 0.055$, 95% CI: 0.0093 to 0.10, $p = 0.021$), but not across the whole WM ($\beta = 0.034$, 95% CI: −0.028 to 0.097, $p = 0.28$). In exploratory analyses at a lobar level, PVS mean diameter was greater in the temporal lobe of carriers versus non-carriers (Table S5). We observed significant positive associations between BG and WM–PVS count fraction and EDD. This association is analogous to the established positive association between PVS count fraction and increasing chronological age observed in adults.[32] However, this positive association with EDD was significantly modified by mutation status, as indicated by a negative interaction effect (Table S3). While non-carriers exhibited the expected increase in BG and WM–PVS count fraction with increasing EDD,[32] the negative interaction effect resulted in a significant decrease in PVS count fraction with increasing EDD among mutation carriers (Table 2). We confirmed the known positive association between WM–PVS count fraction and male sex,[5,32] and found a significant negative association between mean BG–PVS diameter and *APOE* status (Table S3).

Next, following Bateman et al.[8] and Araque Caballero et al.,[31] we estimated differences in PVS count fraction between carriers and non-carriers at various time cut-offs (Figure 2, Table 2). This allowed us to

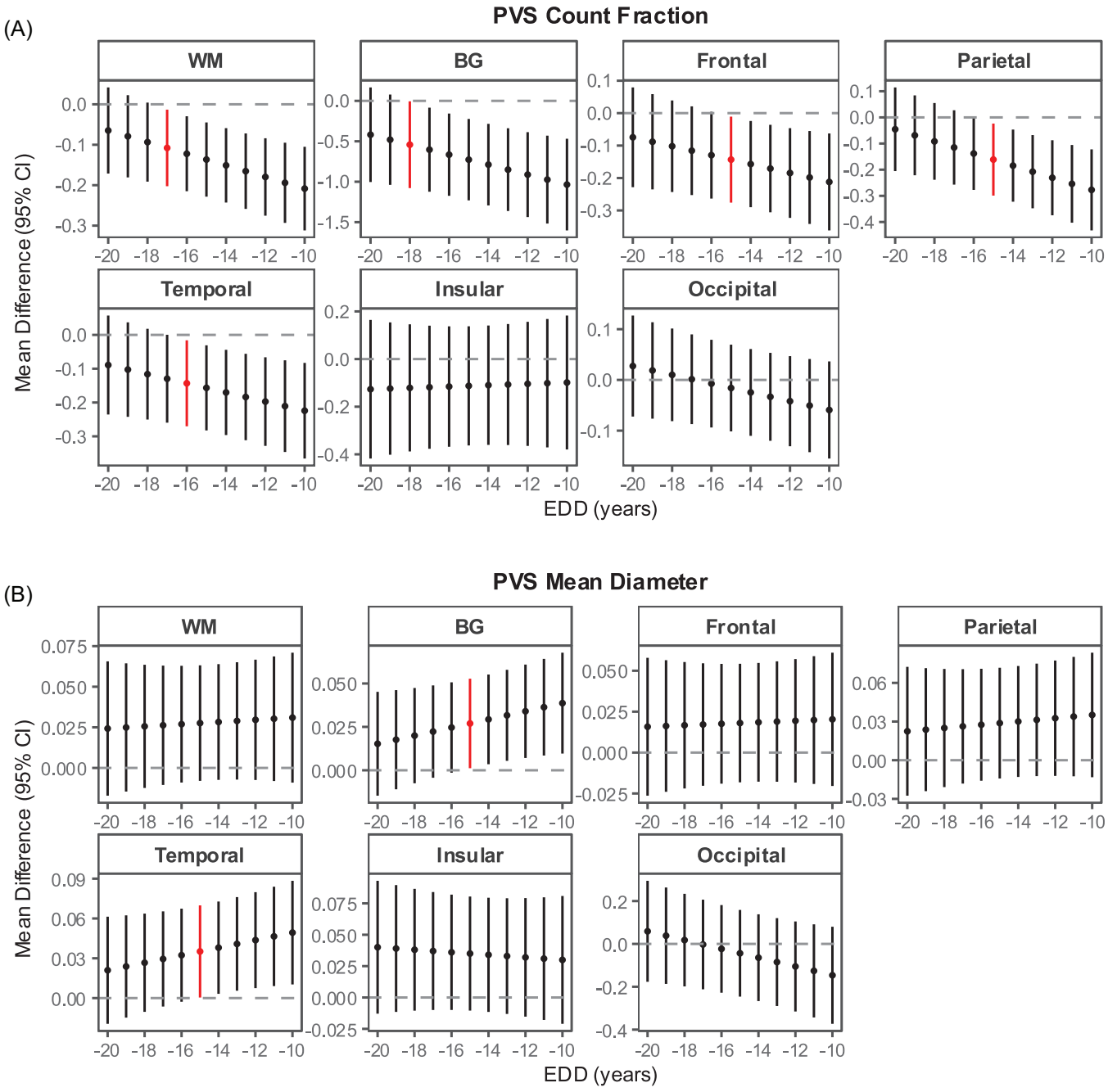

FIGURE 2 Time of first detectable changes in perivascular spaces count fraction and mean diameter. Mean and 95% confidence intervals of the estimated differences in PVS count fraction (A) and mean diameter (B) between mutation carriers and non carriers. Differences were calculated with linear mixed models at each estimated year from EDD (range: -20 to -10). Linear mixed models included mutation status, EDD, and their interaction; sex; cardiovascular risk score; and presence of *APOE ε4* allele(s) as fixed effects, while family membership was included as a random effect. Estimated mean differences were averaged over levels of cardiovascular risk, sex, and *APOE*. The red bar indicates the earliest time point of abnormal PVS metrics for a particular brain region. *APOE*, apolipoprotein E; BG, basal ganglia; CI, confidence interval; EDD, expected dementia diagnosis; PVS, perivascular space; WM, white matter.

identify the earliest timepoint at which significant differences in PVS biomarkers were first observed in carriers compared to non-carriers. We observed the first significant reductions in PVS count fraction at −18 years before EDD in the BG and at −17 years in the WM (Table S6 in supporting information). The first significant increase in BG–PVS mean diameter was seen −15 years before EDD. Regional estimates of between-group differences in PVS biomarkers highlighted early reductions in PVS count fraction in the temporal, frontal, and parietal lobes, as well as early PVS enlargement in the temporal lobe (Figure 2, Table S6 and S7 in supporting information).

Then, we compared how PVS alterations evolve over time in relation to changes of other well-established AD biomarkers (Figure 3).

TABLE 2 Perivascular spaces metrics estimates in mutation carriers versus non-carriers.

		Estimated years from dementia diagnosis					
Variable	**Region**	**−25**	**−20**	**−15**	**−10**	**−5**	**0**
PVS count fraction							
Non-carriers	WM	1.34	1.39	1.43	1.48	1.53	1.58
Carriers	WM	1.34	1.32	1.30	1.27	1.25	1.23
Difference	WM	0.01±0.14	−0.06±0.11	−0.14±0.09	−0.21±0.10	−0.28±0.13	−0.35±0.18
Non-carriers	BG	7.12	7.18	7.24	7.30	7.36	7.42
Carriers	BG	7.01	6.76	6.51	6.26	6.01	5.77
Difference	BG	−0.11±0.77	−0.42±0.59	−0.73±0.5	−1.04±0.57	−1.34±0.74	−1.65±0.96
PVS mean diameter							
Non-carriers	WM	1.76	1.77	1.78	1.79	1.80	1.81
Carriers	WM	1.78	1.80	1.81	1.82	1.83	1.84
Difference	WM	0.02±0.05	0.02±0.04	0.03±0.04	0.03±0.04	0.03±0.05	0.04±0.07
Non-carriers	BG	1.435	1.431	1.427	1.423	1.420	1.416
Carriers	BG	1.438	1.446	1.454	1.462	1.470	1.478
Difference	BG	0.004±0.039	0.015±0.03	0.027±0.026	0.039±0.029	0.05±0.038	0.062±0.049

Note: Estimates of mean PVS count fraction and mean diameter in the WM and BG at various age cut-offs were calculated using the estimated years from dementia diagnosis. Difference refers to the estimated difference between mutation carriers and non-carriers ± 95% confidence intervals. Reported estimates were obtained using a linear mixed model with mutation status (non-carrier or carrier), expected years from dementia diagnosis, and their interaction, cardiovascular risk score, presence of an *APOE* ε4 allele, and sex as fixed effects. Family membership was considered a random effect. Results were averaged over levels of cardiovascular risk, sex, and *APOE*. For regional estimates in the WM, see Table S5 in supporting information. Note that there might be small discrepancies in differences due to rounding.

Abbreviations: *APOE*, apolipoprotein E; BG, basal ganglia; PVS, perivascular spaces; WM, white matter.

Using data from a previous study by Bateman et al.[8] for this comparison, we found that the initial changes and following time course of PVS count fraction reduction and BG–PVS enlargement closely aligned with reported changes in Aβ and tau in the CSF (Figure 3).

Finally, we compared PVS characteristics between carriers of *APP* and *PSEN* mutations. We found no statistically significant differences in PVS metrics, except for a lower PVS count fraction in the temporal lobe of *PSEN* carriers compared to *APP* carriers ($p = 0.003$, Figure S2 in supporting information).

4 | DISCUSSION

We found significant PVS alterations in carriers of pathogenetic mutations for ADAD compared to non-carrier family members. The first differences occurred as early as 18 years before the expected age of dementia diagnosis. The timeframe of initial PVS changes and their trajectory along the estimated disease course aligned with those of Aβ and tau pathology in the CSF previously reported in ADAD[8] and LOAD.[33] The spatial localization of PVS changes also overlapped with regions of known early pathology in ADAD.[8,10,34] Between-group differences in PVS metrics became more prominent as the disease progressed, suggesting that PVS alterations may contribute to ensuing neurodegeneration and the development of symptoms. Given the young age of the analyzed individuals and the independence of these results from cardiovascular risk factors, our findings suggest that alterations in MRI-visible PVS might indicate pathological processes occurring in the small cerebral vessels and/or their perivascular compartments that are specifically related to AD pathophysiology rather than other comorbidities.

We found that mutation carriers had significantly lower PVS count fraction in the BG and WM compared to non-carriers. It is important to note that our PVS count fraction differs from the conventional count of PVS in visual rating scales performed by human raters. Traditional visual rating methods typically assess the number of visibly enlarged PVS in one hemisphere within a single representative MRI slice. This approach provides only a partial view of PVS burden, may depend on the rater performing the evaluation, and lacks sensitivity to smaller or non-enlarged PVS. Moreover, visual rating scales typically do not account for total or regional brain volume, despite evidence that PVS counts are associated with brain volume.[16] In contrast, our fully automated segmentation method quantifies all MRI-visible PVS across the entire brain, irrespective of their enlargement status. This allows us to perform a complete quantitative analysis, also incorporating blood vessels with small/non-enlarged perivascular space.[5] Moreover, by using PVS count fraction (number of PVS divided by regional volume) in all our analyses, we corrected for brain volume as a potential confounder. Our approach thus enables a more sensitive, comprehensive, accurate, and reproducible characterization of overall PVS characteristics compared to visual rating scales.[5]

PVS are considered a marker of CSVD,[15] and their visibility on MRI depends on the presence of fluid within the perivascular

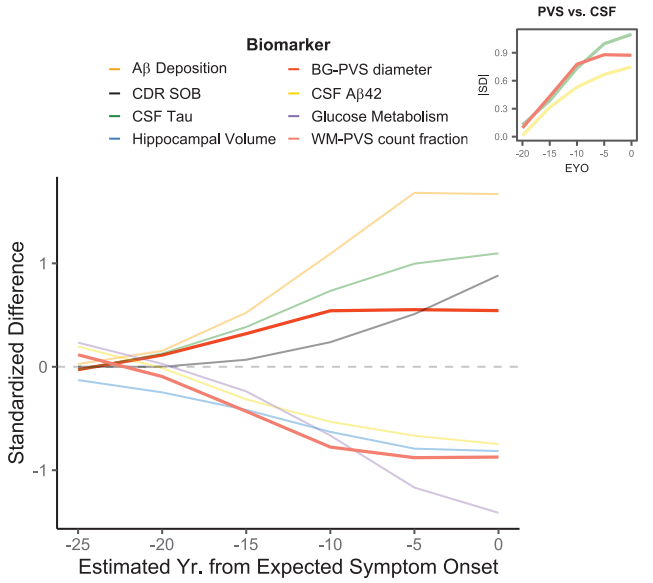

FIGURE 3 Changes in clinical, imaging, and biochemical biomarkers with respect to changes in perivascular space metrics as a function of estimated years from expected symptom onset. The main panel displays the SD between mutation carriers and non carriers over the expected course of the disease for various clinical, imaging, and biochemicat biomarkers, as reported in Bateman et al. These differences are compared to the SD in PVS count fraction in the WM (WM-PVS count fraction, in tight red) and PVS mean diameter in the BG (BG-PVS mean diameter, in red). The expected course of the disease is assessed using the estimated years from EYO. To reconcile the discrepancy between the definition of EYO onset used in Bateman et al. and our definition of EDD, we added 2.6 years to EDD before estimating SD for PVS metrics. This number represented the average time difference between DIAN-determined EYO and our-determined EDD (see main text). The inset highlights the comparison between WM-PVS count fraction and CSF biomarkers (Aβ and tau). To facilitate visual comparisons of the relative magnitude and temporal course of changes, absolute values of SDs are shown. Aβ, amyloid beta; BG, basal ganglia; CDR-SOB, Clinical Dementia Rating Sum of Boxes; CSF, cerebrospinal fluid; DIAN, Dominantly Inherited Alzheimer Network; EDD, expected dementia diagnosis; EYO, expected symptom onset; PVS, perivascular space; SD, standardized differences; WM, white matter.

compartment,[16] and on its flow, which is driven by arterial pulsatility and vasomotion.[17,18,20] Although the exact pathophysiology underlying reduced PVS visibility on MRI is still not fully elucidated, impaired arterial pulsatility has been associated with reduced PVS fluid flow,[19,21] and a lower PVS count has been associated with cerebral hypoperfusion.[5] Given these associations, the reduction in PVS count fraction observed in mutation carriers may reflect early AD-related small vessel pathology. This interpretation is supported by previous findings of CSVD in *post mortem* ADAD cases,[25] lower cerebral blood flow in ADAD,[35] and reduced microvascular density in Down syndrome,[36] a condition characterized by overexpression of the APP gene linked with increased brain amyloid levels and early-onset AD. This suggests that the genetic underpinnings of ADAD might lead to early vascular changes, potentially affecting perivascular fluid flow, and consequently, reducing the MRI visibility of PVS. Consistently, recent studies of PVS in LOAD have also found lower PVS amount across multiple brain regions in patients with mild cognitive impairment or before the development of dementia compared to cognitively unimpaired and stable subjects.[5,37]

PVS are increasingly recognized as a crucial component of the brain's glymphatic system, which is responsible for the clearance of metabolites, interstitial fluid, and waste from the brain.[16,22,38] Accumulation of misfolded proteins within PVS might impede fluid flow,[39] contributing to the observed reduction in MRI-visible PVS. The earliest significant reductions in PVS count fraction occurred in the BG and WM ≈ 18 years before the estimated onset of dementia and increased over time. Specifically, while non-carriers exhibited the expected increase in BG and WM–PVS count fraction with increasing age (as represented by EDD),[32] mutation carriers showed reductions in PVS count over time. The trajectory of between-group PVS changes aligned temporally with differences in $A\beta_{1\text{-}42}$ and tau in the CSF.[8,11] Reductions in PVS count fraction were prominent in the basal ganglia and parietal, temporal, and frontal lobes. These regions are well known to exhibit early and elevated deposition of Aβ in ADAD.[8,10,34] Collectively, these results suggest a potential interplay between PVS and Aβ pathology. Impaired perivascular drainage, potentially exacerbated by Aβ accumulation within the perivascular compartment and/or vessel walls (i.e., CAA), could compromise fluid flow along PVS,[40] possibly creating a pathogenic feedback loop. Prior neuropathological studies have shown a higher prevalence of CAA in *post mortem* cases of ADAD,[23,24] but the precise timing of its development remains to be elucidated.

We observed significantly enlarged PVS in mutation carriers compared to non-carriers, especially within the BG and temporal WM. This finding provides in vivo corroboration for previous *post mortem* reports indicating PVS enlargement in individuals with ADAD.[25] The co-occurrence and temporal sequence of reduced PVS count and enlarged PVS diameter warrant careful consideration of the underlying mechanisms. One possibility is that these two phenomena may be pathologically linked. The reduction in the number of MRI-detectable PVS might relate to the obstruction of perivascular pathways. This could lead to a compensatory redistribution and accumulation of perivascular fluid in the remaining patent spaces, which might drive their progressive enlargement over time. This interpretation, although speculative, is supported by our findings that PVS enlargement emerged later than the initial reduction in count fraction, ≈ 15 years before the expected onset of dementia. Alternatively, mechanisms not directly associated with Aβ might drive PVS enlargement. For example, the timeframe of PVS enlargement parallels that of alterations of a secreted form of triggering receptor expressed on myeloid cells 2—a surrogate marker for microglial activation—in the CSF,[41] suggesting a potential role for inflammatory infiltrates.[42–44] Additionally, PVS enlargement in ADAD has been associated with reductions in astrocytic aquaporin-4, in the absence of CAA.[25] In this regard, we found a negative association between mean BG–PVS diameter and the presence of an *APOE* ε4 allele. This may lend some further support to the hypothesis that PVS enlargement, at least in this region, may occur due to processes distinct from CAA, given that *APOE* ε4 is a known risk factor for

CAA.[45] Previous findings on the association between PVS enlargement and *APOE* ε4 have been mixed, ranging from null results[46,47] to significant PVS enlargement only in the presence of two copies of the ε4 allele.[5] Future research is needed to further elucidate the influence of *APOE* genotypes on PVS enlargement. Last, in our ADAD cohort, we observed similar associations and significant correlations between PVS metrics in the BG and in several WM regions. While previous literature often emphasizes a clear dichotomy between BG and WM PVS alterations in older adults—typically linking them to distinct vascular pathologies—our findings support the notion that in the context of ADAD, PVS alterations may reflect a shared and AD-specific pathological mechanism.

Our study has some limitations, including its cross-sectional nature. Nonetheless, ADAD is characterized by a stereotypical pattern of pathological progression, with a predictable age of symptoms and dementia onset.[8] Therefore, the use of EDD allowed us to assess the evolution of PVS changes along the estimated trajectory of the disease. Another limitation is the lack of other AD biomarkers, such as amyloid and tau CSF or PET data. Thus, we could only indirectly compare how the trajectories of PVS changes relate to other AD biomarkers based on previously published data. Future longitudinal studies are needed to better evaluate the coupled temporal dynamics between PVS and other AD biomarker changes in the same individuals. Additionally, regional analyses were exploratory, aiming to identify specific locations with greater PVS changes. Consequently, these findings should be interpreted with caution as hypothesis generating. However, they provide a foundation for targeted, confirmatory investigations in independent cohorts of individuals with ADAD.

In conclusion, ADAD mutation carriers show early alterations in PVS characteristics in the WM and BG. These PVS alterations may be specific for AD-associated processes and not related to cardiovascular risk factors. Given the early involvement in the disease, the regional distribution of changes, and the hypothesized co-localization of several pathological mechanisms at/near PVS, our findings point to PVS as a relevant hub of pathology in ADAD. If confirmed in future longitudinal studies, this evidence could support research for preventative or treatment strategies targeting the vascular/perivascular compartment in ADAD. Furthermore, given the need for only a 3D T1-weighted MRI sequence, which is commonly acquired in clinical and research MRI protocols, our PVS metrics might be promising non-invasive and inexpensive candidate biomarkers to monitor disease course in ADAD.

ACKNOWLEDGMENTS

We acknowledge the altruism of the participants and their families and contributions of the DIAN research and support staff at each of the participating sites for their contributions to this study. This study was supported by grant RC-202405-2026586 from the Alzheimer's Drug Discovery Foundation to G.B., and by NIA K01AG22228, R01AG062007, U01AG051218, P30AG066530, and the Helene and Lou Galen Professorship to J.M.R. J.C. is supported by grants RF1MH123223, R01AG070825, and R01NS128486 from the NIH. Data collection and sharing for this project was supported by The Dominantly Inherited Alzheimer Network (DIAN, U19AG032438) funded by the National Institute on Aging (NIA), the Alzheimer's Association (SG-20-690363-DIAN), the German Center for Neurodegenerative Diseases (DZNE), Raul Carrea Institute for Neurological Research (FLENI), and partial support by the Research and Development Grants for Dementia from Japan Agency for Medical Research and Development (AMED), the Korea Health Technology R&D Project through the Korea Health Industry Development Institute (KHIDI), Korea Dementia Research Center (KDRC), funded by the Ministry of Health & Welfare and Ministry of Science and ICT, Republic of Korea RS-2024-00344521, and Spanish Institute of Health Carlos III (ISCIII). This manuscript has been reviewed by DIAN Study investigators for scientific content and consistency of data interpretation with previous DIAN Study publications. The founding sources had no role in study design; in the collection, analysis, and interpretation of data; in the writing of the report; nor in the decision to submit the article for publication.

CONFLICT OF INTEREST STATEMENT

The authors declare no conflicts of interest. J.C. receives salary from a startup company, NeuroScope Inc. G.B. is listed as an inventor on a patent application related to this work filed by Stanford University, with no financial interest/conflict. All other authors declare no competing interests. Author disclosures are available in the supporting information.

CONSENT STATEMENT

All participants or their caregivers provided informed consent.

ORCID

Riccardo Leone https://orcid.org/0000-0001-5569-6090
Giuseppe Barisano https://orcid.org/0000-0001-5598-1369

REFERENCES

1. Karanth S, Nelson PT, Katsumata Y, et al. Prevalence and clinical phenotype of quadruple misfolded proteins in older adults. *JAMA Neurol*. 2020;77(10):1299-1307. doi:10.1001/jamaneurol.2020.1741
2. Wardlaw JM, Smith C, Dichgans M. Small vessel disease: mechanisms and clinical implications. *Lancet Neurol*. 2019;18(7):684-696. doi:10.1016/S1474-4422(19)30079-1
3. Graff-Radford J, Arenaza-Urquijo EM, Knopman DS, et al. White matter hyperintensities: relationship to amyloid and tau burden. *Brain*. 2019;142(8):2483-2491. doi:10.1093/brain/awz162
4. Zhang J, Chen H, Wang J, et al. Linking white matter hyperintensities to regional cortical thinning, amyloid deposition, and synaptic density loss in Alzheimer's disease. *Alzheimers Dement*. 2024;20(6):3931-3942. doi:10.1002/alz.13845
5. Barisano G, Iv M, Choupan J, et al. Robust, fully-automated assessment of cerebral perivascular spaces and white matter lesions: a multicentre MRI longitudinal study of their evolution and association with risk of dementia and accelerated brain atrophy. *eBioMed*. 2025;111:105523. doi:10.1016/j.ebiom.2024.105523
6. Petit D, Fernández SG, Zoltowska KM, et al. Aβ profiles generated by Alzheimer's disease causing PSEN1 variants determine the pathogenicity of the mutation and predict age at disease onset. *Mol Psychiatry*. 2022;27(6):2821-2832. doi:10.1038/s41380-022-01518-6
7. Ryman DC, Acosta-Baena N, Aisen PS, et al. Symptom onset in autosomal dominant Alzheimer disease: a systematic

review and meta-analysis. *Neurology*. 2014;83(3):253-260. doi:10.1212/WNL.0000000000000596
8. Bateman RJ, Xiong C, Benzinger TLS, et al. Clinical and biomarker changes in dominantly inherited Alzheimer's disease. *N Engl J Med*. 2012;367(9):795-804. doi:10.1056/NEJMoa1202753
9. Lee S, Viqar F, Zimmerman ME, et al. White matter hyperintensities are a core feature of Alzheimer's disease: evidence from the dominantly inherited Alzheimer network. *Ann Neurol*. 2016;79(6):929-939. doi:10.1002/ana.24647
10. Gordon BA, Blazey TM, Su Y, et al. Spatial patterns of neuroimaging biomarker change in individuals from families with autosomal dominant Alzheimer's disease: a longitudinal study. *Lancet Neurol*. 2018;17(3):241-250. doi:10.1016/S1474-4422(18)30028-0
11. Fagan AM, Xiong C, Jasielec MS, et al. Longitudinal change in CSF biomarkers in autosomal-dominant Alzheimer's disease. *Sci Transl Med*. 2014;6(226):226ra30-226ra30. doi:10.1126/scitranslmed.3007901
12. Wisch JK, McKay NS, Boerwinkle AH, et al. Comparison of tau spread in people with Down syndrome versus autosomal-dominant Alzheimer's disease: a cross-sectional study. *Lancet Neurol*. 2024;23(5):500-510. doi:10.1016/S1474-4422(24)00084-X
13. Shirzadi Z, Schultz SA, Yau WYW, et al. Etiology of white matter hyperintensities in autosomal dominant and sporadic Alzheimer disease. *JAMA Neurol*. 2023;80(12):1353. doi:10.1001/jamaneurol.2023.3618
14. Joseph-Mathurin N, Feldman RL, Lu R, et al. Presenilin-1 mutation position influences amyloidosis, small vessel disease, and dementia with disease stage. *Alzheimers Dement*. 2024;20(4):2680-2697. doi:10.1002/alz.13729
15. Duering M, Biessels GJ, Brodtmann A, et al. Neuroimaging standards for research into small vessel disease—advances since 2013. *Lancet Neurol*. 2023;22(7):602-618. doi:10.1016/S1474-4422(23)00131-X
16. Barisano G, Lynch KM, Sibilia F, et al. Imaging perivascular space structure and function using brain MRI. *NeuroImage*. 2022;257:119329. doi:10.1016/j.neuroimage.2022.119329
17. Hadaczek P, Yamashita Y, Mirek H, et al. The "Perivascular Pump" driven by arterial pulsation is a powerful mechanism for the distribution of therapeutic molecules within the brain. *Mol Ther*. 2006;14(1):69-78. doi:10.1016/j.ymthe.2006.02.018
18. Iliff JJ, Wang M, Zeppenfeld DM, et al. Cerebral arterial pulsation drives paravascular CSF-interstitial fluid exchange in the murine brain. *J Neurosci*. 2013;33(46):18190-18199. doi:10.1523/JNEUROSCI.1592-13.2013
19. Kress BT, Iliff JJ, Xia M, et al. Impairment of paravascular clearance pathways in the aging brain. *Ann Neurol*. 2014;76(6):845-861. doi:10.1002/ana.24271
20. van Veluw SJ, Hou SS, Calvo-Rodriguez M, et al. Vasomotion as a driving force for paravascular clearance in the awake mouse brain. *Neuron*. 2020;105(3):549-561.e5. doi:10.1016/j.neuron.2019.10.033
21. Mestre H, Tithof J, Du T, et al. Flow of cerebrospinal fluid is driven by arterial pulsations and is reduced in hypertension. *Nat Commun*. 2018;9(1):4878. doi:10.1038/s41467-018-07318-3
22. Bown CW, Carare RO, Schrag MS, Jefferson AL. Physiology and clinical relevance of enlarged perivascular spaces in the aging brain. *Neurology*. 2022;98(3):107-117. doi:10.1212/WNL.0000000000013077
23. Ringman JM, Monsell S, Ng DW, et al. Neuropathology of autosomal dominant Alzheimer disease in the National Alzheimer Coordinating Center database. *J Neuropathol Exp Neurol*. 2016;75(3):284-290. doi:10.1093/jnen/nlv028
24. Sepulveda-Falla D, Villegas Lanau CA, White iii C, et al. Comorbidities in early-onset sporadic versus presenilin-1 mutation-associated Alzheimer disease dementia: evidence for dependency on Alzheimer disease neuropathological changes. *J Neuropathol Exp Neurol*. 2025;84(2):104-113. doi:10.1093/jnen/nlae122
25. Littau JL, Velilla L, Hase Y, et al. Evidence of beta amyloid independent small vessel disease in familial Alzheimer's disease. *Brain Pathol*. 2022;32(6):e13097. doi:10.1111/bpa.13097
26. Schoemaker D, Zanon Zotin MC, Chen K, et al. White matter hyperintensities are a prominent feature of autosomal dominant Alzheimer's disease that emerge prior to dementia. *Alz Res Ther*. 2022;14(1):89. doi:10.1186/s13195-022-01030-7
27. Schultz SA, Liu L, Schultz AP, et al. γ-Secretase activity, clinical features, and biomarkers of autosomal dominant Alzheimer's disease: cross-sectional and longitudinal analysis of the dominantly inherited Alzheimer network observational study (DIAN-OBS). *Lancet Neurol*. 2024;23(9):913-924. doi:10.1016/S1474-4422(24)00236-9
28. Fischl B. FreeSurfer. *Neuroimage*. 2012;62(2):774-781. doi:10.1016/j.neuroimage.2012.01.021
29. Frangi AF, Niessen WJ, Vincken KL, Viergever MA. Multiscale vessel enhancement filtering. In: Wells WM, Colchester A, Delp S, eds. *Medical Image Computing and Computer-Assisted Intervention — MICCAI'98*. Springer; 1998:130-137. doi:10.1007/BFb0056195
30. Puonti O, Iglesias JE, Van Leemput K. Fast and sequence-adaptive whole-brain segmentation using parametric Bayesian modeling. *NeuroImage*. 2016;143:235-249. doi:10.1016/j.neuroimage.2016.09.011
31. Araque Caballero MÁ, Suárez-Calvet M, Duering M, et al. White matter diffusion alterations precede symptom onset in autosomal dominant Alzheimer's disease. *Brain*. 2018;141(10):3065-3080. doi:10.1093/brain/awy229
32. Lynch KM, Sepehrband F, Toga AW, Choupan J. Brain perivascular space imaging across the human lifespan. *NeuroImage*. 2023;271:120009. doi:10.1016/j.neuroimage.2023.120009
33. Jia J, Ning Y, Chen M, et al. Biomarker changes during 20 years preceding Alzheimer's Disease. *N Engl J Med*. 2024;390(8):712-722. doi:10.1056/NEJMoa2310168
34. Klunk WE, Price JC, Mathis CA, et al. Amyloid deposition begins in the striatum of presenilin-1 mutation carriers from two unrelated pedigrees. *J Neurosci*. 2007;27(23):6174-6184. doi:10.1523/JNEUROSCI.0730-07.2007
35. McDade E, Kim A, James J, et al. Cerebral perfusion alterations and cerebral amyloid in autosomal dominant Alzheimer disease. *Neurology*. 2014;83(8):710-717. doi:10.1212/WNL.0000000000000721
36. Drachman DA, Smith TW, Alkamachi B, Kane K. Microvascular changes in Down syndrome with Alzheimer's-type pathology: insights into a potential vascular mechanism for Down syndrome and Alzheimer's disease. *Alzheimers Dement*. 2017;13(12):1389-1396. doi:10.1016/j.jalz.2017.05.003
37. Sepehrband F, Barisano G, Sheikh-Bahaei N, et al. Volumetric distribution of perivascular space in relation to mild cognitive impairment. *Neurobiol Aging*. 2021;99:28-43. doi:10.1016/j.neurobiolaging.2020.12.010
38. Wardlaw JM, Benveniste H, Nedergaard M, et al. Perivascular spaces in the brain: anatomy, physiology and pathology. *Nat Rev Neurol*. 2020;16(3):137-153. doi:10.1038/s41582-020-0312-z
39. Peng W, Achariyar TM, Li B, et al. Suppression of glymphatic fluid transport in a mouse model of Alzheimer's disease. *Neurobiol Dis*. 2016;93:215-225. doi:10.1016/j.nbd.2016.05.015
40. Kim SH, Ahn JH, Yang H, Lee P, Koh GY, Jeong Y. Cerebral amyloid angiopathy aggravates perivascular clearance impairment in an Alzheimer's disease mouse model. *Acta Neuropathol Commun*. 2020;8:181. doi:10.1186/s40478-020-01042-0
41. Suárez-Calvet M, Araque Caballero MÁ, Kleinberger G, et al. Early changes in CSF sTREM2 in dominantly inherited Alzheimer's disease occur after amyloid deposition and neuronal injury. *Sci Transl Med*. 2016;8(369):369ra178-369ra178. doi:10.1126/scitranslmed.aag1767
42. Wuerfel J, Haertle M, Waiczies H, et al. Perivascular spaces—MRI marker of inflammatory activity in the brain? *Brain*. 2008;131(9):2332-2340. doi:10.1093/brain/awn171
43. Ge Y, Law M, Herbert J, Grossman RI. Prominent perivenular spaces in multiple sclerosis as a sign of perivascular inflammation in primary demyelination. *AJNR Am J Neuroradiol*. 2005;26(9):2316-2319.

44. Ineichen BV, Okar SV, Proulx ST, Engelhardt B, Lassmann H, Reich DS. Perivascular spaces and their role in neuroinflammation. *Neuron*. 2022;110(21):3566-3581. doi:10.1016/j.neuron.2022.10.024
45. Ringman JM, Sachs MC, Zhou Y, Monsell SE, Saver JL, Vinters HV. Clinical predictors of severe cerebral amyloid angiopathy and influence of APOE genotype in persons with pathologically verified Alzheimer disease. *JAMA Neurol*. 2014;71(7):878-883. doi:10.1001/jamaneurol.2014.681
46. Zhao M, Li Y, Han X, et al. Association of enlarged perivascular spaces with cognitive function in dementia-free older adults: a population-based study. *Alzheimers Dement*. 2024;16(3):e12618. doi:10.1002/dad2.12618
47. Gogniat MA, Khan OA, Bown CW, et al. Perivascular space burden interacts with APOE-ε4 status on cognition in older adults. *Neurobiol Aging*. 2024;136:1-8. doi:10.1016/j.neurobiolaging.2024.01.002

SUPPORTING INFORMATION

Additional supporting information can be found online in the Supporting Information section at the end of this article.

How to cite this article: Leone R, Kobeleva X, Rowe B, Choupan J, Ringman JM, Barisano G. Alterations in MRI-visible perivascular spaces precede dementia diagnosis by 18 years in autosomal dominant Alzheimer's disease. *Alzheimer's Dement*. 2025;:e70588. https://doi.org/10.1002/alz.70588

3.2 Publication 2: White matter hyperintensities contribute to early cortical thinning in addition to tau in aging

Neurobiology of Aging 155 (2025) 66–77

Contents lists available at ScienceDirect

Neurobiology of Aging

journal homepage: www.elsevier.com/locate/neuaging.org

White matter hyperintensities contribute to early cortical thinning in addition to tau in aging

Riccardo Leone [a,b,c], Xenia Kobeleva [a,c,d,*], for the Alzheimer's Disease Neuroimaging Initiative[1]

[a] Computational Neurology Group, Faculty of Medicine, Ruhr University Bochum, Bochum 44801, Germany
[b] Faculty of Medicine, University of Bonn, Bonn 53127, Germany
[c] German Center for Neurodegenerative Diseases (DZNE), Bonn 53127, Germany
[d] Institute for Neural Computation, Ruhr University Bochum, Bochum 44801, Germany

ARTICLE INFO

Keywords:
WMH
Amyloid
Tau
Cortical thickness
Disconnections
Alzheimer's Disease
AD
Copathologies

ABSTRACT

White matter hyperintensities (WMH) are associated with cortical thinning in distant brain regions. However, it is currently unclear how WMH affect neurodegeneration in early Alzheimer's disease (AD). Here, we investigated associations between WMH and cortical thickness in temporal regions involved in early AD (AD cortical signature), while correcting for regional amyloid and tau accumulation assessed by PET. We performed cross-sectional (n = 551), and longitudinal (n = 125) analyses in older adults without dementia, also stratified by amyloid positivity. We evaluated WMH volume - as a measure of the global burden of WMH-related cerebrovascular pathology (GB-WMH) - and investigated the role of deep versus periventricular WMH. We also tested whether a higher focal burden of WMH in specific tracts connected to AD signature regions (FB-WMH) would lead to greater cortical thinning than expected solely from GB-WMH. We performed exploratory analyses in other brain regions to check the specificity of our findings to the temporal AD signature. GB-WMH damage, especially involving periventricular WMH, was cross-sectionally (not longitudinally) associated with cortical thinning in the fusiform, inferior and middle temporal gyri. Stronger associations were found in amyloid-positive individuals, including for the entorhinal cortex. Effects were mostly confined to regions of the temporal AD signature. FB-WMH did not yield higher cortical thinning than expected solely by GB-WMH. Cerebrovascular disease is associated with cortical thinning of temporal regions involved in early AD. Interventions aimed at improving cerebrovascular health might help to mitigate neurodegeneration in these regions.

1. Background

Neurodegenerative disorders are characterized by selective neuronal vulnerability, as evidenced by disease-specific cortical thinning patterns (Kampmann, 2024). In late-onset Alzheimer's disease (AD), a specific pattern of neurodegeneration - termed AD cortical signature - involving the entorhinal, fusiform, and inferior and middle temporal regions is seen at the early stage of the disease (Jack et al., 2015; Parker et al., 2020; Keuss et al., 2024). This AD cortical signature has been shown to predict future cognitive decline and AD dementia (Jack et al., 2015).

Various pathological processes contribute to neurodegeneration in AD. While the amyloid cascade hypothesis stresses the accumulation of misfolded amyloid-beta and tau proteins as the main drivers of neurodegeneration in AD (Musiek and Holtzman, 2015; Selkoe and Hardy, 2016), co-pathologies have been increasingly identified (Jack Jr. et al. 2024). Among co-pathologies, cerebrovascular disease is commonly observed in sporadic late-onset AD (Barisano et al., 2022; Garnier-Crussard et al., 2023; McAleese et al., 2017; Zhang et al., 2024). As cerebrovascular disease can be prevented and modified by lifestyle and medication (Verdelho et al., 2012), it is important to better understand its contribution in the context of amyloid and tau pathology in AD.

White matter hyperintensities (WMH) reflect cerebrovascular disease in vivo (Wardlaw et al., 2015) and are often observed in AD

* Correspondence to: Computational Neurology Group, Ruhr-Universität Bochum, Universitätsstraße 150, Bochum 44801, Germany.
E-mail address: xkobeleva@gmail.com (X. Kobeleva).

[1] Data used in preparation of this article was obtained from the Alzheimer's Disease Neuroimaging Initiative (ADNI) database (adni.loni.usc.edu). As such, the investigators within the ADNI contributed to the design and implementation of ADNI and/or provided data but did not participate in analysis or writing of this report. A complete listing of ADNI investigators can be found at: https://adni.loni.usc.edu/wp-content/uploads/how_to_apply/ADNI_Acknowledgement_List.pdf.

https://doi.org/10.1016/j.neurobiolaging.2025.07.007
Received 17 March 2025; Received in revised form 24 June 2025; Accepted 7 July 2025
Available online 9 July 2025

(Garnier-Crussard et al., 2023; Lee et al., 2016; Shirzadi et al., 2023). Despite their typical location within the deep and periventricular white matter (Wardlaw et al., 2015), WMH have been consistently associated with cortical thinning across the whole brain, suggesting a more widespread than purely local pathological mechanism (Bernal et al., 2024; Dadar et al., 2020; 2022; Lambert et al., 2016; Rizvi et al., 2021; Tuladhar et al., 2015; Zhang et al., 2024). Two main, non-mutually exclusive hypotheses have been suggested to explain the relationship between WMH and cortical thinning in distant regions. First, global pathological processes (e.g., neurovascular dysfunction) (Barisano et al., 2022; Ter Telgte et al., 2018; Low et al., 2019; Lorenzini et al., 2024) or shared genetic risk factors (Patel et al., 2024) might be associated with both the development of WMH and neuronal loss. Second, cortical thinning in WMH-connected cortical areas might arise from axonal degeneration following a focal injury in the location of WMH through white-matter tracts (Hao Li et al., 2023; Zhang et al., 2024). It is currently unclear whether global (i.e., whole-brain) WMH-related processes or focal axonal degeneration (i.e., starting from the WMH-induced lesion) are the main drivers of the association between WMH and cortical thinning.

In the context of AD pathological changes, the relationship between WMH and neurodegeneration is further complicated by the interaction between small vessel disease, and amyloid and tau. Some studies have shown that WMH may exacerbate cortical atrophy in individuals with reduced CSF levels of Aβ1–42 (Freeze et al., 2016; Lorenzini et al., 2024), while others report no significant interaction between regional amyloid burden and WMH in relation to cortical thinning (Keuss et al., 2022; 2024). Therefore, to better clarify these relationships, it is essential to investigate the association of WMH with neurodegeneration while simultaneously considering the regional accumulation of both amyloid and tau, as these pathologies may influence the effects of WMH on neurodegeneration.

In this study, we examined the cross-sectional and longitudinal associations between WMH and cortical thinning in older adults without dementia, also performing sub-analyses in amyloid-positive individuals. We focused on individual regions belonging to the AD cortical signature. We considered regional amyloid and tau deposition – as quantified by PET – and other important confounders, such as demography and

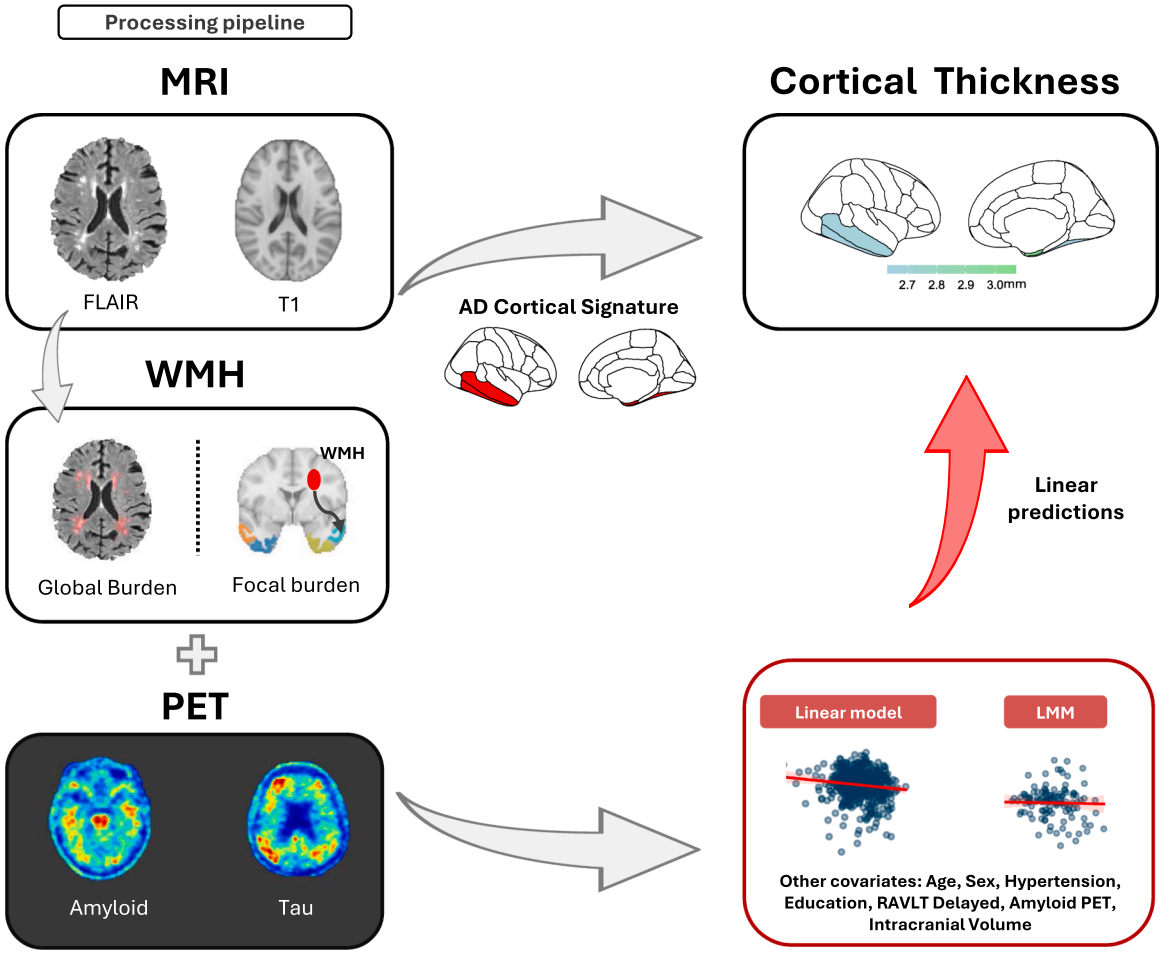

Fig. 1. Methodological Overview of the Study. We used a multimodal imaging dataset comprising MRI and PET data to evaluate the associations between white matter hyperintensities (WMH) and the individual cortical thickness of temporal regions (entorhinal, fusiform, inferior and middle temporal gyri) involved in early Alzheimer's disease (AD cortical signature), while controlling for regional PET amyloid and tau deposition, as well as other important covariates. T1-weighted MRI data was processed using Freesurfer to calculate regional cortical thickness of individuals regions belonging to the AD cortical signature. WMH were calculated using a previously developed deep learning algorithm. Their log-transformed volume was considered as a measure of global WMH damage. The WMH mask was transformed to MNI space and used as input for the Lesion Quantification Toolkit. By employing a normative white matter tracts atlas, LQT calculates a measure of disconnection for each region of interest, by considering the number of connections departing/arriving to that region that are damaged by WMH. Cross-sectional and longitudinal analyses were performed using linear regression and linear mixed-models (LMM), respectively. These analyses evaluated the association between the cortical thickness of each individual region belonging to the AD signature map and global or focal burden of WMH, separately, while correcting for regional tau and amyloid PET standardized uptake volume ratios, as well as age, sex, hypertension, years of education, Ray Auditory Verbal Learning Test (RAVLT) delayed scores, the type of amyloid tracer and total intracranial volume.

cardiovascular risk factors, in our models. We evaluated whether the association between WMH and cortical thickness depended upon the global burden of WMH (GB-WMH), whether this association varied upon the location of WMH (deep versus periventricular), and whether having an increased focal burden of WMH on specific white matter tracts connected to regions of the AD cortical signature may lead to their increased neurodegeneration compared to what expected solely from the global burden of WMH.

By investigating the role of WMH in driving early neurodegeneration in AD cortical signature regions, we aimed to contribute to the current pathological framework of AD and to clarify the role of vascular co-pathologies in the early stages of the disease.

2. Methods

The overall methodological workflow for this study is illustrated in Fig. 1. Data used in the preparation of this article was obtained from the Alzheimer's Disease Neuroimaging Initiative (ADNI) database (adni.loni.usc.edu). ADNI only included individuals in good health conditions, thus participants with a high burden of vascular disease (represented by a Hachinski score > 4) were not enrolled.

2.1. Ethical approval

The ADNI study protocol was approved by institutional review boards of all participating institutions, and written informed consent was obtained from all participants or their legal representatives at study sites. This study was conducted in accordance with the ethical principles of the Declaration of Helsinki. A list of all Ethics Committees/Institutional Review Boards involved in the ADNI study is presented in Supplementary Methods.

2.2. Participants

Demographic and imaging data from cognitively unimpaired (CU) individuals and individuals diagnosed with mild cognitive impairment (MCI) were downloaded from the ADNI website (www.adni.loni.usc.edu). Participants were selected based on the availability of both pre-processed regional amyloid and tau PET, as well as concomitant 3D-T1 and 3D-FLAIR MRI data for the same scan session, which all had to be acquired within a six-months period from each other. More specifically, PET data was pre-processed and made available on the ADNI website by the UC Berkeley team (see paragraph on PET data). We excluded participants not passing quality control, as performed by the UC Berkeley team and, for longitudinal evaluations, we also excluded individuals receiving different amyloid or tau PET tracers at different timepoints. Other exclusion criteria were radiological evidence of brain infarcts; diagnosis of dementia; severe motion artifacts in anatomical MRI or incomplete brain coverage, as determined by visual inspection during quality control; errors in the pre-processing pipeline or missing clinical covariates used for analyses. Furthermore, among covariates, two participants showed outlier values of Rey's Auditory Verbal Learning Test (RAVLT) delayed-recall scores (corresponding to z-scored values of -8 and -7.2, respectively) and were thus also excluded. A subset of individuals also had longitudinal PET and MRI data available. The full inclusion/exclusion flowchart is available in Supplementary Figure 1.

2.3. MRI acquisition

ADNI implemented a standardized and rigorously validated MRI protocol across its different sites. For this study, we only included participants with available 3D-T1 and 3D-FLAIR-weighted sequences acquired during the same session at a magnetic field strength of 3 T. High-resolution 3D T1-weighted magnetization-prepared, rapid acquisition gradient echo (MPRAGE) sequences were acquired with TR = 2300 ms, TEs = 2.9–3.2 ms, dimensions of 1x1x1 mm; 3D-FLAIR with TR = 4800 ms, TE = 119 ms, TI = 1348–1800 ms, dimensions 1.2x1x1mm.

2.4. Cortical thickness

To calculate cortical thickness, T1-weighted images were processed using FreeSurfer version 7.4.1 (Fischl, 2012) (Massachusetts General Hospital, Boston, MA) implemented via the FreeSurfer BIDS-App, first undergoing cross-sectional and then longitudinal processing (Reuter et al., 2012). The processing included the use of a robust, inverse consistent registration to create an unbiased within-subject template space and image (Reuter et al., 2012) and several other processing steps, such as skull stripping, Talairach transformations, atlas registration and spherical surface maps and parcellations using common information from the calculated within-subject template (Reuter et al., 2012). Cortical thickness maps for each region of the Desikan-Killiany atlas were created by combining the timepoint-specific data with the longitudinal templates.

2.5. Regions of interest

We focused our analyses on a subset of *a priori* defined cortical regions (temporal AD cortical signature), namely the entorhinal, fusiform, inferior, and middle temporal gyri, which were previously found to show reduced cortical thickness in early AD (Jack et al., 2015). Furthermore, cortical thinning in these regions predicted future cognitive decline in older adults without cognitive impairment (Jack et al., 2015). By focusing on these regions, we aimed to reduce the dimensionality of our analyses, while increasing the relevance of our findings to the earliest, potentially addressable, phases of the disease. However, to check the specificity of our findings to these temporal regions, we performed exploratory analyses in other cortical areas, either involved in AD (parahippocampal gyrus, temporal pole, inferior parietal gyrus, pars opercularis, pars orbitalis, pars triangularis, precuneus, supramarginal, superior parietal, superior frontal)(Lorenzini et al., 2024; Dickerson et al., 2011), or commonly not involved in AD (precentral and postcentral gyri). After averaging biomarkers values between hemispheres, we performed separate analyses for each individual region.

2.6. WMH segmentation and focal burden of WMH to the connected cortex

WMH segmentation was performed using a previously developed deep learning-based pipeline (Hongwei Li et al., 2018), implemented via the publicly available tool antspynet (Tustison et al., 2021). Total WMH volume was calculated in subject space. Periventricular (pvGB-WMH) and deep GB-WMH (dGB-WMH) were further classified based on their distance from the lateral ventricles: voxels within 10 mm of the ventricular surface were labeled as periventricular WMH, while those beyond this threshold were classified as deep WMH, consistent with standard anatomical definitions (Griffanti et al., 2018).

T1-weighted images were then registered to MNI space using *sMRIPrep* 0.16.0 (Esteban et al., 2024). T1w images were corrected for intensity non-uniformity with N4BiasFieldCorrection (Tustison et al., 2010), distributed with ANTs 2.5.3 (Avants et al., 2008), and used as T1w-reference throughout the workflow. The T1w-reference was then skull-stripped with a *Nipype* implementation of the antsBrainExtraction.sh workflow (from ANTs), using OASIS30ANTs as target template. Volume-based spatial normalization to one standard space (MNI152NLin6Asym) was performed through nonlinear registration with antsRegistration (ANTs 2.5.3), using brain-extracted versions of both T1w reference and the T1w template. The following template was selected for spatial normalization and accessed with *TemplateFlow* (24.2.0, (Ciric et al., 2022)): *FSL's MNI ICBM 152 non-linear 6th Generation Asymmetric Average Brain Stereotaxic Registration Model (MNI152NLin6Asym)*. The same transformation from subject to MNI space was applied to the WMH

mask and used as input for the analysis with the Lesion Quantification Toolbox (Griffis et al., 2021).

First, in the Lesion Quantification Toolkit, a normative structural connectivity matrix is generated by counting streamlines from a reference tractography atlas (HCP842 atlas; (Yeh et al., 2018)) between every pair of regions of the Desikan-Killiany parcellation. After this step, a subject-specific "disconnectivity" (Griffis et al., 2021) matrix is created using each participant's MNI-registered WMH lesion mask. For every pair of regions of the Desikan-Killiany parcellation, this matrix represents the percentage of streamlines overlapping with the WMH lesion mask out of the total number of streamlines connecting the two brain regions. From this matrix, the row-wise sum is calculated and then divided by the amount of non-zero elements in the same row, yielding a summary statistic of how each brain region is "disconnected" from the rest of the brain. Given that WMH might pathologically correspond to varying degrees of axonal damage, ranging from mild demyelination to full axonal loss (Ter Telgte et al., 2018), and not to full "disconnections", we refer to this variable as the focal burden of WMH to the connected cortex (FB-WMH).

2.7. PET data

The PET data used in this study was preprocessed and made publicly available by the UC Berkeley team on the ADNI website. Amyloid PET included tracers [18F] florbetaben and [18F] florbetapir, while tau PET data included the tracer [18F] flortaucipir. In brief, the preprocessing pipeline performed by the UC Berkely team included co-registration of PET scans to the corresponding MRI closest in time, intensity normalization by the whole cerebellum for amyloid PET, or inferior cerebellum for tau PET, and computation of the mean standardized uptake value ratio (SUVR, with partial volume correction for tau) for each region defined by the Desikan-Killiany atlas. Only regions in the AD cortical signature were considered and their left and right SUVR values were averaged. Tracer-specific amyloid positivity information was also provided by the UC Berkeley team based on the upper limit of cortical uptake in whole cerebellum-normalized SUVRs in young control samples (Landau et al., 2012; Royse et al., 2021).

2.8. Statistical methods

Descriptive statistics were used to characterize the study population, including the calculation of medians and interquartile ranges and frequencies for continuous and categorical variables, respectively. Due to its highly skewed distribution, WMH volume was log-transformed and is referred to as global burden of WMH (GB-WMH). FB-WMH damage similarly exhibited a skewed distribution and was log-transformed as well.

To explore the relationship between GB-WMH and FB-WMH, we calculated Spearman's correlation coefficients, which revealed strong to very strong correlations ($r = 0.60–0.85$). To address potential multicollinearity issues in subsequent analyses, we created a residualized FB-WMH measure for participants showing some degree (> 1 %) of FB-WMH damage by regressing out the effects of GB-WMH. The 1 % threshold was selected based on the hypothesis that some minimal level of FB-WMH should exist to potentially observe effects on cortical thickness of connected brain regions. Higher values of this residualized FB-WMH measure represent individuals with greater proportional accumulation of WMH in white matter pathways connected to regions of the AD signature, relative to their overall WMH load.

For cross-sectional analyses, we employed linear regression and evaluated the associations between each individual region cortical thickness with each WMH variable of interest, separately. Analyses were corrected for amyloid, tau and other potential confounders, such as age, sex, hypertension, years of education RAVLT scores, the type of amyloid tracer, and total intracranial volume. For longitudinal analyses, we employed linear mixed-effects models, with random intercepts for each participant to account for within-subject correlation. Fixed effects included the same covariates as the cross-sectional models, measured at baseline, with the addition of time (years from baseline) and its interaction with the WMH variable of interest. In longitudinal analyses, we focused on this interaction to assess the contribution of baseline WMH on cortical thickness changes over time. Analyses were performed in the whole cohort, as well as in amyloid-positive individuals only. We also performed analyses stratified by cognitive status (CU and MCI). All tables report regression coefficients and 95 % confidence intervals for unstandardized variables. To compare the effect size of the WMH measures between regions of the AD cortical signature and other brain regions, as well as between different cognitive status, we used standardized beta coefficients in related figures.

Initial descriptive analyses of FB-WMH focused on the original FB-WMH metrics (not residualized) to provide a clear picture of how WMH affect white matter tracts and connected cortical regions. For regression analyses, we employed the residualized FB-WMH measure as the variable of interest, with analyses restricted to subjects showing some degree of FB-WMH (> 1 % FB-WMH). In these analyses, cortical thickness was modeled as a function of both GB-WMH burden and the residualized FB-WMH measure, along with all relevant covariates.

Statistical analyses were conducted mainly using the *statsmodels* package in Python. To compare the relative importance of different variables in our models, we used the package *relaimpo,* implemented in R, employing the Lindemann, Merenda and Gold (LMG) method. LMG decomposes the explained variance into unique components linked to each predictor by averaging the sequential sum of squares over all possible orderings of predictors, thereby providing a robust measure of each variable's contribution to the explained variance (Groemping, 2007).

For analysis of our *a priori* defined regions of the temporal AD cortical signature, false-discovery rate (FDR) correction was applied to control for multiple comparisons; statistical significance was set at two-tailed FDR-$p < 0.05$ after correction**.** Additionally, to investigate the specificity of our findings to these temporal regions, we conducted exploratory analyses across other brain regions (see paragraph *Regions of Interest*), which were not corrected for multiple comparisons.

3. Results

Demographic baseline information for the whole cohort and for the

Table 1
Participants demographics.

Variable	All (n = 551)	Amyloid-positive (n = 201)
Age (years)	71.7 ± 7.3	73.3 ± 7.0
Education (years)	16.00 (15.00–18.00)	16.00 (15.00–18.00)
MMSE	29.00 (28.00–30.00)	29.00 (27.00–30.00)
WMH volume (log)	2.95 (2.52–3.36)	3.03 ± 0.61
Deep WMH vol. (log)	2.22 (1.73–2.66)	2.23 (1.76–2.70)
PV WMH vol. (log)	2.93 (2.43–3.39)	2.98 (2.46–3.41)
RAVLT	4.00 (2.00–6.00)	5.00 (3.00–6.00)
Sex		
Female	302 (54.8 %)	115 (57.2 %)
Male	249 (45.2 %)	86 (42.8 %)
Cognitive status		
CU	350 (63.5 %)	102 (50.7 %)
MCI	201 (36.5 %)	99 (49.3 %)
Amyloid Status		
Negative	350 (63.5 %)	//
Positive	201 (36.5 %)	//

Demographics summary statistics are presented for the whole cohort and for the amyloid-positive subgroup. Continuous variables are expressed as mean ± standard deviation or median (interquartile range), based on normality tests. Categorical variables are shown as counts and percentages.
Abbreviations: MMSE = Mini-Mental State Examination; WMH = white matter hyperintensity; CU = Cognitively Unimpaired; MCI = Mild Cognitive Impairment; RAVLT = Ray Auditory Verbal Learning Task (delayed recall).

amyloid-positive subgroup are provided in Table 1. After exclusions, 551 participants (aged 71.7 ± 7.3 years, 54.8 % female, 63.5 % without cognitive impairment) were included for cross-sectional analyses. Among them, 201 individuals (aged 73.3 ± 7.0 years, 57.2 % females, 50.7 % without cognitive impairment) were considered amyloid-positive according to a predefined cutoff.

3.1. Description of the focal burden of WMH to the connected cortex

We first describe the distribution of FB-WMH across the AD cortical signature regions (Fig. 2A, upper panel). Overall, WMH were observed in less than 10 % of all white matter tracts (i.e., 10 % of the study's sample tracts) connected with each temporal AD signature region, with the highest average FB-WMH found in tracts connected to the middle temporal gyrus. When aggregating across all AD signature regions, most WMH were located on tracts connecting these regions with the frontal lobe, followed by the parietal lobe (Fig. 2B). At the individual tract level (Fig. 2C), the highest FB-WMH was observed between the right inferior temporal gyrus and the left superior parietal gyrus (FB-WMH = 0.41). High levels of WMH were also found on tracts linking the right fusiform gyrus with the left inferior temporal gyrus (FB-WMH = 0.27) and the left entorhinal cortex with the right pars triangularis (FB-WMH = 0.23). Exploratory analyses of additional cortical regions revealed comparable FB-WMH levels, with somewhat higher involvement in the superior frontal, precentral and supramarginal gyri (Fig. 2A, lower panel).

3.2. GB-WMH damage is a significant contributor to neurodegeneration in AD cortical signature regions in the general population

We next assessed associations between GB-WMH and cortical thickness in individual regions from the AD cortical signature, while controlling for regional amyloid and tau accumulation and other relevant covariates, including age and hypertension (Fig. 3A). When considering the whole cohort, GB-WMH damage was significantly associated with cortical thinning in the fusiform (β = −0.025, 95 % CI: −0.041 to −0.008, FDR-p = 0.013), inferior temporal (β = −0.02, 95 % CI: −0.037 to −0.002, FDR-p = 0.036) and middle temporal (β = −0.02, 95 % CI: −0.037 to −0.004, FDR-p = 0.030), but not in the entorhinal cortex (β = −0.013, 95 % CI: −0.051–0.025, FDR-p = 0.50) (Table 2A). As expected, tau was significantly associated with reduced cortical thickness in all regions from the AD cortical signature (all FDR-p < 0.0001). Amyloid was positively associated with cortical thickness in the entorhinal (FDR-p = 0.019) and fusiform (FDR-p = 0.028) regions, but not with the cortical thickness of other regions (FDR-p > 0.8). We assessed the relative importance of each biomarker for explaining variance in cortical thickness (Supplementary Fig. 2, Supplementary Table 1). Tau was the most important predictor in all regions (relative importance range: 73.9 % - 94.8 %). For the fusiform, inferior and middle temporal gyri, GB-WMH explained more variance (13.6–16.7 %) than amyloid (6.4–12.5 %), while in the entorhinal cortex both amyloid (4.1 %) and GB-WMH (1.1 %) had minor contribution. Furthermore, we obtained estimates of the relative importance of GB-WMH in relation to tau by calculating the ratio of GB-WMH variable importance to that of tau. This analysis showed GB-WMH having up to 22.1 % the relative importance of tau (Supplementary Table 1).

We performed further analyses separating GB-WMH into its periventricular and deep components (Fig. 3A, Supplementary Table 2–3). Results showed that pvGB-WMH largely reproduced the associations observed with GB-WMH - namely, significant negative relationships with cortical thickness in the fusiform, inferior and middle temporal regions - whereas dGB-WMH did not show significant associations with any region. No associations were observed between FB-WMH and cortical thickness (Supplementary Table 4).

To assess the anatomical specificity of the observed associations, we

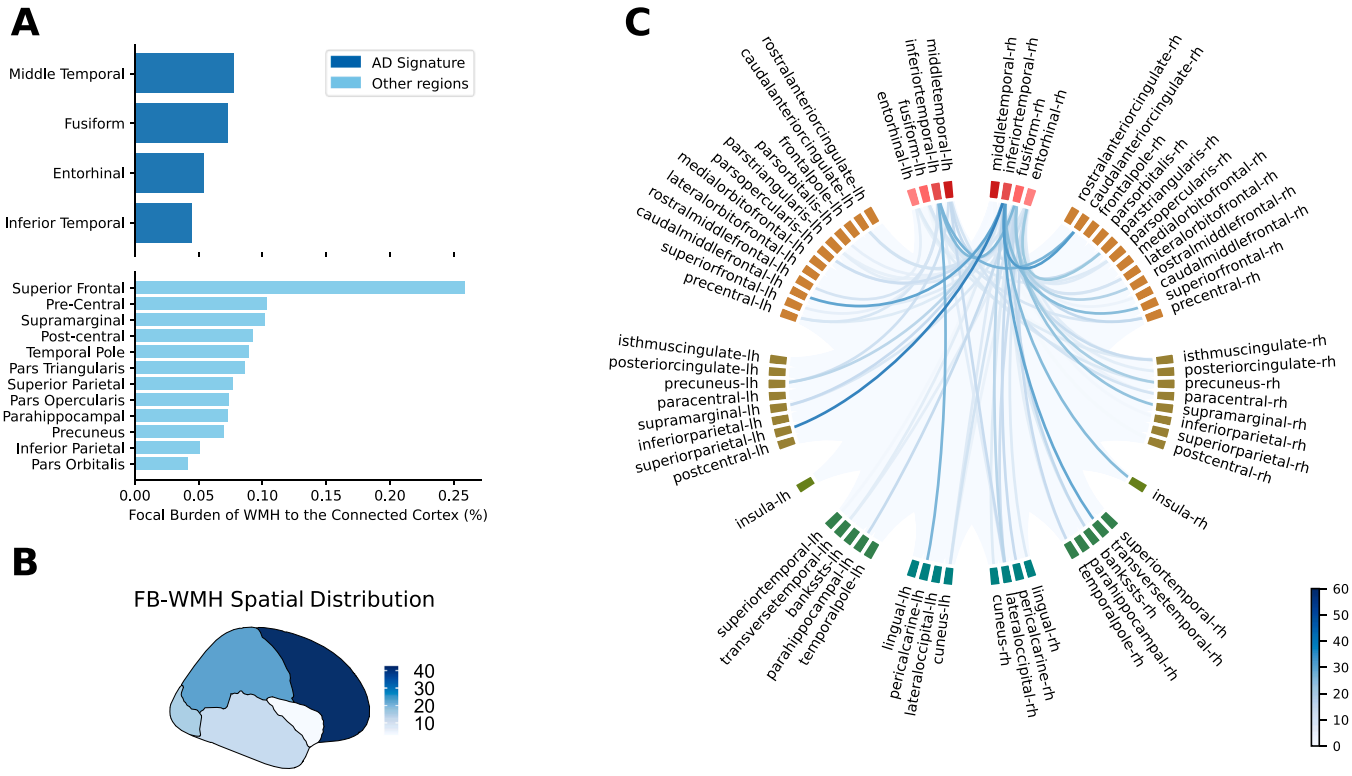

Fig. 2. Spatial distribution and focal burden of WMH to the connected cortex (FB-WMH). (A) Cortical regions receiving connected to tracts with the highest focal burden of WMH, measured as the percentage of intersection between WMH and streamlines connected to each cortical region. Temporal AD cortical signature regions are depicted in dark blue. (B) The spatial distribution of FB-WMH from AD cortical signature reginos to the rest of the cortex, darker shades indicate higher proportional burden (%). (C) Circular connectogram illustrating white matter tracts damaged by WMH. AD signature regions are shown in red, and connection strength is color-coded by FB-WMH (%).

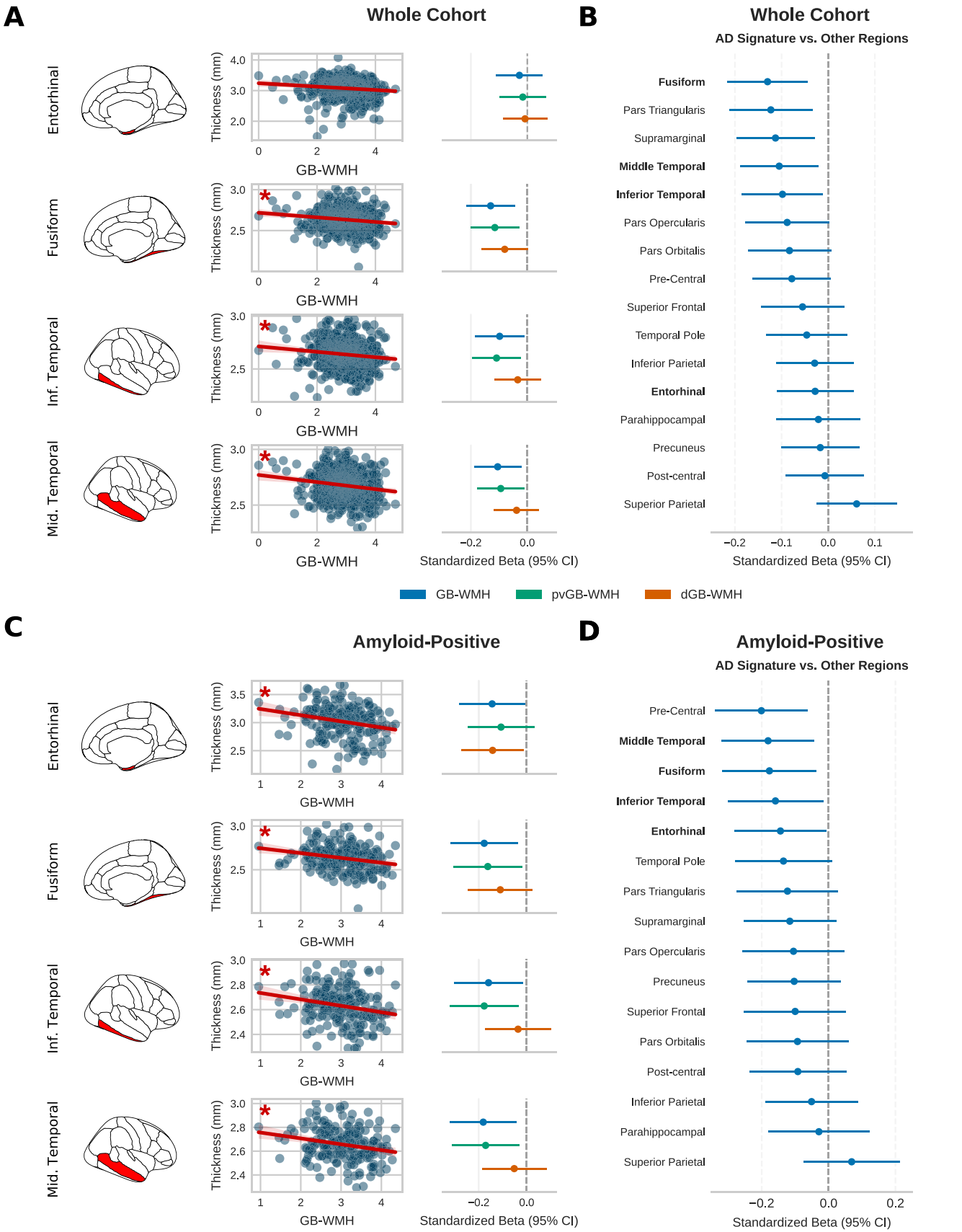

(caption on next page)

Fig. 3. Cross-sectional associations between global burden of WMH (GB-WMH) and cortical thickness in the whole cohort and in amyloid-positive individuals. Scatter plots depict the cross-sectional relationships between GB-WMH and cortical thickness for each individual region belonging to the AD cortical signature (pictorially illustrated in the first column, one region for each row) for the whole cohort (A) and for amyloid-positive individuals (C). For illustrative purposes univariate regression lines between global- and axonal-WMH damage and cortical thickness, together with 95 % confidence intervals (shaded areas) are depicted in red. Significant associations from the fully adjusted multivariate model are marked by a red asterisk in each individual panel. The forest plots in (A) and (C) represent the standardized regression coefficients obtained from linear regression employing either the total GB-WMH (in blue) or only the periventricular GB-WMH (pvGB-WMH, in green) or deep GB-WMH (dGB-WMH, in orange). (B–D) The forest plots illustrate standardized regression coefficients obtained from linear regression employing performed in the AD temporal cortical signature (regions in bold) and in other regions that were considered to check the specificity of the found effects to the temporal lobe. Results for the whole cohort are presented in (B) and for amyloid-positive individuals in (D).

Table 2
Results of cross-sectional linear regression analyses between cortical thickness and global burden of WMH.

A) Whole cohort (n = 551)						
	GB-WMH		**Amyloid**		**Tau**	
Region	**Beta (95 % CI)**	**FDR-p**	**Beta (95 % CI)**	**FDR-p**	**Beta (95 % CI)**	**FDR-p**
Entorhinal	−0.013 (−0.051, 0.025)	0.50	0.307 (0.094, 0.520)	**0.019**	−0.319 (−0.379, −0.259)	**p < 0.0001**
Fusiform	−0.025 (−0.041, −0.008)	**0.013**	0.074 (0.015, 0.133)	**0.028**	−0.092 (−0.119, −0.065)	**p < 0.0001**
Inferior temporal	−0.020 (−0.037, −0.002)	**0.036**	0.011 (−0.042, 0.064)	0.82	−0.063 (−0.090, −0.037)	**p < 0.0001**
Middle temporal	−0.020 (−0.037, −0.004)	**0.03**	−0.006 (−0.056, 0.044)	0.82	−0.074 (−0.101, −0.047)	**p < 0.0001**
B) Amyloid-positive (n = 201)						
	GB-WMH		**Amyloid**		**Tau**	
Region	**Beta (95 % CI)**	**FDR-p**	**Beta (95 % CI)**	**FDR-p**	**Beta (95 % CI)**	**FDR-p**
Entorhinal	−0.068 (−0.132, −0.003)	**0.039**	0.132 (−0.184, 0.448)	0.62	−0.230 (−0.306, −0.153)	**p < 0.0001**
Fusiform	−0.042 (−0.076, −0.009)	**0.028**	0.040 (−0.063, 0.143)	0.62	−0.097 (−0.131, −0.062)	**p < 0.0001**
Inferior temporal	−0.037 (−0.070, −0.004)	**0.039**	−0.027 (−0.117, 0.062)	0.62	−0.068 (−0.100, −0.037)	**p < 0.0001**
Middle temporal	−0.040 (−0.071, −0.009)	**0.028**	−0.022 (−0.111, 0.067)	0.62	−0.083 (−0.115, −0.050)	**p < 0.0001**

Coefficients and false-discovery-rate-corrected p-values (FDR-p) for linear regressions testing the association between cortical thickness (dependent variable) and global burden of WMH (GB-WMH) in each region of interest of the AD cortical signature. Results are presented first for the whole cohort and then for the amyloid-positive subgroup. Other covariates included age, sex, hypertension, years of education, Ray Auditory Verbal Learning Test (delayed recall) scores, total intracranial volume and amyloid tracer. Significant FDR-p values are highlighted in bold.

compared the strength of the relationship between GB-WMH and cortical thickness across AD signature regions and a broader set of cortical areas (Fig. 3C, Supplementary Table 5). Among all regions examined, the fusiform cortex exhibited the strongest association with GB-WMH, followed by the pars triangularis, supramarginal gyrus, middle temporal gyrus, and inferior temporal gyrus. Other regions outside of the temporal AD cortical signature did not show statistically significant unadjusted associations.

We then performed stratified analyses by cognitive status (Supplementary Fig. 3, Supplementary Table 6). When considering the whole cohort, we found consistently more negative standardized regression coefficients in individuals with MCI compared to CU participants for the fusiform, inferior temporal and middle temporal gyri, although these did not survive FDR correction (FDR-p = 0.06). An exception to this was the entorhinal cortex, where the strength of the negative association was greater in CU individuals. When stratified by cognitive status, the previously observed positive association between amyloid and entorhinal thickness was present only in MCI, while a negative association emerged for CU participants. Additionally, significant negative associations between tau and cortical thinning were only observed in individuals with MCI.

3.3. GB-WMH relates to stronger cortical thinning in amyloid-positive individuals

We then performed analyses in the amyloid-positive group, defined according to a previously validated cortical summary region of interest (Fig. 3C, Table 2B). In amyloid-positive subjects, significant associations were found for the fusiform (β = −0.042, 95 % CI: −0.076 to −0.009, FDR-p = 0.028), inferior (β = −0.037, 95 % CI: −0.07 to −0.004, FDR-p = 0.039), middle temporal (β = −0.040, 95 % CI: −0.071 to −0.009, FDR-p = 0.028) gyri, and for the entorhinal cortex (β = −0.068, 95 % CI: −0.132 to −0.003, FDR-p = 0.039). Also in amyloid-positive individuals tau showed a significant negative association with cortical thinning in all regions (all FDR-p < 0.0001). Amyloid did not show any significant association with the cortical thickness of any region in this subgroup (all FDR-p > 0.6). In amyloid-positive individuals, the relative importance of GB-WMH increased in all regions compared with the general population (12.4 % for the entorhinal, 16.6 % for the fusiform, 18.2 % for the inferior temporal, and 17.5 % for the middle temporal) (Supplementary Fig. 2, Supplementary Table 1). The relative importance of GB-WMH in relation to tau increased to 25.4 % for the inferior temporal gyrus.

Analyses of pvGB-WMH showed significant negative associations with all regions except for the entorhinal thickness. dGB-WMH was not associated with cortical thickness in any region after FDR correction (Supplementary Table 2–3). No associations were observed between FB-WMH and cortical thickness (Supplementary Table 4).

When comparing associations in the temporal AD cortical signature regions with other regions, we found the strongest association between GB-WMH and cortical thinning in amyloid-positive individuals in the pre-central gyrus (Fig. 3D, Supplementary Table 5). Other significant associations were limited to regions within the temporal AD cortical signature and no other regions outside the AD signature showed statistically significant associations.

When stratifying the amyloid-positive subgroup by cognitive status, for CU individuals, we observed negative significant associations (which survived FDR-correction) between GB-WMH and cortical thickness in the entorhinal and middle temporal gyri (Supplementary Fig. 3, Supplementary Table 7). Standardized beta coefficients were more negative in CU participants – except for the fusiform cortex - although confidence intervals overlapped. The association between tau and cortical thickness was statistically significant only in MCI.

3.4. GB-WMH and FB-WMH damage are not associated with longitudinal cortical thinning

A subset of individuals also had available longitudinal data (n = 125, median follow-up of 2.5 years [IQR 2–4]). In these participants, we assessed whether baseline WMH measures were associated with the longitudinal rate of change of cortical thickness, while controlling for the same covariates at baseline. No WMH measures at baseline were significantly associated with cortical thickness in any region of the AD cortical signature in the whole cohort nor in amyloid-positive participants (Fig. 4, Supplementary Table 8–10).

4. Discussion

In this study, we used a multimodal imaging approach to examine the relationship between WMH and cortical thickness in four brain regions that comprise the previously defined temporal AD cortical signature. Consistent with prior findings, tau pathology was the strongest predictor of neurodegeneration. However, we observed that greater global WMH burden - particularly in periventricular areas - was cross-sectionally associated with reduced cortical thickness in these temporal regions, even after adjusting for local amyloid and tau deposition. These associations were primarily confined to temporal cortices, although other brain regions with relatively low tau burden exhibited significant WMH-related cortical thinning. The relationship between WMH and cortical thinning was stronger in amyloid-positive individuals, particularly for the entorhinal cortex. We found stronger associations between GB-WMH and cortical thinning in CU amyloid-positive individuals compared with MCI. A high focal burden of WMH along white matter tracts connected to AD signature regions did not contribute to neurodegeneration beyond what expected from the global burden of WMH. Baseline WMH did not predict longitudinal cortical thinning, possibly due to the short follow up of the study and the stronger effects of tau-related neurodegeneration. These findings underscore the contribution of cerebrovascular pathology to cortical atrophy in early AD and suggest a potential vascular dysfunction pathway that might influence early structural brain changes, especially in the presence of elevated amyloid.

Neurodegeneration in specific temporal regions is a key feature of early AD, which is linked to the subsequent development of cognitive decline and dementia (Jack et al., 2015; Keuss et al., 2024). According to the amyloid cascade hypothesis, the regional accumulation of amyloid

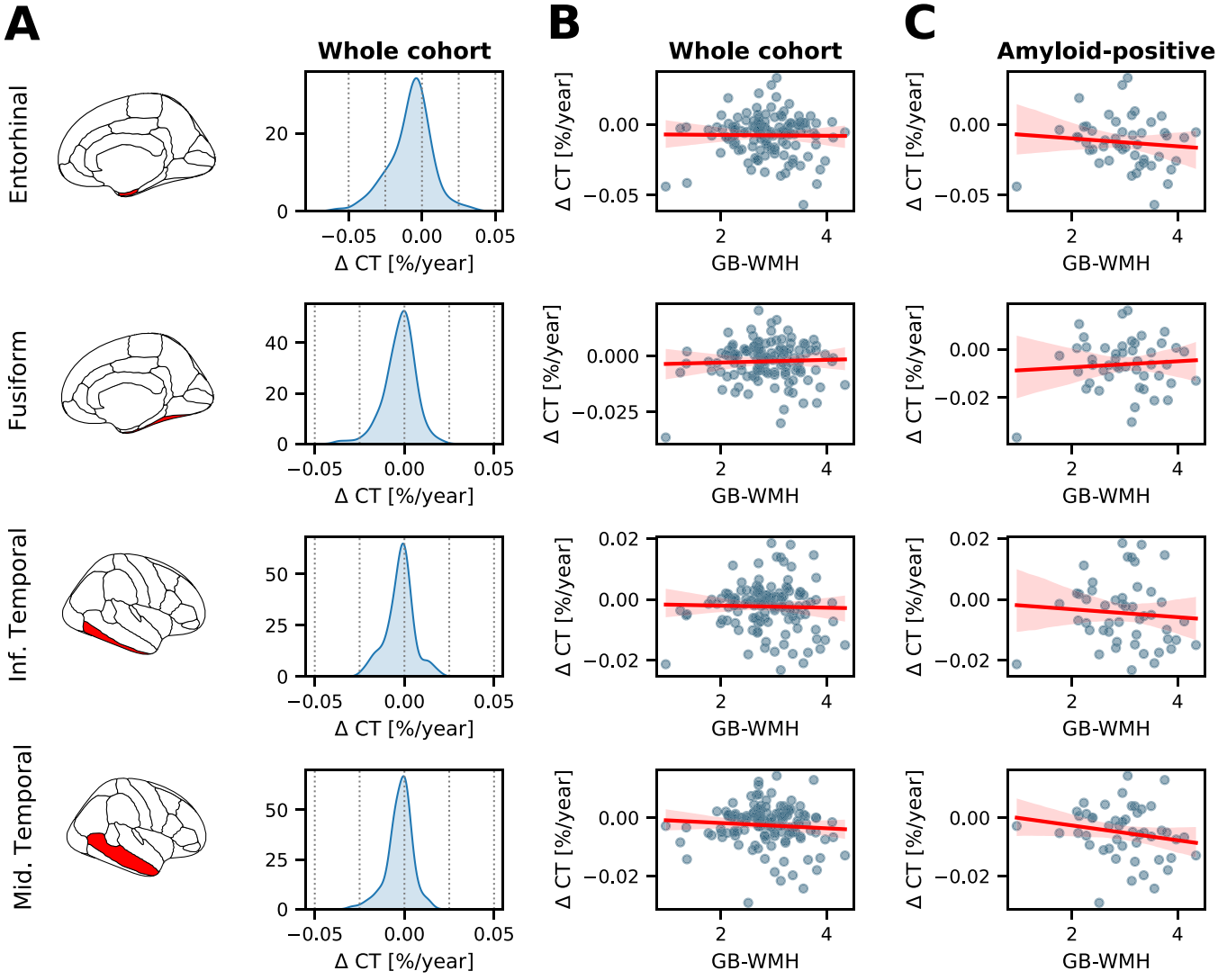

Fig. 4. Longitudinal associations between global burden of WMH (GB-WMH) and cortical thickness in the whole cohort and in amyloid-positive individuals. The first column pictorially illustrates the brain region considered for each row. Distribution of the annualized percent rate of cortical thickness change for each region in the whole cohort (A). Scatter plots of the relationship between GB-WMH and the annualized percent rate of cortical thickness change for each region in the whole cohort, with univariate regression lines and 95 % confidence intervals (shaded areas) shown in red (B). The same is shown for amyloid-positive individuals (C).

leads to the subsequent aggregation of hyperphosphorylated tau, which in turns drives pattern-specific neurodegeneration (Musiek and Holtzman, 2015; Selkoe and Hardy, 2016). Possible associations between neurodegeneration and other co-pathologies, such as WMH, have been traditionally less well explored. In this study, we found that WMH are associated with significant cortical thinning in AD cortical signature temporal regions even after adjusting for levels of regional amyloid and tau accumulation. While tau pathology remained the strongest predictor of cortical thinning across all AD signature regions - consistent with its established role in driving local atrophy - GB-WMH explained a substantial proportion of the remaining variance, particularly in the fusiform, inferior temporal, and middle temporal gyri. In these regions, the explanatory power of GB-WMH exceeded that of amyloid and amounted to approximately 22 % of the relative importance of tau. Additionally, we found stronger associations between WMH and cortical thinning in amyloid-positive individuals, with a significant effect also observed in the entorhinal cortex. Therefore, our results suggest that WMH may play a relevant role in the early neurodegeneration of these temporal regions, especially in amyloid-positive individuals, leading to significantly more neuronal loss than expected due to amyloid and tau alone.

To assess the anatomical specificity of these findings, we conducted exploratory analyses in both other AD-relevant (Dickerson et al., 2011) and non-AD-related cortical regions. Among the five regions with unadjusted significant associations between GB-WMH and cortical thinning, three were part of the original AD temporal signature. The other two - pars triangularis and supramarginal gyrus - are not core temporal regions but are implicated in AD at later disease stages (Insel et al., 2020). In amyloid-positive individuals, these effects became more localized to the temporal cortex, with only the precentral gyrus - an area not typically affected by tau - showing a significant WMH-related association (Patel et al., 2024). These findings suggest that, while GB-WMH is associated with cortical thinning across various brain regions, this association may be more relevant for AD-vulnerable regions in the temporal lobe, particularly in the presence of elevated amyloid or tau levels.

Previous studies suggested an association between WMH and cortical thinning of specific AD-related regions both in the general population (Rizvi et al., 2021) and in amyloid-positive individuals (Keuss et al., 2024; 2022). Furthermore, WMH were associated with more diffuse patterns of neurodegeneration involving several brain regions in amyloid-positive individuals (Zhang et al., 2024). Another study observed that individuals with late-onset AD at any AT stage, who showed neurodegeneration, had a higher volume of WMH compared to the same category without neurodegeneration (Jack et al., 2017). Moreover, WMH partially explained the mismatch between tau accumulation and regional neurodegeneration (Lyu et al., 2024) - specifically, larger than expected neurodegeneration when predicted by tau alone. Our study extends this previous research by demonstrating the contribution of WMH on cortical thickness, while accounting for the precise regional accumulation of amyloid and tau assessed by PET.

While our study was limited to standard anatomical imaging, preventing direct assessment of underlying pathological mechanisms, the association between GB-WMH and cortical thinning suggests that WMH might serve as markers of diffuse cerebrovascular dysfunction affecting both the formation of WMH and early neurodegeneration in AD-vulnerable temporal regions (Garnier-Crussard et al., 2023; Bachmann et al., 2024; Eisenmenger et al., 2023; Kisler et al., 2017). Various biological pathways, including shared genetic risk factors (Patel et al., 2024), may explain this association. For example, hypoperfusion might be linked to both the development of WMH and cortical thinning via hypoxia (Dalby et al., 2019), while increased permeability in the blood-brain barrier has been linked to hippocampal atrophy (Barisano et al., 2022) and it has been described in WMH (Zhang et al., 2019). Interestingly, we found that the association between WMH and cortical thinning may occur at different cognitive stages depending on amyloid-positivity. For instance, when we analyzed the amyloid-positive group stratified by cognitive status, we found a stronger negative association between GB-WMH and cortical thinning in CU compared to MCI individuals. This was in contrast with associations in the whole cohort, where – with the exception of the entorhinal cortex – we found stronger negative associations in individuals with MCI. Although these findings did not survive multiple comparisons correction and should thus be interpreted with caution, they suggest that WMH may be associated with different pathological processes occurring in the initial stages of the disease in amyloid-positive individuals (i.e., by being more linked to AD-specific than only vascular pathology). It is still unclear whether cerebrovascular alterations are an integral part of AD pathophysiology or just occurring in parallel (Eisenmenger et al., 2023). Previous reports of early alterations in cerebral blood flow (Eisenmenger et al., 2023; Falcon et al., 2024) as well as increased permeability of the blood-brain-barrier (Barisano et al., 2022) in individuals in the early stages of AD suggest that an intrinsic pathological component involving the vascular/perivascular compartment might be present in AD. Future studies incorporating specific vascular biomarkers, such as perfusion measures, microstructural imaging, or blood-brain barrier integrity markers, are needed to provide more comprehensive insights into the mechanisms linking global WMH with cortical thinning in AD signature regions and to further investigate potential differences in pathological processes occurring in cognitively unimpaired amyloid-positive versus mildly cognitively impaired amyloid-negative individuals.

We performed sub-analyses to better understand the effects of periventricular versus deep GB-WMH. We found significant relationships only between pvGB-WMH and cortical thinning. While some studies suggest that periventricular and deep WMH only represent different stages of the same pathological process (DeCarli et al., 2005; Wardlaw et al., 2015), our findings align with other studies suggesting distinct anatomopathological characteristics based on lesion location, with periventricular WMH showing greater white matter damage (Murray et al., 2012). The differential genetic associations - periventricular WMH linked to vascular dysfunction genes while deep WMH associate with glial dysfunction genes (Armstrong et al., 2020) further support mechanistic distinctions that may explain why periventricular WMH specifically drive the observed associations with cortical thinning.

Throughout this study, we investigated whether FB-WMH along white matter tracts anatomically connected to temporal AD cortical regions contributes to cortical thinning beyond what is expected from the global burden of WMH. Our results showed that the temporal regions comprising the AD cortical signature were only moderately affected by tract-specific WMH, with fewer than 10 % of the study's sample tracts in the temporal AD cortical regions intersected by WMH. Among the affected tracts, most were interhemispheric and linked the temporal cortex to frontal and parietal regions. We did not find associations between FB-WMH and cortical thinning. We cannot completely exclude that part of the effect of GB-WMH on neurodegeneration might happen through white matter degeneration. However, our results suggest that axonal degeneration per se is not the predominant mechanism of WMH-related cortical atrophy in early-stage AD, but other potential processes such as hypoxia (Dalby et al., 2019) and blood-brain-barrier disruption (Barisano et al., 2022) might be more likely involved. These findings are apparently in contrast with a recent study by Zhang et al. (2024) in amyloid-positive individuals, which reported reduced cortical thickness in regions structurally connected to WMH-affected tracts compared to WMH-unconnected cortex. However, several methodological and conceptual differences may explain the discrepancy. First, our study targeted a focused set of temporal regions associated with early AD pathology, while Zhang et al. conducted a whole-brain analysis, identifying WMH-connected cortical thinning primarily in frontal and parietal areas. Second, the disease stage of participants differed: over half of Zhang et al.'s sample was diagnosed with dementia, suggesting a later disease stage compared to our cohort, which only included CU and MCI participants. Taken together, these results imply that the relationship between WMH and cortical thinning may evolve over the course of the

disease. For instance, global cerebrovascular pathology may be more relevant for early-stage temporal neurodegeneration, whereas tract-specific WMH-induced axonal damage could become more prominent at later stages.

Our results support proposals to expand the AT(N) framework (Jack Jr. et al. 2024; Chun et al., 2023), incorporating vascular contributions (v) as an additional possible mechanism of neurodegeneration (Barisano et al., 2022; Chun et al., 2023). An extended ATVN model could move forward AD research and clinical care. For example, accounting for vascular contributions to neurodegeneration may potentially explain some of the heterogeneity in neurodegeneration patterns observed across different individuals (Lyu et al., 2024). This extended framework could guide the development of more personalized intervention strategies targeting additional pathways besides amyloid and tau and making use of available treatments for cerebrovascular disease (e.g., lifestyle changes).

Although not the primary focus of the study, we found a bidirectional association between amyloid-beta and entorhinal cortical thickness, which depended on cognitive status. In CU individuals, we found a negative relationship between amyloid and cortical thinning, while a strong positive relationship was observed in MCI participants. Although the entorhinal cortex is not a common site of increased amyloid deposition in the initial stages of AD, amyloid-related processes could have detrimental effects in driving early neurodegeneration in this region, a finding that should be further investigated in future studies. The positive association observed in latter stages and in the fusiform gyrus is possibly attributed to the space-occupying effect of amyloid plaques or local fluid increase due to amyloid-related inflammation, as previously reported (Chételat et al., 2010; Oh et al., 2014; Harrison et al., 2021).

We found that WMH were not associated with longitudinal rates of cortical thinning neither in the whole cohort nor in amyloid-positive individuals. Most previous studies (Keuss et al., 2024; Bernal et al., 2024; Rizvi et al., 2021; Luo et al., 2023), with the exception of Dickie et al. (2016), have reported significant associations between baseline WMH and the longitudinal rate of cortical thinning in AD-related regions. However, these studies did not consider the contribution of WMH together with combined regional amyloid and tau deposition. A possible explanation for the lack of significant findings in our cohort is that the rate of cortical thinning may be more strongly associated with tau, and the effects of tau may overshadow in the model the subtler impact of WMH. A recent study has shown that WMH may affect tau deposition (indirectly via amyloid), thus it is possible that the effects of WMH on neurodegeneration may occur through increased tau deposition (Lorenzini et al., 2024), although this effect may mostly relate to microbleeds-associated WMH (Graff-Radford et al., 2019). Another possible explanation is that neurodegeneration due to WMH might happen over longer timescales than the relatively short follow-up time in our sample (~2.5 years), while tau-related neurodegeneration might be more direct and thus observable within a shorter time frame. We speculate that the lack of significant longitudinal findings in the amyloid-positive subgroup might be linked to the relatively low power of this analysis. Future studies should account for longer follow-up times and include more amyloid-positive individuals, while also considering possible interaction effects between WMH and tau in driving longitudinal cortical thinning.

4.1. Limitations

There are some limitations to be considered for this study. First, the computation of FB-WMH was performed using a normative white matter tracts atlas based on healthy individuals and not using subject-specific diffusion-tensor imaging data (Griffis et al., 2021). This precluded us from evaluating the specific FB-WMH using subject-specific white matter tract reconstructions. Nonetheless, it allowed us to evaluate stable features of the population-level white matter anatomy, possibly reducing the rate of false positive connections observed in diffusion MRI tractography analyses (Griffis et al., 2021). Moreover, ADNI only recruited individuals without substantial vascular damage (modified Hachinksi score ≤ 4), so participants with elevated levels of WMH are underrepresented in our sample. Given that WMH correspond to various degrees of pathological damage, ranging from demyelination to axonal loss (Ter Telgte et al., 2018), future studies should aim to assess whether longitudinal cortical thinning – possibly due to axonal degeneration - might be observed in individuals with higher burdens of WMH. Furthermore, our results are based on neuroimaging, thus we could only assess cerebrovascular pathology or axonal degeneration indirectly through imaging biomarkers. Future studies addressing post-mortem pathological samples are needed to further validate our findings and provide a more comprehensive understanding of the underlying pathological mechanisms associating WMH to early neurodegeneration in AD. Finally, while we showed an association between WMH and neurodegeneration, it is important to acknowledge that the directionality of this association cannot be definitively determined from this study. While, similarly to many previous studies (Keuss et al., 2024; Bernal et al., 2024; Rizvi et al., 2021; Luo et al., 2023; Lorenzini et al., 2024), we speculate throughout the text that WMH may be upstream to neurodegeneration, recent neuropathological evidence suggests that WMH – especially in the parietal lobe - could result from tau-related axonal degeneration (McAleese et al., 2017). Future studies over a much longer timespan are needed to further understand this complex interplay, which will be crucial for refining models of AD progression (McAleese et al., 2017).

5. Conclusions

Pathological cerebrovascular processes related to WMH are an important co-pathology in early AD that contributes to neuronal loss in AD-vulnerable temporal regions, resulting in significant additional neurodegeneration beyond that induced by amyloid and tau. Interventions aimed at improving cerebrovascular health might mitigate early neurodegeneration in AD, potentially slowing the development of cognitive symptoms.

CRediT authorship contribution statement

Riccardo Leone: Writing – review & editing, Writing – original draft, Methodology, Investigation, Formal analysis, Data curation, Conceptualization. **Xenia Kobeleva:** Writing – review & editing, Supervision, Methodology, Investigation, Formal analysis, Conceptualization.

Funding

No third-party funding was received for this work.

Declaration of Competing Interest

All authors declare no competing interests.

Acknowledgements

Data collection and sharing for this project was funded by the Alzheimer's Disease Neuroimaging Initiative (ADNI) (National Institutes of Health Grant U01 AG024904) and DOD ADNI (Department of Defense award number W81XWH-12-2-0012). ADNI is funded by the National Institute on Aging, the National Institute of Biomedical Imaging and Bioengineering, and through generous contributions from the following: AbbVie, Alzheimer's Association; Alzheimer's Drug Discovery Foundation; Araclon Biotech; BioClinica, Inc.; Biogen; Bristol-Myers Squibb Company; CereSpir, Inc.; Cogstate; Eisai Inc.; Elan Pharmaceuticals, Inc.; Eli Lilly and Company; EuroImmun; F. Hoffmann-La Roche Ltd and its affiliated company Genentech, Inc.; Fujirebio; GE Healthcare; IXICO

Ltd.; Janssen Alzheimer Immunotherapy Research & Development, LLC.; Johnson & Johnson Pharmaceutical Research & Development LLC.; Lumosity; Lundbeck; Merck & Co., Inc.; Meso Scale Diagnostics, LLC.; NeuroRx Research; Neurotrack Technologies; Novartis Pharmaceuticals Corporation; Pfizer Inc.; Piramal Imaging; Servier; Takeda Pharmaceutical Company; and Transition Therapeutics. The Canadian Institutes of Health Research is providing funds to support ADNI clinical sites in Canada. Private sector contributions are facilitated by the Foundation for the National Institutes of Health (www.fnih.org). The grantee organization is the Northern California Institute for Research and Education, and the study is coordinated by the Alzheimer's Therapeutic Research Institute at the University of Southern California. ADNI data are disseminated by the Laboratory for Neuro Imaging at the University of Southern California.

Appendix A. Supporting information

Supplementary data associated with this article can be found in the online version at doi:10.1016/j.neurobiolaging.2025.07.007.

Data and material availability

Data used in preparation of this article were obtained from the Alzheimer's Disease Neuroimaging Initiative (ADNI) database. Data access requests should be sent to http://adni.loni.usc.edu/data-samples/adni-data/. A complete description of ADNI and up-to-date information is available at http://adni.loni.usc.edu/. The investigators within the ADNI contributed to the design and implementation of ADNI and/or provided data but did not participate in analysis or writing of this report. Code to reproduce the findings of the manuscript is available on (https://github.com/computational-neurology/WMH_in_AD).

References

Armstrong, Nicola J., Mather, Karen A., Sargurupremraj, Muralidharan, Knol, Maria J., Malik, Rainer, Satizabal, Claudia L., Yanek, Lisa R., et al., 2020. Common genetic variation indicates separate causes for periventricular and deep white matter hyperintensities. Stroke 51 (7), 2111–2121. https://doi.org/10.1161/STROKEAHA.119.027544.

Avants, B.B., Epstein, C.L., Grossman, M., Gee, J.C., 2008. Symmetric diffeomorphic image registration with cross-correlation: evaluating automated labeling of elderly and neurodegenerative brain. Med. Image Anal. 12 (1), 26–41. https://doi.org/10.1016/j.media.2007.06.004.

Bachmann, Dario, Saake, Antje, Studer, Sandro, Buchmann, Andreas, Rauen, Katrin, Gruber, Esmeralda, Michels, Lars, et al., 2024. Hypertension and cerebral blood flow in the development of alzheimer's disease. Alzheimer's Dement. J. Alzheimer's Assoc. Sept. https://doi.org/10.1002/alz.14233.

Barisano, Giuseppe, Montagne, Axel, Kisler, Kassandra, Schneider, Julie A., Wardlaw, Joanna M., Zlokovic, Berislav V., 2022. Blood–brain barrier link to human cognitive impairment and alzheimer's disease. Nat. Cardiovasc. Res. 1 (2), 108–115. https://doi.org/10.1038/s44161-021-00014-4.

Bernal, Jose, Inga Menze, Renat Yakupov, Oliver Peters, Julian Hellmann-Regen, Silka Dawn Freiesleben, Josef Priller, et al., 2024. Longitudinal evidence for a mutually reinforcing relationship between white matter hyperintensities and cortical thickness in cognitively unimpaired older adults. Alzheimer's Res. Ther. 16 (1), 240. https://doi.org/10.1186/s13195-024-01606-5.

Chételat, Gaël, Villemagne, Victor L., Pike, Kerryn E., Jean-Claude, Baron, Bourgeat, Pierrick, Jones, Gareth, Faux, Noel G., et al., 2010. Larger temporal volume in elderly with high versus low beta-amyloid deposition. Brain A J. Neurol. 133 (11), 3349–3358. https://doi.org/10.1093/brain/awq187.

Chun, M.Y., Jang, H., Kim, S.J., Park, Y.H., Yun, J., Lockhart, S.N., et al., 2023. Emerging role of vascular burden in AT(N) classification in individuals with Alzheimer's and concomitant cerebrovascular burdens. J. Neurol. Neurosurg. Psychiatry 95 (1), 44–51. Dec 14.

Ciric, Rastko, William H, Thompson, Romy, Lorenz, Mathias, Goncalves, Eilidh, MacNicol, Christopher J, Markiewicz, Yaroslav O, Halchenko, 2022. TemplateFlow: FAIR-sharing of multi-scale, multi-species brain models. Cold Spring Harb. Lab. https://doi.org/10.1101/2021.02.10.430678.

Dadar, Mahsa, Ana Laura, Manera, Simon, Ducharme, D. Louis, Collins, 2022. White matter hyperintensities are associated with grey matter atrophy and cognitive decline in alzheimer's disease and frontotemporal dementia. Neurobiol. Aging 111 (March), 54–63. https://doi.org/10.1016/j.neurobiolaging.2021.11.007.

Dadar, Mahsa, Camicioli, Richard, Duchesne, Simon, Collins, D.Louis, Alzheimer's Disease Neuroimaging Initiative, 2020. The temporal relationships between white matter hyperintensities, neurodegeneration, amyloid beta, and cognition. Alzheimer's Dement. (Amst. Neth.) 12 (1), e12091. https://doi.org/10.1002/dad2.12091.

Dalby, Rikke B., Eskildsen, Simon F., Videbech, Poul, Frandsen, Jesper, Mouridsen, Kim, Sørensen, Leif, Jeppesen, Peter, Bek, Toke, Rosenberg, Raben, Østergaard, Leif, 2019. Oxygenation differs among white matter hyperintensities, intersected fiber tracts and unaffected white matter. Brain Commun. 1 (1), fcz033. https://doi.org/10.1093/braincomms/fcz033.

DeCarli, Charles, Fletcher, Evan, Ramey, Vincent, Harvey, Danielle, Jagust, William J., 2005. Anatomical mapping of white matter hyperintensities (WMH): exploring the relationships between periventricular WMH, deep WMH, and Total WMH burden. Stroke 36 (1), 50–55. https://doi.org/10.1161/01.STR.0000150668.58689.f2.

Dickerson, B.C., Stoub, T.R., Shah, R.C., Sperling, R.A., Killiany, R.J., Albert, M.S., Hyman, B.T., Blacker, D., deToledo-Morrell, L., 2011. Alzheimer-signature MRI biomarker predicts AD dementia in cognitively normal adults. Neurology 76 (16), 1395–1402. https://doi.org/10.1212/WNL.0b013e3182166e96.

Dickie, David Alexander, Sherif, Karama, Stuart J, Ritchie, Simon R, Cox, Eleni, Sakka, Natalie A, Royle, Benjamin S, Aribisala, et al., 2016. Progression of white matter disease and cortical thinning are not related in older community-dwelling subjects. Stroke 47 (2), 410–416. https://doi.org/10.1161/STROKEAHA.115.011229.

Eisenmenger, Laura B., Peret, Anthony, Famakin, Bolanle M., Spahic, Alma, Roberts, Grant S., Bockholt, Jeremy H., Johnson, Kevin M., Paulsen, Jane S., 2023. Vascular contributions to alzheimer's disease. Transl. Res. 254 (April), 41–53. https://doi.org/10.1016/j.trsl.2022.12.003.

Esteban, O., C. Markiewicz, R. Blair, R. Poldrack, and K. Gorgolewski. 2024. sMRIPrep: Structural MRI PREProcessing Workflows (0.16.0). https://doi.org/10.5281/zenodo.13376346.

Falcon, Carles, Montesinos, Paula, Václavů, Lena, Kassinopoulos, Michalis, Minguillon, Carolina, Fauria, Karine, Cascales-Lahoz, Diego, et al., 2024. Time-encoded ASL reveals lower cerebral blood flow in the early AD continuum. Alzheimer's Dement. 20 (8), 5183–5197. https://doi.org/10.1002/alz.14059.

Fischl, Bruce, 2012. FreeSurfer. NeuroImage 62 (2), 774–781. https://doi.org/10.1016/j.neuroimage.2012.01.021.

Freeze, Whitney M., Jacobs, Heidi I.L., Gronenschild, Ed.H., Jansen, Jacobus F.A., Burgmans, Saartje, Aalten, Pauline, Clerx, Lies, et al., 2016. White matter hyperintensities potentiate hippocampal volume reduction in non-demented older individuals with abnormal amyloid-β." Edited by Joel Ramirez. J. Alzheimer's Dis. 55 (1), 333–342. https://doi.org/10.3233/JAD-160474.

Garnier-Crussard, Antoine, Cotton, François, Krolak-Salmon, Pierre, Chételat, Gaël, 2023. White matter hyperintensities in alzheimer's disease: beyond vascular contribution. Alzheimer's Dement. 19 (8), 3738–3748. https://doi.org/10.1002/alz.13057.

Graff-Radford, Jonathan, Arenaza-Urquijo, Eider M., Knopman, David S., Schwarz, Christopher G., Brown, Robert D., Rabinstein, Alejandro A., Gunter, Jeffrey L., et al., 2019. White matter hyperintensities: relationship to amyloid and tau burden. Brain 142 (8), 2483–2491. https://doi.org/10.1093/brain/awz162.

Griffanti, Ludovica, Jenkinson, Mark, Suri, Sana, Enikő, Zsoldos, Mahmood, Abda, Filippini, Nicola, Sexton, Claire E., et al., 2018. Classification and characterization of periventricular and deep white matter hyperintensities on MRI: a study in older adults. NeuroImage Segm. Brain 170 (April), 174–181. https://doi.org/10.1016/j.neuroimage.2017.03.024.

Griffis, Joseph C., Metcalf, Nicholas V., Corbetta, Maurizio, Shulman, Gordon L., 2021. Lesion quantification toolkit: a MATLAB software tool for estimating grey matter damage and white matter disconnections in patients with focal brain lesions. NeuroImage Clin. 30, 102639. https://doi.org/10.1016/j.nicl.2021.102639.

Groemping, Ulrike, 2007. Relative importance for linear regression in r: the package relaimpo. J. Stat. Softw. 17, 1–27. https://doi.org/10.18637/jss.v017.i01.

Harrison, Theresa M., Richard, Du, Klencklen, Giuliana, Baker, Suzanne L., William J, Jagust, 2021. Distinct effects of beta-amyloid and tau on cortical thickness in cognitively healthy older adults. Alzheimer's Dement. 17 (7), 1085–1096. https://doi.org/10.1002/alz.12249.

Insel, Philip S., Mormino, Elizabeth C., Aisen, Paul S., Thompson, Wesley K., Donohue, Michael C., 2020. Neuroanatomical spread of amyloid β and tau in alzheimer's disease: implications for primary prevention. Brain Commun. 2 (1), fcaa007. https://doi.org/10.1093/braincomms/fcaa007.

Jack, Clifford R., Wiste, Heather J., Weigand, Stephen D., Knopman, David S., Mielke, Michelle M., Vemuri, Prashanthi, Lowe, Val, et al., 2015. Different definitions of neurodegeneration produce similar amyloid/neurodegeneration biomarker group findings. Brain A J. Neurol. 138 (Pt 12), 3747–3759. https://doi.org/10.1093/brain/awv283.

Jack, Clifford R., Wiste, Heather J., Weigand, Stephen D., Therneau, Terry M., Knopman, David S., Lowe, Val, Vemuri, Prashanthi, et al., 2017. Age-specific and sex-specific prevalence of cerebral β-amyloidosis, tauopathy, and neurodegeneration in cognitively unimpaired individuals aged 50–95 years: a cross-sectional study. Lancet Neurol. 16 (6), 435–444. https://doi.org/10.1016/S1474-4422(17)30077-7.

Jack Jr, Clifford R., Andrews, J.Scott, Beach, Thomas G., Buracchio, Teresa, Dunn, Billy, Graf, Ana, Hansson, Oskar, et al., 2024. Revised criteria for diagnosis and staging of alzheimer's disease: alzheimer's association workgroup. Alzheimer's Dement. 20 (8), 5143–5169. https://doi.org/10.1002/alz.13859.

Kampmann, Martin, 2024. Molecular and cellular mechanisms of selective vulnerability in neurodegenerative diseases. Nat. Rev. Neurosci. 1–21. https://doi.org/10.1038/s41583-024-00806-0. https://doiorg/10.1038/s41583-024-00806-0.

Keuss, Sarah E., Coath, William, Cash, David M., Barnes, Josephine, Nicholas, Jennifer M., Lane, Christopher A., Thomas, Parker, D., et al., 2024. Rates of cortical thinning in alzheimer's disease signature regions associate with vascular burden but not with β-amyloid status in cognitively normal adults at age 70. J. Neurol. Neurosurg. Psychiatry 95 (8), 748–752. https://doi.org/10.1136/jnnp-2023-332067.

Keuss, Sarah E., Coath, William, Nicholas, Jennifer M., Poole, Teresa, Barnes, Josephine, Cash, David M., Lane, Christopher A., et al., 2022. Associations of β-amyloid and vascular burden with rates of neurodegeneration in cognitively normal members of the 1946 British Birth Cohort. Neurology 99 (2), e129–e141. https://doi.org/10.1212/WNL.0000000000200524.

Kisler, Kassandra, Nelson, Amy R., Montagne, Axel, Zlokovic, Berislav V., 2017. Cerebral blood flow regulation and neurovascular dysfunction in alzheimer disease. Nat. Rev. Neurosci. 18 (7), 419–434. https://doi.org/10.1038/nrn.2017.48.

Lambert, Christian, Benjamin, Philip, Zeestraten, Eva, Lawrence, Andrew J., Barrick, Thomas R., Markus, Hugh S., 2016. Longitudinal patterns of leukoaraiosis and brain atrophy in symptomatic small vessel disease. Brain 139 (4), 1136–1151. https://doi.org/10.1093/brain/aww009.

Landau, Susan M., Mintun, Mark A., Joshi, Abhinay D., Koeppe, Robert A., Petersen, Ronald C., Aisen, Paul S., Weiner, Michael W., Jagust, William J., Alzheimer's Disease Neuroimaging Initiative, 2012. Amyloid deposition, hypometabolism, and longitudinal cognitive decline. Ann. Neurol. 72 (4), 578–586. https://doi.org/10.1002/ana.23650.

Lee, Seonjoo, Viqar, Fawad, Zimmerman, Molly E., Narkhede, Atul, Tosto, Giuseppe, Benzinger, Tammie L.S., Marcus, Daniel S., et al., 2016. White matter hyperintensities are a core feature of alzheimer's disease: evidence from the dominantly inherited alzheimer network. Ann. Neurol. 79 (6), 929–939. https://doi.org/10.1002/ana.24647.

Li, Hao, Jacob, Mina A., Cai, Mengfei, Duering, Marco, Chamberland, Maxime, Norris, David G., Kessels, Roy P.C., Frank-Erik, de Leeuw, José P, Marques, Tuladhar, Anil M., 2023. Regional cortical thinning, demyelination and iron loss in cerebral small vessel disease. Brain A J. Neurol. 146 (11), 4659–4673. https://doi.org/10.1093/brain/awad220.

Li, Hongwei, Jiang, Gongfa, Zhang, Jianguo, Wang, Ruixuan, Wang, Zhaolei, Wei-Shi, Zheng, Menze, Bjoern, 2018. Fully convolutional network ensembles for white matter hyperintensities segmentation in MR images. NeuroImage 183 (December), 650–665. https://doi.org/10.1016/j.neuroimage.2018.07.005.

Lorenzini, Luigi, Maranzano, Alessio, Ingala, Silvia, Collij, Lyduine E., Tranfa, Mario, Blennow, Kaj, Di Perri, Carol, et al., 2024. Association of vascular risk factors and cerebrovascular pathology with alzheimer disease pathologic changes in individuals without dementia. Neurology 103 (7), e209801. https://doi.org/10.1212/WNL.0000000000209801.

Low, Audrey, Mak, Elijah, Rowe, James B., Markus, Hugh S., O'Brien, John T., 2019. Inflammation and cerebral small vessel disease: a systematic review. Ageing Res. Rev. 53 (August), 100916. https://doi.org/10.1016/j.arr.2019.100916.

Luo, Jingqin, Ma, Yinjiao, Folasade Jane, Agboola, Grant, Elizabeth, Morris, John C., McDade, Eric, Fagan, Anne M., et al., 2023. Longitudinal relationships of white matter hyperintensities and alzheimer disease biomarkers across the adult life span. Neurology 101 (2), e164–e177. https://doi.org/10.1212/WNL.0000000000207378.

Lyu, Xueying, Duong, Michael Tran, Xie, Long, Flores, Robin de, Richardson, Hayley, Hwang, Gyujoon, Wisse, Laura E.M., et al., 2024. Tau-neurodegeneration mismatch reveals vulnerability and resilience to comorbidities in alzheimer's continuum. Alzheimer's Dement. J. Alzheimer's Assoc. 20 (3), 1586–1600. https://doi.org/10.1002/alz.13559.

McAleese, Kirsty E., Walker, Lauren, Graham, Sophie, Moya, Elisa L.J., Johnson, Mary, Erskine, Daniel, Colloby, Sean J., et al., 2017. Parietal white matter lesions in Alzheimer's disease are associated with cortical neurodegenerative pathology, but not with small vessel disease. Acta Neuropathol. 134 (3), 459–473. https://doi.org/10.1007/s00401-017-1738-2.

Murray, Melissa E., Vemuri, Prashanthi, Preboske, Greg M., Murphy, Matthew C., Schweitzer, Katherine J., Parisi, Joseph E., Jack, Clifford R., Dickson, Dennis W., 2012. A quantitative postmortem MRI design sensitive to white matter hyperintensity differences and their relationship with underlying pathology. J. Neuropathol. Exp. Neurol. 71 (12), 1113–1122. https://doi.org/10.1097/NEN.0b013e318277387e.

Musiek, Erik S., Holtzman, David M., 2015. Three dimensions of the amyloid hypothesis: time, space, and 'wingmen.'. Nat. Neurosci. 18 (6), 800–806. https://doi.org/10.1038/nn.4018.

Oh, Hwamee, Habeck, Christian, Madison, Cindee, Jagust, William, 2014. Covarying alterations in Aβ deposition, glucose metabolism, and gray matter volume in cognitively normal elderly. Hum. Brain Mapp. 35 (1), 297–308. https://doi.org/10.1002/hbm.22173.

Parker, Thomas, D., Cash, David M., Lane, Christopher A., Lu, Kirsty, Malone, Ian B., Nicholas, Jennifer M., Sarah-Naomi, James, et al., 2020. Amyloid β influences the relationship between cortical thickness and vascular load. Alzheimer's Dement. Diagn. Assess. Dis. Monit. 12 (1), e12022. https://doi.org/10.1002/dad2.12022.

Patel, Yash, Shin, Jean, Sliz, Eeva, Tang, Ariana, Mishra, Aniket, Xia, Rui, Hofer, Edith, et al., 2024. Genetic risk factors underlying white matter hyperintensities and cortical atrophy. Nat. Commun. 15 (1), 9517. https://doi.org/10.1038/s41467-024-53689-1.

Reuter, Martin, Schmansky, Nicholas J., Rosas, H.Diana, Fischl, Bruce, 2012. Within-subject template estimation for unbiased longitudinal image analysis. NeuroImage 61 (4), 1402–1418. https://doi.org/10.1016/j.neuroimage.2012.02.084.

Rizvi, Batool, Lao, Patrick J., Chesebro, Anthony G., Dworkin, Jordan D., Amarante, Erica, Beato, Juliet M., Gutierrez, Jose, et al., 2021. Association of regional white matter hyperintensities with longitudinal alzheimer-like pattern of neurodegeneration in older adults. JAMA Netw. Open 4 (10), e2125166. https://doi.org/10.1001/jamanetworkopen.2021.25166.

Royse, Sarah K., Minhas, Davneet S., Lopresti, Brian J., Murphy, Alice, Ward, Tyler, Koeppe, Robert A., Bullich, Santiago, et al., 2021. Validation of amyloid PET positivity thresholds in centiloids: a multisite PET study approach. Alzheimer's Res. Ther. 13 (1), 99. https://doi.org/10.1186/s13195-021-00836-1.

Selkoe, Dennis J., Hardy, John, 2016. The Amyloid hypothesis of alzheimer's disease at 25 years. EMBO Mol. Med. 8 (6), 595–608. https://doi.org/10.15252/emmm.201606210.

Shirzadi, Zahra, Schultz, Stephanie A., Wai-Ying W, Yau, Joseph-Mathurin, Nelly, Fitzpatrick, Colleen D., Levin, Raina, Kantarci, Kejal, et al., 2023. Etiology of white matter hyperintensities in autosomal dominant and sporadic alzheimer disease. JAMA Neurol. 80 (12), 1353. https://doi.org/10.1001/jamaneurol.2023.3618.

Ter Telgte, Annemieke, Esther, M.C. Van Leijsen, Wiegertjes, Kim, Klijn, Catharina J.M., Tuladhar, Anil M., Frank-Erik, De. Leeuw, 2018. Cerebral small vessel disease: from a focal to a global perspective. Nat. Rev. Neurol. 14 (7), 387–398. https://doi.org/10.1038/s41582-018-0014-y.

Tuladhar, Anil M., Andrew, T.Reid, Shumskaya, Elena, de Laat, Karlijn F., van Norden, Anouk G.W., van Dijk, Ewoud J., Norris, David G., de Leeuw, Frank-Erik, 2015. Relationship between white matter hyperintensities, cortical thickness, and cognition. Stroke 46 (2), 425–432. https://doi.org/10.1161/STROKEAHA.114.007146.

Tustison, N.J., Avants, B.B., Cook, P.A., Zheng, Y., Egan, A., Yushkevich, P.A., Gee, J.C., 2010. N4itk: improved N3 bias correction. IEEE Trans. Med. Imaging 29 (6), 1310–1320. https://doi.org/10.1109/TMI.2010.2046908.

Tustison, N.J., Cook, Philip A., Holbrook, Andrew J., Johnson, Hans J., Muschelli, John, Devenyi, Gabriel A., Duda, Jeffrey T., et al., 2021. The ANTsX ecosystem for quantitative biological and medical imaging. Sci. Rep. 11 (1), 9068. https://doi.org/10.1038/s41598-021-87564-6.

Verdelho, Ana, Madureira, Sofia, José M, Ferro, Hansjörg, Baezner, Blahak, Christian, Poggesi, Anna, Hennerici, Michael, et al., 2012. Physical activity prevents progression for cognitive impairment and vascular dementia. Stroke 43 (12), 3331–3335. https://doi.org/10.1161/STROKEAHA.112.661793.

Wardlaw, Joanna M., Maria del C, Valdés Hernández, Susana Muñoz, Maniega, 2015. What are white matter hyperintensities made of? J. Am. Heart Assoc. 4 (6), 1–19. https://doi.org/10.1161/JAHA.114.001140.

Yeh, Fang-Cheng, Panesar, Sandip, Fernandes, David, Meola, Antonio, Yoshino, Masanori, Fernandez-Miranda, Juan C., Vettel, Jean M., Verstynen, Timothy, 2018. Population-averaged atlas of the macroscale human structural connectome and its network topology. NeuroImage 178 (September), 57–68. https://doi.org/10.1016/j.neuroimage.2018.05.027.

Zhang, Junfang, Chen, Haijuan, Wang, Jie, Huang, Qi, Xu, Xiaomeng, Wang, Wenjing, Xu, Wei, et al., 2024. Linking white matter hyperintensities to regional cortical thinning, amyloid deposition, and synaptic density loss in alzheimer's disease. Alzheimer's Dement. 20 (6), 3931–3942. https://doi.org/10.1002/alz.13845.

Zhang, C., Eleana, Sau May, Wong, Uiterwijk, Renske, Backes, Walter H., Jansen, Jacobus F.A., Cécile R. L. P. N, Jeukens, van Oostenbrugge, Robert J., Staals, Julie, 2019. Blood–brain barrier leakage in relation to white matter hyperintensity volume and cognition in small vessel disease and normal aging. Brain Imaging Behav. 13 (2), 389–395. https://doi.org/10.1007/s11682-018-9855-7.

3.3 Publication 3: Beyond Focal Lesions: Dynamical Network Effects of White Matter Hyperintensities

Human Brain Mapping

WILEY

RESEARCH ARTICLE OPEN ACCESS

Beyond Focal Lesions: Dynamical Network Effects of White Matter Hyperintensities

Riccardo Leone[1,2,3] | Steven Geysen[3,4] | Gustavo Deco[5,6] | Xenia Kobeleva[1,3,4] | Alzheimer's Disease Neuroimaging Initiative

[1]Computational Neurology Group, Ruhr University Bochum, Bochum, Germany | [2]Faculty of Medicine, University of Bonn, Bonn, Germany | [3]German Center for Neurodegenerative Diseases (DZNE), Bonn, Germany | [4]Department of Neurology, University Hospital Bonn, Bonn, Germany | [5]Department of Information and Communication Technologies, Center for Brain and Cognition, Computational Neuroscience Group, Universitat Pompeu Fabra, Barcelona, Spain | [6]Institució Catalana de la Recerca i Estudis Avançats (ICREA), Barcelona, Spain

Correspondence: Xenia Kobeleva (xkobeleva@gmail.com)

Received: 8 August 2024 | **Revised:** 3 November 2024 | **Accepted:** 11 November 2024

Funding: X.K. was supported by an add-on fellowship of the Joachim Herz Foundation, a grant of the Transdisciplinary Research Area 1 of the University of Bonn, the Innovative Minds Programme of the Stiftung Deutsche Demenzhilfe, and the BONFOR research group support by University Hospital of Bonn. G.D. was supported by the project NEurological MEchanismS of Injury, and Sleep-like cellular dynamics (NEMESIS) (ref. 101071900) funded by the EU ERC Synergy Horizon Europe; the NODYN Project PID2022-136216NB-I00 financed by the MCIN/AEI, UE, the Ministry of Science and Innovation, the State Research Agency and the European Regional Development Fund; the AGAUR research support grant (ref. 2021 SGR 00917) funded by the Department of Research and Universities of the Generalitat of Catalunya, and the project eBRAIN-Health—Actionable Multilevel Health Data (id 101058516), funded by the EU Horizon Europe.

Keywords: connectivity | dementia | disconnectome | fMRI | neural-mass modeling | white matter hyperintensities | whole-brain modeling

ABSTRACT

White matter (WM) tracts shape the brain's dynamical activity and their damage (e.g., white matter hyperintensities, WMH) yields relevant functional alterations, ultimately leading to cognitive symptoms. The mechanisms linking the structural damage caused by WMH to the arising alterations of brain dynamics is currently unknown. To estimate the impact of WMH on brain dynamics, we combine neural-mass whole-brain modeling with a virtual-lesioning (disconnectome) approach informed by empirical data. We account for the heterogeneous effects of WMH either on inter-regional communication (i.e., edges) or on dynamics (i.e., nodes) and create models of their local versus global, and edge versus nodal effects using a large fMRI dataset comprising 188 non-demented individuals (120 cognitively normal, 68 with mild cognitive impairment) with varying degrees of WMH. We show that, although WMH mainly determine local damage to specific WM tracts, these lesions yield relevant global dynamical effects by reducing the overall synchronization of the brain through a reduction of global coupling. Alterations of local nodal dynamics through disconnections are less relevant and present only at later stages of WMH damage. Exploratory analyses suggest that education might play a beneficial role in counteracting the reduction in global coupling associated with WMH. This study provides generative models linking the structural damage caused by WMH to alterations in brain dynamics. These models might be used to evaluate the detrimental effects of WMH on brain dynamics in a subject-specific manner. Furthermore, it validates the use of whole-brain modeling for hypothesis-testing of structure–function relationships in diseased states characterized by empirical disconnections.

1 | Introduction

The structural scaffold formed by white matter connections shapes cerebral dynamical activity (Sporns 2013; Suárez et al. 2020). Its damage results in disruption of the arising dynamics (Alstott et al. 2009; Cabral et al. 2012; Idesis et al. 2022; Thiebaut de Schotten, Foulon, and Nachev 2020), ultimately yielding cognitive deficits (Jenkins et al. 2021; Thiebaut de Schotten, Foulon, and Nachev 2020). White matter hyperintensities (WMH) constitute imaging correlates of white matter

Summary

- White matter hyperintensities (WMH) appear in imaging studies as damage to focal white matter tracts, but they induce dynamical effects on interregional communication at a global level.
- In later stages of white matter damage, WMH might also determine changes in intrinsic regional brain node dynamics through disconnections.
- Whole-brain modeling can be used to effectively link structural damage to associated alterations of brain dynamics.

damage and are characterized by local areas of high signal in T2-weighted MRI (Kantarovich et al. 2022; Wardlaw, Valdés Hernández, and Maniega 2015). They pathologically correspond to vasculopathy, chronic demyelination, axonal damage and loss (Wardlaw, Valdés Hernández, and Maniega 2015). Previous studies demonstrated that WMH is associated with alterations of brain dynamics with significant effects both on static functional connectivity (FC) and time-varying FC (tv-FC) (Jenkins et al. 2021; Kantarovich et al. 2022; Schlemm et al. 2022; Schulz et al. 2021). Nonetheless, these studies lacked a generative model allowing them to explain these modifications and to compare different pathophysiological hypotheses. Understanding the effects of WMH is of crucial clinical importance due to their high prevalence and associated risk of developing cognitive impairment (Debette and Markus 2010; Wardlaw, Valdés Hernández, and Maniega 2015). Better elucidation of the pathophysiological effects of WMH on brain dynamics might provide insights for the development of new preventive and treatment strategies aimed at counteracting their detrimental effects. Furthermore, generative models of brain signal alterations caused by WMH might prove useful to predict subject-specific network dynamics alterations stemming from WM lesions in a clinical setting.

By linking structural connectivity to the arising dynamics through well-defined mathematical equations, whole-brain neural mass models (WBM) are well suited to explore the dynamical effects of structural lesions, such as WMH (Alstott et al. 2009; Cabral et al. 2012; Deco et al. 2017; Idesis et al. 2022). In WBM, model parameters can be adjusted based on hypotheses about the pathophysiological effects of the investigated observables (e.g., lesions of white matter tracts) and the biological plausibility of these hypotheses can be tested in terms of goodness of fit between simulated and empirical fMRI or EEG data (Kobeleva et al. 2022). From a network perspective, by interrupting the communication between various brain regions, WMH can be conceptualized as disconnections (Griffis et al. 2021; Idesis et al. 2022; Thiebaut de Schotten, Foulon, and Nachev 2020). As shown by a previous computational study, disconnections unlink each regional activity from that of other network's nodes, thus affecting the resulting FC (Cabral et al. 2012). Although promising, previous theoretical studies evaluating the impact of disconnections lacked validation by empirical data analyses, thus limiting the clinical applicability of whole-brain mass models for diagnostic or prognostic purposes.

In this study, by combining WBM with a virtual-lesioning disconnectome approach—informed by empirical WMH lesions—we aim to contribute to a deeper understanding of the effect of structural alterations caused by WMH on resting-state brain dynamics, going beyond focal lesion studies such as in stroke (Idesis et al. 2022). We introduce the concept that WMH might result in changes in the intrinsic dynamics of disconnected regions and build upon previous theoretical results (Cabral et al. 2012) by testing theoretical predictions against empirical data. Specifically, we aim to: (a) test how WMH influence inter-regional connectivity (structural disconnectivity models) and neuronal activity at the node level (node disconnectivity models), and (b) determine whether WMH effects are localized (i.e., focal) or indicative of more diffuse white matter damage (i.e., global). To achieve this, we developed four distinct WMH-weighted models to explore these hypotheses and compared them to a baseline benchmark model with no information regarding WMH. Our modeling approach is based on resting-state fMRI data of 188 elderly nondemented study participants (either cognitively normal or with mild cognitive impairment), constituting one of the largest data-driven WBM studies to date.

2 | Materials and Methods

2.1 | Participants

From an initial sample of 363 elderly subjects without dementia from the Alzheimer's Disease NeuroImaging Initiative 3 dataset, 188 subjects with available rs-fMRI, 3D-T1-weighted and 3D-FLAIR sequences, acquired at 3T at the same timepoint, were included after preprocessing. CSF biomarkers, including the amyloid-beta peptide 42 to 40 ratio (Aβ42/Aβ40) and total tau levels, were obtained from the UPENNBIOMK Master data release (Shaw et al. 2009). The detailed step-by-step inclusion and exclusion flowchart is summarized in Figure S1. In exploratory analyses, we assessed the associations between model-derived parameters of the homogeneous SDC model (i.e., the model with the best fit) and executive functions and memory. We used the composite measurements of executive functions and memory provided in the ADNI database. The full details are in Gibbons et al. (2012).

2.2 | MRI Preprocessing and Timeseries Extraction

The full MRI acquisition and preprocessing protocol is provided in the Supporting Information. Briefly, fMRIPrep v. 21.0.4 (Esteban et al. 2019) was used for fMRI preprocessing. XCP-D (Adebimpe et al. 2023) was used to discard the first four timepoints, to perform the "nonaggressive" ICA-AROMA denoising strategy (including six motion estimates and their derivatives as well as signal from white matter and CSF), and to extract regional timeseries for the 90 supratentorial regions of the automated anatomical labeling (AAL) atlas (Tzourio-Mazoyer et al. 2002) (Figure 1A and Table S1). Timeseries were demeaned, detrended and filtered in the 0.04–0.07 Hz frequency range.

2.3 | Structural Connectivity

To avoid the possible detrimental effects of WMH on diffusion tractography (Min et al. 2021; Svärd et al. 2017), we used a

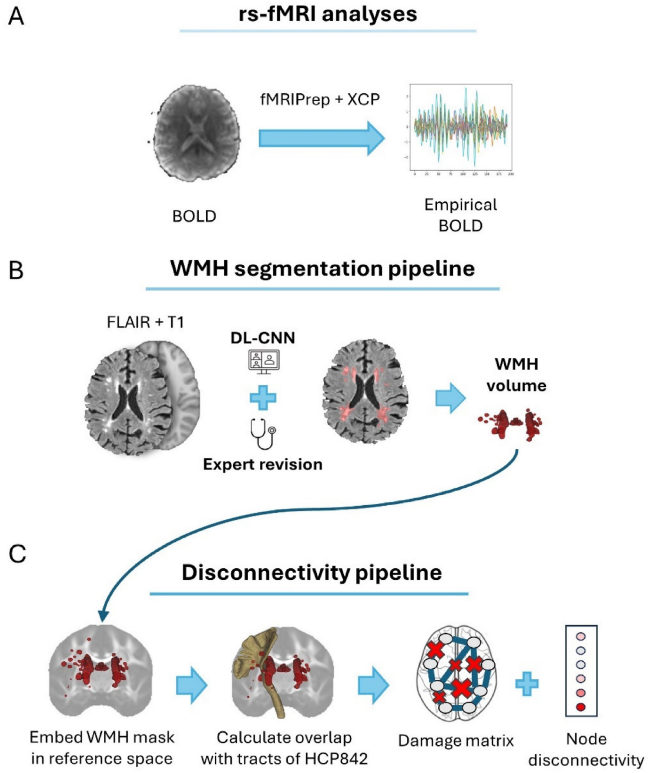

FIGURE 1 | Preprocessing workflow of the study. (A) fMRI data preprocessing was performed using the reproducible containerized versions of fMRIPrep (Esteban et al. 2019) and XCP (Adebimpe et al. 2023). (B) WMH segmentation was performed in subject space via automated deep learning software and visually checked to avoid inconsistencies. Infratentorial WMH were removed. (C) MNI-registered WMH masks were used as input for the Lesion Quantification Toolkit to calculate subject-specific damage matrices, representing the percentage of damage to each regional connection (represented by an "X" of different dimensions on the damaged tract) and a node disconnection vector, summarizing, for each brain region, the extent of regional disconnection from the whole-brain network (represented by different shades of red; gray defines nodes that were not disconnected by WMH).

normative SC matrix based on the AAL atlas from a previously published study in healthy controls (Škoch et al. 2022).

2.4 | WMH Segmentation and Disconnectome Analysis

Segmentation of WMHs was performed using a deep-learning-based software (Li et al. 2018) in subject space (Figure 1B). Segmentations were visually inspected to avoid inconsistencies and manually modified, if needed. Infratentorial WMH were removed. Fazekas score (Fazekas et al. 1987) was recorded. Total WMH volumes were calculated in mm^3, log-transformed and normalized to the 0–1 range (only in the group with relevant WMH, namely the volume for subjects without relevant WMH was set to 0). WMH segmentations were registered to MNI space and used as inputs for the Lesion Quantification Toolkit (LQT) (Griffis et al. 2021). The full details are reported in the original paper (Griffis et al. 2021) and graphically summarized in Figure 1C. Briefly, LQT employs a normative white matter atlas in MNI space to estimate the damage to each of 70 reference tracts caused by the input lesion. From this, a disconnection vector ($\vec{d}$) representing the WMH-related disconnection to each region and a damage matrix (DM) representing the percentage of damage to each edge are calculated.

2.5 | Hopf Model

We modelled each regional BOLD signal over time using the normal form of a supercritical Hopf bifurcation and coupled the resulting activity through the normative AAL atlas (Škoch et al. 2022; Figure 2A). The Hopf model has been widely used to describe whole-brain neural dynamics, given its ability to capture static and dynamic properties of brain functional connectivity (Deco et al. 2017). In the complex plane, the simulated BOLD activity (z) of each node (n) over time (t) is described by the following differential equation:

$$\frac{dz_n}{dt} = z\left[a_n + i\omega_n - \left|z_n^2\right|\right] + \beta\eta_n(t) \quad (1)$$

where z_n is a complex number $z_n = x_n + i\,y_n$, ω_n denotes the intrinsic frequency of each node, which is determined empirically by averaging the peak frequencies of narrowband-filtered BOLD signals in the 0.04–0.07 Hz range. We used group-averaged frequencies for all simulations. $\eta_n(t)$ represents additive Gaussian noise with standard deviation β. Substituting z_n in Equation (1) and dividing into the real and imaginary parts of the equation, we obtain:

$$\frac{dx_n}{dt} = \left[a_n - x_n^2 - y_n^2\right]x_n - \omega_n y_n + \beta\eta_n(t) \quad (2)$$

$$\frac{dy_n}{dt} = \left[a_n - x_n^2 - y_n^2\right]y_n - \omega_n x_n + \beta\eta_n(t) \quad (3)$$

Here, x_n represents the BOLD signal for a single uncoupled node. In the Hopf model, a_n, is known as the bifurcation parameter, and can be thought of as a control parameter governing the dynamical activity of each region. When the bifurcation parameter is negative ($a_n < 0$), the addition of Gaussian noise results in noisy activity around a stable point, which can be thought of as corresponding to asynchronous neuronal firing. After transitioning to values greater than the bifurcation point ($a = 0$), full oscillations are observed for positive values ($a_n > 0$), which correspond to synchronized neuronal firing.

Given that the brain is a coupled system consisting of various nodes (brain regions), the activity of all nodes is coupled through an underlying structural connectivity matrix C_{np}, which is defined as the number of streamlines connecting each two regions n and p. The real part of the complex number z_n representing the BOLD signal for node n when considering the coupled whole-brain system is then described by the following equation:

$$\frac{dx_n}{dt} = \left[a_n - x_n^2 - y_n^2\right]x_n - \omega_n y_n + G\sum_i C_{np}\left(x_p - x_n\right) + \beta\eta_n(t) \quad (4)$$

where G, defined as the global coupling weight, equally scales the total input received by each brain area to determine the overall synchronization. In the baseline model, we set the bifurcation parameter for all nodes at the brink of the bifurcation ($a_n = -0.02$),

as this nodal activity regime is able to give rise to complex collective brain dynamics resembling whole-brain activity observed in vivo (Deco, Jirsa, and McIntosh 2011; Deco et al. 2017). All simulations were implemented in Neurolib (Cakan, Jajcay, and Obermayer 2021). The sampling rate of 3 s and simulation length matched the empirical preprocessed fMRI recordings, plus two initial minutes—to allow for the stabilization of the system after the initial random conditions—that were discarded before other analyses.

2.6 | Model Fitting

As commonly performed in the literature (Deco et al. 2019; Patow et al. 2023), we initially aimed to best characterize both time-averaged and time-varying properties of the empirical data by calculating FC and tv-FC (Deco et al. 2019) in healthy subjects without WMH. In line with previous studies (Deco et al. 2019; Patow et al. 2023), fitting tv-FC was clearly a stronger model constraint compared with fitting FC in our dataset. As can be seen in Figure S2, FC fits are consistently high across a wide range of G (resulting in several possible G values to retrieve the same FC), while tv-FC clearly shows a global minimum at $G = 1.98$. This is an expected finding, as tv-FC is better able to capture the complex spatiotemporal structure inherent in fMRI data. Due to better constraints in model parameter estimation, we only focus on fitting tv-FC for further analyses.

Tv-FC was assessed using the phase functional connectivity dynamics (phFCD) (Deco et al. 2019). Briefly, for both empirical and

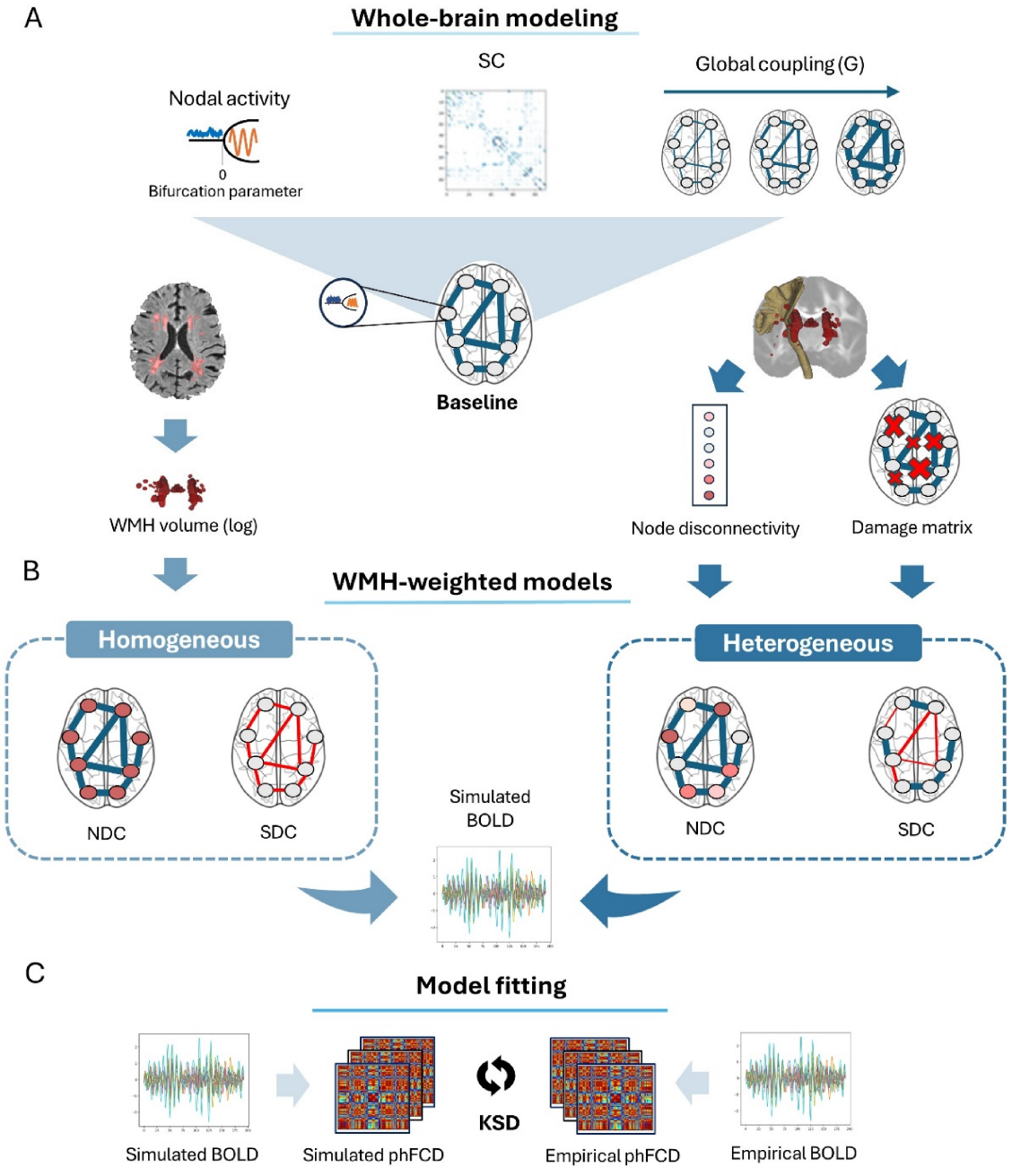

FIGURE 2 | Legend on next page.

simulated signals, we first applied the Hilbert transform to calculate the instantaneous BOLD phase of each region n at each timepoint t. For each timepoint, we then calculated its phase coherence matrix by taking the cosine of the absolute phase difference of each two regions n and m. When the BOLD signal in regions n and m is synchronized, it means that their phases would be similar, and, consequently, their phase difference is small, resulting in a high phase coherence value (close to 1). On the other hand, if their phases are not aligned (i.e., asynchronous), their phase coherence value is close to zero. Since the phase coherence matrix is symmetric, we only considered its upper triangular part and we accrued them over all timepoints for each subject or simulation. We finally compared the empirical and simulated distributions of the phFCD using the Kolmogorov–Smirnov distance (KSD). Lower KSD represents better goodness of fit (Figure 2C). The full details are in Deco et al. (2019).

2.7 | Modeling Steps

We hypothesized that WMH might have an impact on brain dynamics only after a certain threshold, so we used the clinical Fazekas score (Fazekas et al. 1987)—a visual estimate of the amount of WMH in structural MRI scans (score range 0–3)—to binarize our sample into a group without relevant WMH (Fazekas ≤ 1) and a group with relevant WMH (Fazekas >1). Previous studies using the Hopf model showed that brain dynamics in healthy subjects are best described by slightly subcritical bifurcation parameters (Deco et al. 2017). We assessed the optimal dynamical working point in our sample by performing a group-level tuning of the Hopf whole-brain model in the healthy subjects' group (no WMH and cognitively unimpaired). To do so, we fixed a (uniformly across regions) just below the critical bifurcation point ($a=-0.02$) and allowed G to vary as a free parameter (Figure 2B) ($0 \leq G \leq 3.5$, $\Delta G = 0.02$). The best G maximizing the fit to empirical data was found at 1.98. We refer to the resulting model (with $a=-0.02$ and $G=1.98$) as the baseline model and use it as a reference benchmark for comparison of all WMH-weighted models.

2.8 | WMH-Weighted Models

We first discuss the building blocks of WBM aimed at evaluating the effects of WMH on brain dynamics, tested in the subgroups with relevant WMH (88 subjects), and later presented the specific equations used for fitting. We developed four distinct WMH-weighted models (Figure 2B) guided by two sets of interrelated hypotheses: (Sporns 2013) how WMH might influence various parameters of the whole-brain model (i.e., edges vs. nodes), and (Suárez et al. 2020) the biological nature of WMH (i.e., local vs. global).

The first set of hypotheses explored how WMH might impact brain dynamics. Since WMH damage WM tracts, which are crucial for communication between brain regions, we posited that WMH could reduce the strength of inter-regional communication (i.e., the edges of the connectome), leading to structural disconnectivity (SDC) models. Additionally, experimental data suggest that axonal lesions could alter the intrinsic dynamic of neuronal firing (Nagendran et al. 2017). In the node disconnectivity (NDC) models, we tested whether these changes could be seen in the whole-brain Hopf models as variations in (nodal) bifurcation parameters. Based on previous studies (Demirtaş et al. 2017; Sanz Perl et al. 2023), we hypothesized that higher WMH-related disconnections might induce reductions in bifurcation parameters.

The second set of hypotheses addressed whether WMH effects are location-specific (i.e., local) or suggestive of a more diffuse WM damage (i.e., global). Biological evidence posits that WMH might represent just the observable aspect of a more widespread WM damage that is not visible with conventional MRI (Maillard et al. 2011; ter Telgte et al. 2018). We explored this concept by developing homogeneous models, which hypothesized that WMH effects are global and confronted them with heterogeneous models where the effects of WMH are locally confined to the specific brain regions or connections damaged by visible WMH.

To build the heterogeneous models, we used outputs from the LQT pipeline. For the heterogeneous SDC model, we linearly

FIGURE 2 | Schematics of the modeling pipeline. (A) In a whole-brain Hopf model, each regional dynamics over time is driven by its intrinsic frequency (not shown, as this was estimated from the empirical data and not modified in relation to WMH) and by a bifurcation parameter, describing the transition from asynchronous noisy behavior (<0) to full oscillations (>0), with zero referred to as the critical bifurcation point. The overall activity of the network is derived from the sum of the local activity plus the weighted (by the strength of inter-regional connection, e.g., number of tracts) sum of the activities of all regions connected to it, scaled by a global coupling parameter (G). Using this framework, a baseline model was constructed based on a normative SC and tuned to the empirical data of subjects without cognitive impairment and without WMH (Baseline model). (B) This panel displays the four WMH-weighted whole-brain models, categorized into homogeneous and heterogeneous types according to the hypotheses outlined in the main text. These models investigate whether WMH effects are localized to specific brain regions (heterogeneous) or distributed broadly across the brain (homogeneous). For the homogeneous models, the log-transformed volume of WMH is applied to uniformly reduce either connectivity or bifurcation parameters uniformly across the brain. In the homogeneous Node Disconnectivity (NDC) model, the bifurcation parameters in all regions are uniformly decreased, represented by red nodes with the same shade. In the homogeneous structural disconnectivity (SDC) model, connectivity across all tracts is uniformly reduced, shown as uniformly thinner red lines. In the heterogeneous models, the NDC model links WMH to changes in bifurcation parameters, using the node disconnectivity vector to inform how these parameters are altered in specific regions, depicted as red nodes of varying shades. Meanwhile, the SDC version simulates how WMH reduce inter-regional communication along specific tracts. This is achieved by using the damage matrix from the Lesion Quantification Toolkit to decrease connectivity only in those specific tracts, illustrated with red lines of varying thickness. The brain network illustration also includes gray nodes, which represent regions where WMH do not impact bifurcation parameters (matching the baseline model), and blue tracts, indicating connections not affected by WMH. These models were employed to simulate whole-brain BOLD activity and were subsequently compared against empirical data and a baseline model without WMH information. (C) The dynamics of phase coherence matrices (phFCD) was chosen as the fitting measurement between simulated and empirical data and compared with the Kolmogorov–Smirnov distance (KSD, see Methods for a full description). Lower values of KSD represent a better fit.

reduced the edge values of the normative SC matrix by the subject-specific damage matrix. For the heterogeneous NDC model, we reduced the bifurcation parameters proportionally to the node disconnectivity vector. For the homogeneous models, we used the log-transformed WMH volume as a proxy of overall brain damage. The homogeneous SDC model was created by proportionally reducing the global coupling parameter, while the homogeneous NDC model involved proportionally decreasing all bifurcation parameters with increasing WMH volume.

To introduce information regarding WMH in the Hopf model we performed a linear fitting of one of its parameters (a, G, or SC) by WMH information (WMH volume log-transformed, node disconnectivity or damage matrix) and explored the parameter space using a grid search. More in detail, the NDC and SDC homogeneous models were obtained by fitting a or G, respectively, as follows:

$$a = -0.02 + w * \mathrm{WMH}_{\mathrm{vol}} + b\ (-0.1 \le \mathrm{w} \le 0,\ -0.05 \le \mathrm{b} \le 0,\ \Delta\mathrm{w} = \Delta\mathrm{b} = 0.005);$$

$$G = 1.98 + w * \mathrm{WMH}_{\mathrm{vol}} + b\ (-1 \le \mathrm{w} \le 0,\ \Delta\mathrm{w} = 0.1;\ -0.5 \le \mathrm{b} \le 0,\ \Delta\mathrm{b} = 0.05);$$

The heterogeneous SDC model was obtained by linearly reducing the weights of the SC based on the damage matrix calculated by LQT, as follows:

$$\mathrm{SC}_{\mathrm{het}} = \mathrm{SC} + w * \mathrm{DM}\ (-0.25 \le w \le 0,\ \mathrm{b} = 0,\ \Delta\mathrm{w} = 0.005)$$

Elements with values less than zero in the resulting matrix were reset to zero. This matrix was used instead than the healthy normative SC. The fitting of b was omitted considering that the average value of SC elements is approximately zero.

Finally, the heterogeneous NDC model used the region disconnection vector $\vec{d}$ as a spatial prior for linear fitting, leading to heterogeneous bifurcation parameters (different between regions):

$$\vec{a} = -0.02 + w * \vec{d} + b\ (-0.1 \le \mathrm{w} \le 0,\ -0.05 \le b \le 0,\quad \Delta w = \Delta b = 0.005).$$

Homogeneous random models were obtained by randomly shuffling WMH volume across subjects. The heterogeneous random versions were obtained by randomly shuffling the region disconnection vector or damage matrix between subjects for node and structural disconnectivity models, respectively.

2.9 | Statistical Comparisons

Categorical variables are reported as numbers (percentages) and continuous variables as median (interquartile ranges) and compared with the Chi-square and Mann–Whitney-U test, respectively. Models' goodness of fit was compared with the paired-samples Wilcoxon test and corrected for multiple comparisons with the Benjamini–Hochberg method (Benjamini and Hochberg 1995). Partial correlation analyses were performed using Spearman's correlation and corrected for age.

3 | Results

3.1 | Empirical Data Analysis

We first present the overall characteristics of the sample (Table S2 and Figure S3). We hypothesized that WMH might not have an impact on brain dynamics in the lowest Fazekas score group due to their very limited extension, thus we binarized our sample into a group without relevant WMH (Fazekas ≤ 1, 100 subjects) and a group with relevant WMH (Fazekas > 1, 88 subjects). We also later explored the effects of WMH on brain dynamics in the subgroup with the highest Fazekas score of 3 ("High WMH", 22 subjects). As expected, subjects with relevant WMH were significantly older than those without ($p < 0.001$). There were no statistically significant differences in years of education and mini-mental state examination (MMSE) between the two groups. WMH did not show any significant correlation with Aβ42/Aβ40 nor tau CSF levels (all $p > 0.05$; Figure S4). Figure 3A shows the regional distribution of WMH (Figure 3A); compared to the group without WMH, the group-averaged distribution of the phFCD was shifted towards lower values in individuals with WMH ($p < 0.001$), suggesting lower synchrony (Figure 3B).

3.2 | Model Comparison

Accounting for WMH-related damage resulted in better descriptions (lower KSD) of the empirical data compared to the baseline model (Figure 3C, for individual p values, please see Table 1). We found that WMH significantly alter inter-regional communication strengths (i.e., edges), although this effect remained statistically significant after correcting for multiple comparisons only for the homogeneous SDC model. We compared these models fits to the respective randomly implemented counterparts and found that random models resulted in significantly lower model fits for both SDC models (Figure S5, Table S3). Interestingly, both heterogeneous models did not result in increased model fit compared to their homogeneous counterparts. The volume of WMH (log-transformed) was significantly positively correlated with the percent improvement of model fit compared with baseline for all WMH-weighted models (Figure 3D). These analyses were performed considering partial correlation corrected for the effects of age (Table 2). Based on these findings, we assessed the dynamical effects of WMH in the group with the highest WMH (Fazekas score of 3). Here, the heterogeneous SDC and both NDC models described the empirical data significantly better compared to the baseline, also after multiple comparisons correction (Figure 3E), suggesting that at higher level of tract damage, an effect on regional node dynamics is also observed (Table 2).

3.3 | Assessing the Impact of Clinical Variables on Model Fit

We then performed exploratory correlational analyses (partial correlations, including the effects of age) to further evaluate if other clinical variables might be responsible for the increase in model fit compared to the baseline (Figure 4, Table 2). We

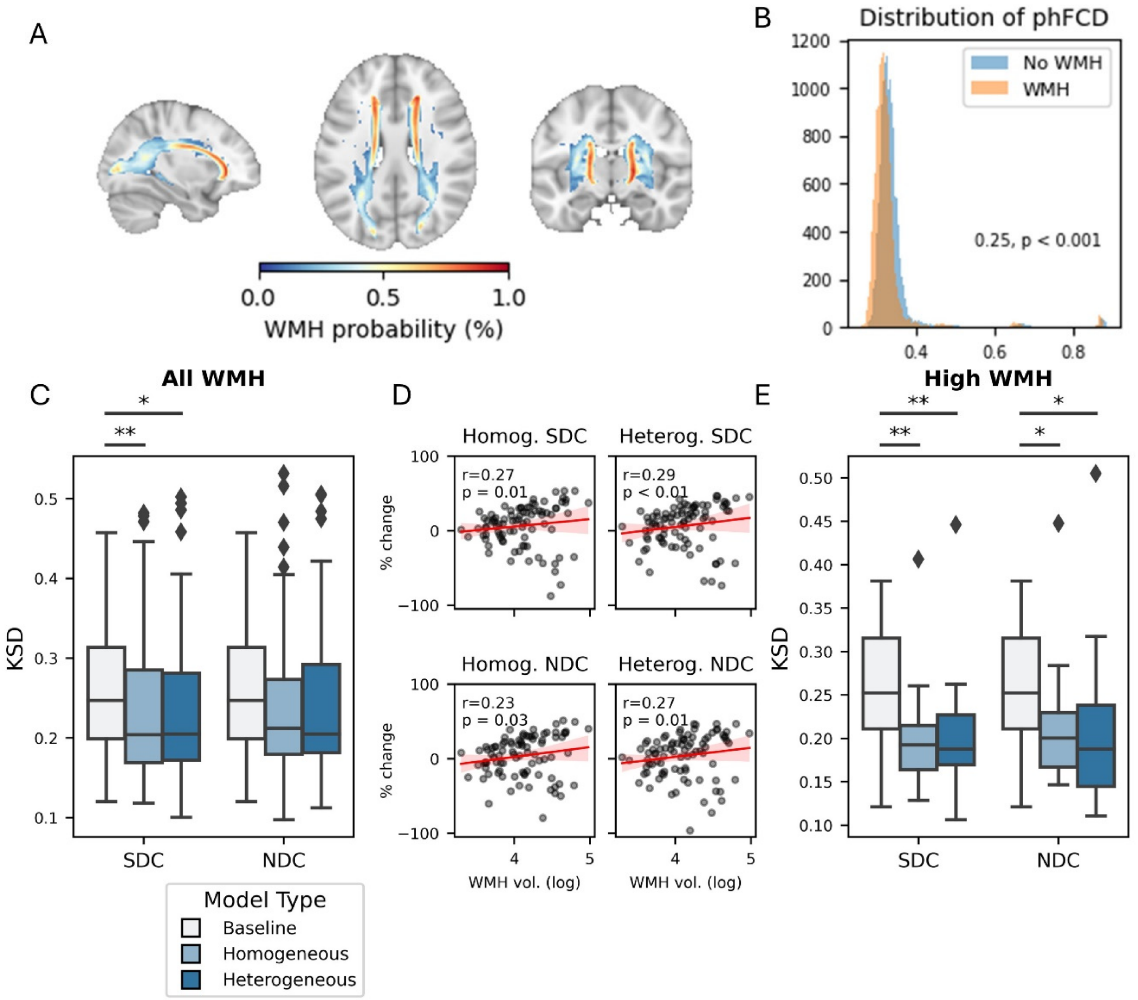

FIGURE 3 | (A) Maximum intensity projections along the sagittal (left), axial (middle) and coronal (right) planes of WMH probability maps. (B) Histograms of the distribution of the group-averaged phase functional connectivity dynamics (phFCD) in the groups without (blue) and with (orange) relevant WMH. The distribution of the phFCD is significantly shifted towards lower phFCD values in the group with relevant WMH, suggesting lower synchrony ($p < 0.001$). (C) Boxplots summarizing model comparisons between the baseline (white) and the homogeneous (light blue) and heterogeneous models (dark blue). The same baseline model (in white) is shown twice for better visualization of the comparison. Structural disconnectivity models (SDC), assessing the impact of WMH on structural connections are grouped on the left. Node disconnectivity (NDC) models, showing the effects of WMH on bifurcation parameters are shown as grouped boxplots on the right. The boxplots represent the Kolmogorov–Smirnov distance (KSD) between the empirical and simulated phase functional connectivity dynamics for the whole group with WMH. Note that after Benjamini–Hochberg correction only the homogeneous SDC remained statistically significant. (D) Scatterplots depicting the correlation between WMH volume (log-transformed, along the x axes) and the percentage of improvement in the model fit of the considered model (homogenous/heterogeneous SDC/NDC) compared to the baseline model (r refers to post hoc Spearman's rank-order partial correlation corrected for age, $p = p$-value). (E) The same model comparison as in (C) was evaluated in the group with the highest Fazekas score of 3. All comparisons remained statistically significant also after Benjamini–Hochberg correction. *$0.01 < p < 0.05$; **$0.001 < p <= 0.01$.

found that for both SDC models, the increase in performance was negatively correlated with years of patient education. For the heterogeneous SDC model, the observed improvement was also positively correlated with increasing age. No correlations were found between these variables and either of the NDC models (Figure S5, Table 2).

3.4 | Assessing the Association Between Model Parameters and Cognitive Scores

We performed exploratory analyses to investigate the association of model-derived parameters on cognitive scores of executive functions and memory. We focused on the homogeneous SDC model since this was the best-performing model. We did not find any statistically significant association between executive functions and memory scores (Figure S6).

4 | Discussion

In this study, we aimed to quantify in vivo global dynamical effects induced by WMH, which are highly prevalent lesions of the WM in the general aging population (Garnier-Crussard et al. 2023; Wardlaw, Valdés Hernández, and Maniega 2015). We combined WBM (Alstott et al. 2009; Cabral et al. 2012;

Deco et al. 2017; Demirtaş et al. 2017; Idesis et al. 2022; Patow et al. 2023; Sanz Perl et al. 2023) with a virtual-lesioning approach (Griffis et al. 2021) and tested different hypothesis-driven generative models of brain dynamics against empirical resting-state fMRI data, providing new insights into the pathophysiology of WMH from a network perspective. We tested various hypotheses on the local versus global and nodal versus edge effects of WMH in different WMH-weighted models and compared them both to a baseline model, to evaluate their added accuracy in describing empirical data, and to random models, to assess their robustness. We found that, although WMH are focal lesions of WM tracts, they induce global effects on network dynamics by reducing the global coupling of the network. At later stages of damage (e.g., higher WMH volume), WMH also alter the intrinsic nodal dynamics of disconnected regions. Finally, exploratory analyses suggested that level of education plays a role in counteracting the detrimental effects of WMH on global coupling, consistent with previous work on cognitive reserve (Stern 2009). Our results contribute to building biologically plausible and clinically informative models of brain dynamics in the healthy aging population and in diseases characterized by an elevated volume of WMH, such as cerebrovascular and Alzheimer's dementia (Garnier-Crussard et al. 2023; Wardlaw, Valdés Hernández, and Maniega 2015). Furthermore, methods and insights from this study might also be applied to other neurological diseases characterized by WM disconnections, that is, multiple sclerosis or traumatic brain injury.

TABLE 1 | Median (interquartile range) Kolmogorov–Smirnov distance (KSD) of the simulated phase functional connectivity dynamics compared to the empirical data for the baseline and WMH-weighted models.

	All WMH		High WMH	
Model Name	**KSD**	***p***	**KSD**	***p***
Baseline	0.25 (0.20–0.31)	NA	0.25 (0.21–0.31)	NA
Homogeneous SDC	0.20 (0.17–0.29)	**0.003***	0.19 (0.16–0.21)	**0.003***
Heterogeneous SDC	0.20 (0.17–0.28)	**0.042**	0.19 (0.17–0.23)	**0.005***
Homogeneous NDC	0.21 (0.18–0.27)	0.17	0.20 (0.16–0.22)	**0.036***
Heterogeneous NDC	0.21 (0.18–0.29)	0.12	0.19 (0.14–0.24)	**0.036***

Note: Results are first presented in the complete group consisting of all subjects with relevant WMH (All WMH) and then only for the group with a Fazekas score of 3 (High WMH). *p* values represent the comparison of model fit of each WMH-weighted model compared to the baseline model. Significant *p* values are illustrated in bold, and significant *p* values after multiple-comparison correction using the Benjamini–Hochberg correction are illustrated with *.
Abbreviations: NDC = node disconnectivity; SDC = structural disconnectivity.

We found that, when considering all subjects with WMH, SDC models yielded a significantly better fit compared to the baseline model, while NDC models performed better only when considering the specific subgroup with the highest Fazekas score (i.e., high WMH group). This finding suggests that alterations in inter-regional communication induced by WMH (as evidenced by SDC models) play a more prominent role in shaping global brain dynamics, namely reducing the strength of inter-regional communication (i.e., on the connectome edges). Only when a certain level of damage is reached, then disturbances in local nodal activity might play a role. In light of the location of WMH this is not an unexpected finding, but notably, modeling these effects considering the location-specific damage to WM tracts did not yield better descriptions of empirical data compared to considering their effect as globally homogeneous. This suggests that the damage associated with WMH might have dynamic repercussions at the whole-brain level. A previous study by Cabral et al. (2012) already showed in theoretical simulations that increasing levels of disconnections led to similar network reorganizations as reductions in global coupling. In this scenario, the more damage to white matter tracts, namely the higher the WMH load, the more the dynamical effects caused by disconnections resemble those occurring from a reduction in global coupling. From a biological perspective, a previous study also showed the existence of a widespread damage to white matter tracts that are not observable with structural MRI, of which WMH are just the tip-of-the-iceberg (Maillard et al. 2011; ter Telgte et al. 2018). WMH are surrounded by an area without abnormalities on conventional MRI, but where diffusion metrics in diffusion tractography are already altered (Maillard et al. 2011; Maniega et al. 2015). We suggest that these unobservable lesions might already determine communication impairments in widespread networks. In this scenario, the damage that was accounted for in the heterogeneous SDC model might thus be underestimated compared to the damage to the real empirical network. Thus, a global measure

TABLE 2 | Correlations (Spearman's *r*) between the percentage increase in model performance compared to the baseline for each WMH-weighted model and the considered demographic variables.

	Homogeneous SDC		Heterogeneous SDC		Homogeneous NDC		Heterogeneous NDC	
Demographic variable	***r***	***p***	***r***	***p***	***r***	***p***	***r***	***p***
WMH volume (log)	0.27	**0.01**	0.29	**0.007**	0.23	**0.03**	0.27	**0.01**
Age	0.15	0.16	0.23	**0.03**	0.21	0.052	0.10	0.35
MMSE	−0.19	0.08	−0.15	0.17	−0.13	0.23	−0.10	0.36
Education (years)	−0.26	**0.02**	−0.21	**0.045**	−0.21	0.055	0.16	0.14

Note: All correlations refer to partial correlations corrected for age, except for age itself. Significant *p* values are illustrated in bold.
Abbreviations: MMSE = Mini Mental State Examination; NDC = node disconnectivity; SDC = structural disconnectivity.

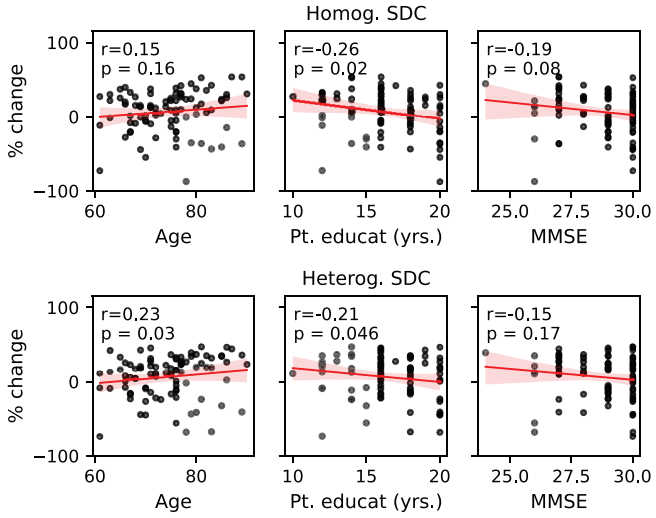

FIGURE 4 | Scatterplots depicting the correlation between demographics factors (age, years of patient education and mini-mental status examination (MMSE), and the percentage improvement in model performance of the considered model compared to the baseline model. The first row shows the results for the homogeneous structural disconnectivity model (SDC), while the second row shows the results for the heterogeneous SDC. For age, r refers to Spearman's rank correlation, while for patient education and MMSE, r refers to Spearman's partial correlation accounting for age. p = p-value, not corrected for multiple comparisons.

of WMH (since we perform a linear fitting) might be enough to capture this damage. Future studies using advanced diffusion-tractography-based measurements (e.g., fractional anisotropy) could further evaluate this hypothesis by also accounting for the normal-appearing white matter damage. Albeit previous associational studies on the effects of WMH on inter-regional FC are mixed (Schulz et al. 2021) and the association might be confounded by several factors (see next paragraph), our results are in line with the prevailing idea that WMH mostly reduces long-distance FC (Quandt et al. 2020; Yang et al. 2023) and consequently increase local efficiency (Vergoossen et al. 2021). The increase in local efficiency is also predicted by computational models characterized by a reduction in global coupling (Cabral et al. 2012), thus we are planning a future study to investigate whether this relationship can also be observed in our models fitted to empirical data of subjects with WMH.

Interestingly, for both SDC models, we found an inverse association between model performance increase—compared with the baseline—and years of education. We speculate that this finding might be related to nonlinearities occurring in vivo caused by counteracting increases in global coupling associated with higher educational status that could be linked to the construct of "cognitive reserve". Cognitive reserve refers to a series of protective mechanisms that allow an individual to mitigate the detrimental effects of age or pathological biomarkers (e.g., amyloid, tau, WMH) to achieve better results than what would have been predicted by simply evaluating the observed damage (Stern 2009). Previous studies demonstrated that cognitive reserve is indeed related to increases in resting-state functional connectivity in distributed resting-state networks (Marques et al. 2016), as well as with a more integrated and interconnected network configuration (Chaddock-Heyman et al. 2018). Given the exploratory nature of this finding, future studies are needed to further explore this hypothesis.

When WMH become widely diffuse throughout the brain, namely when the Fazekas score is 3, then a more negative shift away from the bifurcation parameter of the nodes is also observed, that is, the dynamical behavior of the networks becomes noisier. This reduction in bifurcation parameters might be linked to other known pathological processes also associated with WMH, especially at later stages, such as tau and amyloid (Demirtaş et al. 2017; Patow et al. 2023). However, our study did not find any significant correlation between WMH and CSF levels of Aβ42/Aβ40 nor tau, suggesting that, if present, the interplay among these pathologies might be more intricate and not simply linear in nature. An alternative hypothesis is that neurons might not suffer from alterations to their intrinsic patterns of firing when demyelination and axonal damage are below a certain threshold, possibly due to compensatory mechanisms (Naud and Longtin 2019). Only when this threshold is surpassed, then abnormal neuronal firing might occur. Future studies might implement biophysically detailed models and account for both WMH and amyloid/tau to try to disentangle their separate and synergistic contributions to intrinsic regional dynamics.

Some limitations apply to this study, some intrinsically linked to the methodology of rs-fMRI. The BOLD signal does not directly measure neuronal activity per se, but rather slow oscillations deriving from neuro-vascular coupling (Logothetis 2003; Logothetis and Wandell 2004). WMH are commonly associated with cerebral small vessel disease, thus, they might be associated with whole-brain level alterations of neuro-vascular coupling (Girouard and Iadecola 2006), increasing the intricacy in the interpretation of our results. Another limitation of our study is the age difference between the group with and without WMH. WMH are intrinsically associated with the aging process, resulting in an older average age for the cohort with WMH compared to the control group without WMH. To address the influence of the age difference, we evaluated the partial correlations corrected by age between increases in model performance and WMH and demographics variables. Furthermore, we used a normative SC for both groups, mitigating the potential impact of the age difference on SC measures. Another limitation is that model-derived parameters did not correlate with cognitive function scores, which are known to be impacted in subjects with WMH. A possible explanation is that in our study, we focused on fitting models to achieve the best average of single-subject fitting (i.e., using the same weight and bias for all subjects). While this resulted in models that could be applied to unseen subjects for a good representation of their dynamics, certain individual characteristics were not represented, leading to a lack of correlation with cognitive scores on a subject-specific basis. Lastly, our modeling approach, as common to many previous modeling studies using the Hopf model with rs-fMRI (Deco et al. 2017; Demirtaş et al. 2017; Sanz Perl et al. 2023), did not include delays due to the longer timescales of the BOLD signal acquisition (seconds vs. the millisecond scale of inter-neuronal signaling), but studying the heterogeneous effects of WMH on delays could be an interesting direction to explore in future studies.

In summary, our study provides further understanding of the dynamical effects of WMH, suggesting the presence of an

associated widespread damage to WM tracts with relevant dynamical effects on global synchronization and, at later stages, also on regional brain dynamics. The models developed in this study also show promise for clinical applications, that is, in predicting subject-specific network effects in the presence of WMH. The pathophysiological insights developed and discussed in this study might be used, alone or in combination with other biomarkers (e.g., tau and amyloid), to inform and create more biologically plausible representations of brain dynamics in several diseases characterized by WMH, such as Alzheimer's disease, but also in other pathologies harboring WM disconnections (e.g., multiple sclerosis, traumatic brain injury). Furthermore, our study highlights the importance of whole-brain modeling to reconcile theoretical predictions with the nuances and complexities arising from biological findings, effectively bridging the gap between the two.

Author Contributions

R.L.: conceptualization, formal analysis, writing – original draft, writing – review and editing. **S.G.:** data curation, writing – review and editing. **G.D.:** conceptualization, writing – review and editing. **X.K.:** conceptualization, formal analysis, writing – review and editing.

Acknowledgments

Data collection and sharing for this project was funded by the Alzheimer's Disease Neuroimaging Initiative (ADNI) (National Institutes of Health Grant U01 AG024904) and DOD ADNI (Department of Defense award number W81XWH-12-2-0012). ADNI is funded by the National Institute on Aging, the National Institute of Biomedical Imaging and Bioengineering, and through generous contributions from the following: AbbVie, Alzheimer's Association; Alzheimer's Drug Discovery Foundation; Araclon Biotech; BioClinica Inc.; Biogen; Bristol-Myers Squibb Company; CereSpir Inc.; Cogstate; Eisai Inc.; Elan Pharmaceuticals Inc.; Eli Lilly and Company; EuroImmun; F. Hoffmann-La Roche Ltd. and its affiliated company Genentech Inc.; Fujirebio; GE Healthcare; IXICO Ltd.; Janssen Alzheimer Immunotherapy Research & Development LLC.; Johnson & Johnson Pharmaceutical Research & Development LLC.; Lumosity; Lundbeck; Merck & Co. Inc.; Meso Scale Diagnostics LLC.; NeuroRx Research; Neurotrack Technologies; Novartis Pharmaceuticals Corporation; Pfizer Inc.; Piramal Imaging; Servier; Takeda Pharmaceutical Company; and Transition Therapeutics. The Canadian Institutes of Health Research is providing funds to support ADNI clinical sites in Canada. Private sector contributions are facilitated by the Foundation for the National Institutes of Health (www.fnih.org). The grantee organization is the Northern California Institute for Research and Education, and the study is coordinated by the Alzheimer's Therapeutic Research Institute at the University of Southern California. ADNI data are disseminated by the Laboratory for Neuro Imaging at the University of Southern California.

Consent

Patient informed consent was acquired by ADNI Investigators at each participating site.

Conflicts of Interest

The authors declare no conflicts of interest.

Data Availability Statement

The data set is owned by a third-party organization; the Alzheimer's Disease Neuroimaging Initiative (ADNI). Data are publicly and freely available from the http://adni.loni.usc.edu/data-samples/access-data/InstitutionalDataAccess/EthicsCommittee (contact via http://adni.loni.usc.edu/data-samples/access-data/) upon sending a request that includes the proposed analysis and the name of the lead investigator. Code to reproduce the analyses will be made available on https://github.com/computational-neurology upon publication of the results.

References

Adebimpe, A., M. Bertolero, K. Mehta, et al. 2023. XCP-D: A Robust Postprocessing Pipeline of fMRI Data. https://doi.org/10.5281/zenodo.7641626.

Alstott, J., M. Breakspear, P. Hagmann, L. Cammoun, and O. Sporns. 2009. "Modeling the Impact of Lesions in the Human Brain." *PLoS Computational Biology* 5: e1000408.

Benjamini, Y., and Y. Hochberg. 1995. "Controlling the False Discovery Rate: A Practical and Powerful Approach to Multiple Testing." *Journal of the Royal Statistical Society: Series B: Methodological* 57: 289–300.

Cabral, J., E. Hugues, M. L. Kringelbach, and G. Deco. 2012. "Modeling the Outcome of Structural Disconnection on Resting-State Functional Connectivity." *NeuroImage* 62: 1342–1353.

Cakan, C., N. Jajcay, and K. Obermayer. 2021. "Neurolib: A Simulation Framework for Whole-Brain Neural Mass Modeling." *Cognitive Computation* 15: 1132–1152. https://doi.org/10.1007/s12559-021-09931-9.

Chaddock-Heyman, L., T. B. Weng, C. Kienzler, et al. 2018. "Scholastic Performance and Functional Connectivity of Brain Networks in Children." *PLoS One* 13: e0190073.

Debette, S., and H. S. Markus. 2010. "The Clinical Importance of White Matter Hyperintensities on Brain Magnetic Resonance Imaging: Systematic Review and Meta-Analysis." *BMJ* 341: c3666.

Deco, G., J. Cruzat, J. Cabral, et al. 2019. "Awakening: Predicting External Stimulation to Force Transitions Between Different Brain States." *Proceedings of the National Academy of Sciences of the United States of America* 116: 18088–18097.

Deco, G., V. K. Jirsa, and A. R. McIntosh. 2011. "Emerging Concepts for the Dynamical Organization of Resting-State Activity in the Brain." *Nature Reviews. Neuroscience* 12: 43–56.

Deco, G., M. L. Kringelbach, V. K. Jirsa, and P. Ritter. 2017. "The Dynamics of Resting Fluctuations in the Brain: Metastability and Its Dynamical Cortical Core." *Scientific Reports* 7: 3095.

Demirtaş, M., C. Falcon, A. Tucholka, J. D. Gispert, J. L. Molinuevo, and G. Deco. 2017. "A Whole-Brain Computational Modeling Approach to Explain the Alterations in Resting-State Functional Connectivity During Progression of Alzheimer's Disease." *Neuroimage Clinical* 16: 343–354.

Esteban, O., C. J. Markiewicz, R. W. Blair, et al. 2019. "fMRIPrep: A Robust Preprocessing Pipeline for Functional MRI." *Nature Methods* 16: 111–116.

Fazekas, F., J. B. Chawluk, A. Alavi, H. I. Hurtig, and R. A. Zimmerman. 1987. "MR Signal Abnormalities at 1.5 T in Alzheimer's Dementia and Normal Aging." *American Journal of Roentgenology* 149: 351–356.

Garnier-Crussard, A., F. Cotton, P. Krolak-Salmon, and G. Chételat. 2023. "White Matter Hyperintensities in Alzheimer's Disease: Beyond Vascular Contribution." *Alzheimer's & Dementia* 19: 3738–3748.

Gibbons, L. E., A. C. Carle, R. S. Mackin, et al. 2012. "A Composite Score for Executive Functioning, Validated in Alzheimer's Disease Neuroimaging Initiative (ADNI) Participants With Baseline Mild Cognitive Impairment." *Brain Imaging and Behavior* 6: 517–527.

Girouard, H., and C. Iadecola. 2006. "Neurovascular Coupling in the Normal Brain and in Hypertension, Stroke, and Alzheimer Disease." *Journal of Applied Physiology* 100: 328–335.

Griffis, J. C., N. V. Metcalf, M. Corbetta, and G. L. Shulman. 2021. "Lesion Quantification Toolkit: A MATLAB Software Tool for Estimating Grey Matter Damage and White Matter Disconnections in Patients With Focal Brain Lesions." *NeuroImage: Clinical* 30: 102639.

Idesis, S., C. Favaretto, N. V. Metcalf, et al. 2022. "Inferring the Dynamical Effects of Stroke Lesions Through Whole-Brain Modeling." *NeuroImage: Clinical* 36: 103233.

Jenkins, L. M., A. Kogan, M. Malinab, et al. 2021. "Blood Pressure, Executive Function, and Network Connectivity in Middle-Aged Adults at Risk of Dementia in Late Life." *Proceedings of the National Academy of Sciences of the United States of America* 118: e2024265118.

Kantarovich, K., L. Mwilambwe-Tshilobo, S. Fernández-Cabello, et al. 2022. "White Matter Lesion Load Is Associated With Lower Within- and Greater Between-Network Connectivity Across Older Age." *Neurobiology of Aging* 112: 170–180.

Kobeleva, X., G. Varoquaux, A. Dagher, M. H. Adhikari, C. Grefkes, and M. Gilson. 2022. "Advancing Brain Network Models to Reconcile Functional Neuroimaging and Clinical Research." *NeuroImage: Clinical* 36: 103262.

Li, H., G. Jiang, J. Zhang, et al. 2018. "Fully Convolutional Network Ensembles for White Matter Hyperintensities Segmentation in MR Images." *NeuroImage* 183: 650–665.

Logothetis, N. K. 2003. "The Underpinnings of the BOLD Functional Magnetic Resonance Imaging Signal." *Journal of Neuroscience* 23: 3963–3971.

Logothetis, N. K., and B. A. Wandell. 2004. "Interpreting the BOLD Signal." *Annual Review of Physiology* 66: 735–769.

Maillard, P., E. Fletcher, D. Harvey, et al. 2011. "White Matter Hyperintensity Penumbra." *Stroke* 42: 1917–1922.

Maniega, S. M., M. C. Valdés Hernández, J. D. Clayden, et al. 2015. "White Matter Hyperintensities and Normal-Appearing White Matter Integrity in the Aging Brain." *Neurobiology of Aging* 36: 909–918.

Marques, P., P. Moreira, R. Magalhães, et al. 2016. "The Functional Connectome of Cognitive Reserve." *Human Brain Mapping* 37: 3310–3322.

Min, Z., H. R. Shan, L. Xu, et al. 2021. "Diffusion Tensor Imaging Revealed Different Pathological Processes of White Matter Hyperintensities." *BMC Neurology* 21: 128.

Nagendran, T., R. S. Larsen, R. L. Bigler, et al. 2017. "Distal Axotomy Enhances Retrograde Presynaptic Excitability Onto Injured Pyramidal Neurons via Trans-Synaptic Signaling." *Nature Communications* 8: 625.

Naud, R., and A. Longtin. 2019. "Linking Demyelination to Compound Action Potential Dispersion With a Spike-Diffuse-Spike Approach." *Journal of Mathematical Neuroscience* 9: 3.

Patow, G., L. Stefanovski, P. Ritter, G. Deco, X. Kobeleva, and for the Alzheimer's Disease Neuroimaging Initiative. 2023. "Whole-Brain Modeling of the Differential Influences of Amyloid-Beta and Tau in Alzheimer's Disease." *Alzheimer's Research & Therapy* 15: 210.

Quandt, F., F. Fischer, J. Schröder, et al. 2020. "Higher White Matter Hyperintensity Lesion Load Is Associated With Reduced Long-Range Functional Connectivity." *Brain Communications* 2: fcaa111.

Sanz Perl, Y., S. Fittipaldi, C. Gonzalez Campo, et al. 2023. "Model-Based Whole-Brain Perturbational Landscape of Neurodegenerative Diseases." *eLife* 12: e83970.

Schlemm, E., B. M. Frey, C. Mayer, et al. 2022. "Equalization of Brain State Occupancy Accompanies Cognitive Impairment in Cerebral Small Vessel Disease." *Biological Psychiatry* 92: 592–602.

Schulz, M., C. Malherbe, B. Cheng, G. Thomalla, and E. Schlemm. 2021. "Functional Connectivity Changes in Cerebral Small Vessel Disease—A Systematic Review of the Resting-State MRI Literature." *BMC Medicine* 19: 103.

Shaw, L. M., H. Vanderstichele, M. Knapik-Czajka, et al. 2009. "Cerebrospinal Fluid Biomarker Signature in Alzheimer's Disease Neuroimaging Initiative Subjects." *Annals of Neurology* 65: 403–413.

Škoch, A., B. Rehák Bučková, J. Mareš, et al. 2022. "Human Brain Structural Connectivity Matrices–Ready for Modelling." *Scientific Data* 9: 486.

Sporns, O. 2013. "Structure and Function of Complex Brain Networks." *Dialogues in Clinical Neuroscience* 15: 247–262.

Stern, Y. 2009. "Cognitive Reserve." *Neuropsychologia* 47: 2015–2028.

Suárez, L. E., R. D. Markello, R. F. Betzel, and B. Misic. 2020. "Linking Structure and Function in Macroscale Brain Networks." *Trends in Cognitive Sciences* 24: 302–315.

Svärd, D., M. Nilsson, B. Lampinen, et al. 2017. "The Effect of White Matter Hyperintensities on Statistical Analysis of Diffusion Tensor Imaging in Cognitively Healthy Elderly and Prodromal Alzheimer's Disease." *PLoS One* 12: e0185239.

ter Telgte, A., E. M. C. van Leijsen, K. Wiegertjes, C. J. M. Klijn, A. M. Tuladhar, and F. E. de Leeuw. 2018. "Cerebral Small Vessel Disease: From a Focal to a Global Perspective." *Nature Reviews. Neurology* 14: 387–398.

Thiebaut de Schotten, M., C. Foulon, and P. Nachev. 2020. "Brain Disconnections Link Structural Connectivity With Function and Behaviour." *Nature Communications* 11: 5094.

Tzourio-Mazoyer, N., B. Landeau, D. Papathanassiou, et al. 2002. "Automated Anatomical Labeling of Activations in SPM Using a Macroscopic Anatomical Parcellation of the MNI MRI Single-Subject Brain." *NeuroImage* 15: 273–289.

Vergoossen, L. W. M., J. F. A. Jansen, T. T. van Sloten, et al. 2021. "Interplay of White Matter Hyperintensities, Cerebral Networks, and Cognitive Function in an Adult Population: Diffusion-Tensor Imaging in the Maastricht Study." *Radiology* 298: 384–392.

Wardlaw, J. M., M. C. Valdés Hernández, and S. Muñoz Maniega. 2015. "What Are White Matter Hyperintensities Made of?" *Journal of the American Heart Association* 4: 1–19.

Yang, D., J. Li, Z. Ke, et al. 2023. "Subsystem Mechanisms of Default Mode Network Underlying White Matter Hyperintensity-Related Cognitive Impairment." *Human Brain Mapping* 44: 2365–2379.

Supporting Information

Additional supporting information can be found online in the Supporting Information section.

3.4 Publication 4: A Whole-Brain Model of the Aging Brain During Slow Wave Sleep

eNeuro

Research Article: New Research
Integrative Systems

A Whole-Brain Model of the Aging Brain During Slow Wave Sleep

Eleonora Lupi,[1]* Gabriele Di Antonio,[2,3,4]* Marianna Angiolelli,[5]* Maria Sacha,[6]* Mehmet Alihan Kayabas,[7]* Nicola Alboré,[2,4,8]* Riccardo Leone,[9,10,11]* Karim El Kanbi,[12] Alain Destexhe,[6] and Jan Fousek[13]****

[1]Department of Brain and Behavioral Sciences, University of Pavia, Pavia 27100, Italy, [2]Research Center "Enrico Fermi", Rome 00184, Italy, [3]"Roma Tre" University of Rome, Rome 00146, Italy, [4]Natl. Center for Radiation Protection and Computational Physics, Istituto Superiore di Sanità, Rome 00161, Italy, [5]Department of Engineering, Università Campus Bio-Medico di Roma, Rome 00128, Italy, [6]Institute of Neuroscience (NeuroPSI), Paris-Saclay University, Centre National de la Recherche Scientifique (CNRS), Saclay 91400, France, [7]Univ Rennes, INSERM, Rennes 35043, France, [8]"Tor Vergata" University of Rome, Rome 00133, Italy, [9]Faculty of Medicine, University of Bonn, Bonn 53115, Germany, [10]Computational Neurology Group, Ruhr University Bochum, Bochum 44801, Germany, [11]Deutsches Zentrum für Neurodegenerative Erkrankungen (DZNE), Bonn 53127, Germany, [12]DREEM, Paris 75003, France, and [13]Central European Institute of Technology (CEITEC), Masaryk University, Brno 62500, Czech Republic

Visual Abstract

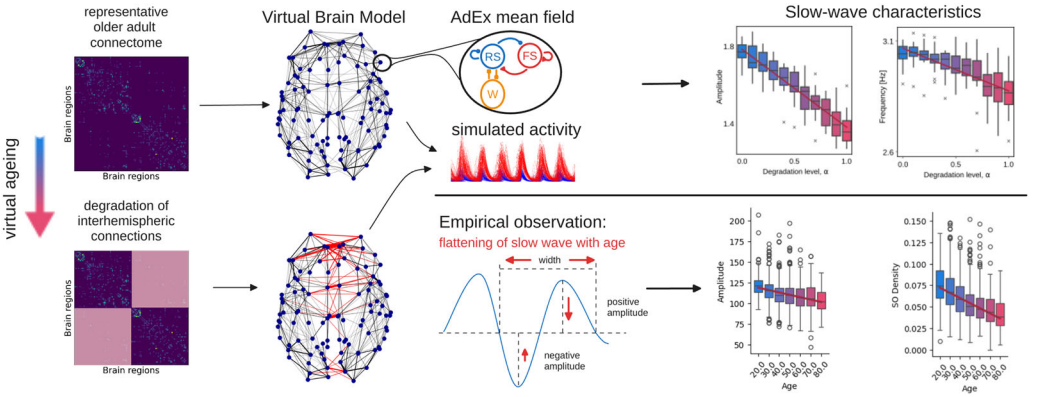

Received April 26, 2024; revised Sept. 18, 2024; accepted Oct. 2, 2024.

The authors declare no competing financial interests.

E.L., G.D., A.D., and J.F. designed research; E.L., G.D., M.A., M.S., M.K., N.A., R.L., K.E., A.D., and J.F. performed research; E.L., G.D., M.A., M.S., M.K., N.A., R.L., K.E., A.D., and J.F. analyzed data; E.L., G.D., M.A., M.S., M.K., N.A., R.L., K.E., A.D., and J.F. wrote the paper.

Eleonora Lupi is a PhD student enrolled in the National PhD in Artificial Intelligence, XXXVIII cycle, course on Health and life sciences, organized by Università Campus Bio-Medico di Roma. Jan Fousek receives funding from the European Union's Horizon Europe research and innovation programme under the Marie Sklodowska-Curie grant agreement No 101130827. Research supported by CNRS and the European Union (Human Brain Project H2020-785907 and H2020-945539). No additional acknowledgements beside the funding sources.

Continued on next page.

Abstract

Age-related brain changes affect sleep and are reflected in properties of sleep slow-waves, however, the precise mechanisms behind these changes are still not completely understood. Here, we adapt a previously established whole-brain model relating structural connectivity changes to resting state dynamics, and extend it to a slow-wave sleep brain state. In particular, starting from a representative connectome at the beginning of the aging trajectory, we have gradually reduced the inter-hemispheric connections, and simulated sleep-like slow-wave activity. We show that the main empirically observed trends, namely a decrease in duration and increase in variability of the slow waves are captured by the model. Furthermore, comparing the simulated EEG activity to the source signals, we suggest that the empirically observed decrease in amplitude of the slow waves is caused by the decrease in synchrony between brain regions.

Significance Statement

Aging is characterized by changes in slow wave (SW) sleep features, yet the precise mechanisms driving these alterations remain elusive. Employing a connectome-based model, we implement the established age-related reductions in inter-hemispheric connectivity, successfully replicating the SW changes in the simulated activity. Our simulation of EEG activity also suggests that observed decreases in SW amplitude stems from diminished synchrony between brain regions. Our results support the notion that alterations in SW characteristics result from reductions in cortical excitatory drive—here facilitated by the inter-hemispheric connections. Our model serves as a robust foundation for extensions to population studies and interventional work in animal models of aging aimed at disentangling the contributions of network alterations, changes to local neural mass properties, and neuromodulation.

Introduction

Slow waves (SW) are neural oscillations occurring during non-rapid eye movement (NREM) sleep that are characterized by a phase of hyperpolarization (down period), during which cortical neurons are silent, and by a phase of depolarization, in which intense neuronal firing occurs (up period) (Steriade et al., 1993). SW characteristics vary across the lifespan, changing in both healthy (Van Cauter et al., 2000; Landolt and Borbély, 2001; Mander et al., 2017) and pathological aging. Compared to young subjects, older individuals show a lower percentage of deep SW sleep (Van Cauter et al., 2000; Landolt and Borbély, 2001; Mander et al., 2017), lower SW density and amplitude, especially at the beginning and end of the night (El Kanbi et al., 2023), and both longer SW positive and negative phase duration, especially in prefrontal/frontal brain areas (Carrier et al., 2011). Furthermore, in a recent study of more than 2000 individuals, El Kanbi et al. (2023) also found that slow-wave inducing auditory stimulation during N3 (Debellemaniere et al., 2018) were much less successful in older subjects compared to younger ones. Although these descriptive changes of SW characteristics with aging are well known in the literature, the exact mechanisms linking aging to alterations in SW are still not fully elucidated.

Aging is associated with many structural brain alterations involving both the gray (Giorgio et al., 2010; Bethlehem et al., 2022) and white matter (Antonenko and Flöel, 2014; Damoiseaux, 2017; Puxeddu et al., 2020; Lavanga et al., 2023a) that might be implicated in the alteration of SW. Previous studies showed a reduction in cortical gray matter occurring across the lifespan (Giorgio et al., 2010; Bethlehem et al., 2022) and this has already been linked to alterations in SW (Dubé et al., 2015). Reduced cortical thickness in regions that are normally involved in SW generation (e.g., insula, superior temporal, parietal, middle frontal) mediated the negative effects of aging on SW density, whereas reduced SW amplitude was associated with reduced cortical thickness in middle frontal, medial prefrontal, and medial posterior regions (Dubé et al., 2015). Another prominent aspect of age-related structural changes is the reduction in white matter connections (Antonenko and Flöel, 2014; Damoiseaux, 2017) which was shown to occur especially for inter-hemispheric connections (Puxeddu et al., 2020; Lavanga et al., 2023a). Inter-hemispheric connections have a prominent influence on aspects of coordinated neural dynamics both during awake resting state activity (Lavanga et al., 2023a), and during sleep (Avvenuti et al., 2020). In the awake state, reductions in inter-hemispheric connectivity have been linked to a reduction in functional dynamical flexibility (Lavanga et al., 2023a). During sleep, a previous study on callosotomized patients with drug-resistant epilepsy (Avvenuti et al., 2020) reported that SW displayed a significantly reduced probability of cross-hemispheric propagation and a stronger interhemispheric asymmetry compared to controls (Avvenuti et al., 2020). Nevertheless, if reduced inter-hemispheric connectivity might play a role in shaping SW characteristics during normal aging has not yet been investigated.

Connectome-based whole-brain modeling frameworks, such as The Virtual Brain (TVB) (Sanz-Leon et al., 2015; Schirner et al., 2022), can create personalized virtual brain models (Ghosh et al., 2008; Deco and Corbetta, 2011), that can integrate individual structural brain imaging data and, based on the mean field model (Abbott and van Vreeswijk, 1993; Treves, 1993; Brunel and Hakim, 1999; Knight, 2000; Mattia and Del Giudice, 2002) governing the dynamics of each node of the network, capture the characteristics of resting-state (Lavanga et al., 2023a) or SW dynamics (Goldman et al., 2022). Using a spiking model of adaptive exponential integrate and fire (AdEx) neurons, El Kanbi et al. (2023)

*EL, GDA, MA, MS, MAK, NA and RL are equally contributing first authors.

**AD and JF are equally contributing last authors.

Correspondence should be addressed to Jan Fousek at jan.fousek@ceitec.muni.cz.

suggest that the reduction of the excitatory drive might be the mechanism behind the observed SW changes on the level of individual neuronal populations. Here, we aim to investigate to which degree this reduction of excitatory drive might be related to the reduction of inter-hemispheric connectivity. In particular, by using the AdEx mean field model (Di Volo et al., 2019) and structural connectivity matrices representative of the participants of the 1000BRAINS study (Caspers et al., 2014) at the beginning of the aging trajectory, we recapitulate the main aging-associated alterations of EEG slow-wave recordings (El Kanbi et al., 2023) by manipulating the underlying structural connectivity (Lavanga et al., 2023a) (i.e., by reducing the connection strengths of inter-hemispheric tracts, Fig. 1). Then, we investigate the changes of the slow-wave characteristics in the model along the virtual ageing trajectory on the source level, and relate these to the hypothesized decrease of the excitatory drive and changes in synchrony. Through this simulation-based approach, we aim to gain insights into the underlying mechanisms linking aging, inter-hemispheric connectivity, and slow wave dynamics.

Methods

Structural connectivity. An anonymized connectome was drawn from an embedding of structural connectivity matrices of the youngest subjects of the 1000BRAINS project (Caspers and Schreiber, 2021; Lavanga et al., 2023b). The original connectomes resulted from a pipeline described in detail in Caspers et al. (2014). In short, for each participant, a T1-weighted and diffusion-weighted MRI images were obtained. The T1 scan (MPRAGE, 176 slices, TR = 2.25 s, TE = 3.03 ms, TI = 900 ms, FoV = 256 × 256 mm^2, flip angle = 9°, resolution 1 mm isotropic) was used to extract cortical grey matter masks, which were divided into 100 regions using the Schaefer parcellation scheme (17-Networks, Schaefer et al., 2018). The diffusion MRI (two *b*-value scans b = 1,000 s/mm^2 (EPI, TR = 6.3 s, TE = 81 ms, 7 b0-images and 60 DW volumes) and b = 2, 700 s/mm^2 (EPI, TR = 8 s, TE = 112 ms, 13 b0-images and 120 DW volumes)) were registered to the T1 images, and used to generate streamlines between the respective regions defined by the parcellation, resulting in a 100 × 100 connectivity matrix. The representative connectome at the start of the aging trajectory was derived from the pseudonymized dataset (Caspers and Schreiber, 2021, N = 645, age 55–63 years).

The representative connectome for the subjects at the start of the aging trajectory was computed from 220 connectomes of subjects in the age group of 55–63 years. The connectomes were linearized and stacked resulting in a 220×100^2 matrix W. The matrix W was then factorized using singular value decomposition giving $W = USV^H$. The first 33 components were sufficient to eliminate any confusion when the connectomes were projected back into this space, so we have set the dimension of the generative distribution constructed in the next step to $d = 33$. The matrix U can be cast into a multivariate normal distribution $\mathcal{U}_N = (\mu, \Sigma)$ such that means are $\mu_i = avg_{j,j<d}(U_{ij})$ and the covariance $\Sigma = cov(U^T_{ij,j<d})$. A sample U' drawn from the U_N is then converted to a connectome W' by computing $W' = U' diag S_{ij,j<d} V^T_{ij,j<d}$ and devectorizing W' back to a 100×100 matrix.

Virtually aged structural connectome. The structural connectome was virtually aged (Lavanga et al., 2023a) by gradually decreasing the interhemispheric connections. In particular, given the weighted connectivity matrix W and the matrix M^α such that $M^\alpha_{ij} = 1$ for intra-hemispheric connections, and $M^\alpha_{ij} = 1 - \alpha$ for inter-hemispheric connections, the gradually aged connectome was computed as element-wise product $W_\alpha = W \odot M_\alpha$ for $\alpha \in [0, 6]$ with a step of 0.1, resulting in 7 samples along the virtual aging trajectory. Here, the $\alpha = 0$ signifies an unaltered connectivity matrix, while $\alpha = 0.6$ corresponds to the highest reduction observed in the elderly subjects (Lavanga et al., 2023a).

Modeling. The Adaptive Exponential Integrate-and-Fire (AdEx) model is a biologically realistic neuron model that has been widely used to simulate the electrical activity of neurons (Brette and Gerstner, 2005). It is an extension of the classic integrate-and-fire model, incorporating both an exponential spike mechanism and an adaptation process. The mean field equations for the AdEx model includes conductance-based synaptic interactions and accounts for adaptation, leading to the following set of equations (Zerlaut et al., 2018; Di Volo et al., 2019; Goldman et al., 2022):

$$\begin{aligned} T\frac{\partial \nu_\mu}{\partial t} &= (F_\mu - \nu_\mu) + \frac{1}{2}\frac{\partial^2 F_\mu}{\partial \lambda \partial \eta} c_{\lambda\eta}, \\ T\frac{\partial c_{\lambda\eta}}{\partial t} &= \delta_{\lambda\eta}\frac{F_\lambda(1/T - F_\eta)}{N_\lambda} + (F_\lambda - \nu_\lambda)(F_\eta - \nu_\eta) + \frac{\partial F_\lambda}{\partial \nu_\mu} c_{\eta\mu} + \frac{\partial F_\eta}{\partial \nu_\mu} c_{\lambda\mu} - 2c_{\lambda\eta}, \\ \frac{\partial W_\mu}{\partial t} &= -\frac{W_\mu}{\tau_{w_\mu}} + b_\mu \nu_\mu + \frac{a_\mu\left[\mu_V(\nu_e, \nu_i, W_\mu) - E_{L_\mu}\right]}{\tau_{w_\mu}}, \end{aligned} \tag{1}$$

where ν_μ is the average firing rate of population $\mu = \{e, i\}$ (excitatory or inhibitory), $F_\mu = F_\mu(\nu_e + \nu_e^{in}, \nu_i + \nu_i^{in}, W_\mu)$ is the transfer function, ν_e^{in} and ν_i^{in} are the inputs to the excitatory and inhibitory populations, $c_{\lambda\eta}$ is the covariance between populations λ and η and W is a population adaptation variable (Di Volo et al., 2019). The mean field model can accurately predict the average spontaneous activity levels in asynchronous irregular regimes, capture the transient temporal response of the network to complex external inputs, and quantitatively describe regimes where high–and low-activity states alternate (up/down state dynamics).

The previous equations can be extended to describe large networks of interconnected brain regions, with each region being described by a mean-field model and the connectivity derived from human tractography (structural connectivity). In

Table 1. AdEx mean field model parameters

(a) Scalar parameters of the AdEx mean field model

parameter	value	parameter	value	parameter	value
C_m	200.0pF	S_i	1.2	g	0.2
E_{L_e}	−63.0 mV	T	40.0 ms	g_L	10.0 nS
E_{L_i}	−65.0 mV	a_e	0.0 nS	$p\text{con}_e$	0.05
E_e	0.0 mV	a_i	0.0 nS	$p\text{con}_i$	0.05
E_i	−80.0 mV	b_e	60.0 pA	T_{OU}	5.0 ms
$K\text{ext}_e$	400	b_i	0.0 pA	τ_e	5.0 ms
$K\text{ext}_i$	0	ν_e^{ex}	0.315e−3 kHz	τ_i	5.0 ms
N_{tot}	10,000	ν_e^{in}	0.000 kHz	τ_{w_e}	500.0 ms
Q_e	1.5 nS	ν_i^{ex}	0.315e−3 kHz	τ_{w_i}	1.0 ms
Q_i	5.0 nS	ν_i^{in}	0.000 kHz	noise weight	1e−4

(b) Values for the fitted polynomials P of the transfer function F_μ. See Di Volo et al. (2019) for detailed description. Values are given in V

cell type	P_0	P_{μ_V}	P_{σ_V}	P_{τ_V}	$P_{\mu_V^2}$	$P_{\sigma_V^2}$	$P_{\tau_V^2}$	$P_{\mu_V\sigma_V}$	$P_{\mu_V\tau_V}$	$P_{\sigma_V\tau_V}$
excitatory	−0.0498	0.00506	−0.025	0.0014	−0.00041	0.0105	−0.036	0.0074	0.0012	−0.0407
inhibitory	−0.0514	0.004	−0.0083	0.0002	−0.0005	0.0014	−0.0146	0.0045	0.0028	−0.0153

addtion, such network can be driven by noise to produce spontaneous activity. In particular, the network input enters at node k at time t by expanding the excitatory input term ν_e^{in} as

$$\nu_\mu^{in}(k, t) = G_\mu \sum_j C_{kj}\nu_e(j, t - D_{k,j}) + wOU(t)_k, \tag{2}$$

where G_μ is a scaling factor, C_{kj} is the connectivity matrix, $D_{k,j}$ is the propagation delay, w is the noise scaling factor, and $OU(t)_k$ is the noise drive defined as Ornstein-Uhlenbeck process:

$$T_{OU}\mathrm{d}OU = -OU\mathrm{d}t + \mathrm{d}W_t, \tag{3}$$

where T_{OU} is time constant and $\mathrm{d}W_t$ is an increment of a Wiener process. The network input is scaled differently for the inhibitory and excitatory populations given the S_i constant, such that $G_e = S_i G$. The parameters of the model were adapted from Goldman et al. (2022) and are listed in Table 1.

For the following analyses, 30 s of data were simulated and the first initial transient of 2 s was discarded before further processing.

EEG

The EEG observer model complements the generative model of the brain dynamics (that is the networked AdEx model) in order to provide simulated EEG signals. Here, four virtual electrodes were positioned on the forehead to simulate the placement of headband devices commonly used in sleep studie s, i.e., the Dreem Headband (Arnal et al., 2020). A detailed view of the electrodes placement is presented in Extended Data Figure 2-3. Given the small number of electrodes and coarse-grained spatial resolution of the dynamical model, a simplified forward solution ommiting the conductivities and dipole orientation was employed (Sarvas, 1987). The elements of the leadfield matrix L prescribing the contribution of each of the brain network nodes to the sensor-level signals, were calculated as follows:

$$L_{ij} = 1/d_{ij}^2$$

where d_{ij} is the euclidean distance between brain region i the electrode j. The EEG signals are then derived as the dot product between the lead field matrix and the output of the AdEx model.

Analysis

Detection of up- and down-states

The dynamics of the model in the sleep-like regime exhibits regular slow-wave dynamics, characterized by alternating periods of high and low activity (up- and down-states, Goldman et al., 2022). In order to quantify this dynamical pattern, we applied the following steps to identify and evaluate the up- and down-states in both the EEG and source-level time-series. The simulated EEG time-series was first normalized in the [0 – 1] range and then binarized using a threshold of 0.5 (see Extended Data Fig. 5-2). Up-states were defined as having higher activity than the threshold and down-states as having lower activity than the threshold, respectively. Then, the start and length of each up or down state were identified, and only cycles where both states

lasted at least 50 milliseconds were considered for further analysis. Same procedure was also applied on the source-level time-series, with the binarization threshold of 0.3, and duration threshold of 40 milliseconds. A detailed view of the behavior for various time and amplitude thresholds for the source-level signals is presented in Extended Data Figure 3-1, and for the simulated EEG in Figure 2-2. The particular values of the thresholds were chosen to avoid misinterpreting noise-driven fluctuation in the down-state (threshold too low), and missing lower-amplitude up-states (threshold too high).

Slow wave characterization

To evaluate the effects of aging on the SW properties, we particularly focused on the following variables: average SW frequency, average up and down-state duration, the coefficient of variance of the SW frequency and synchrony. Each of these is further detailed below. First, the total duration of each up-down cycle was extracted as the time interval from the first point above the selected threshold to the last point recorded before the onset of a new up-state. The corresponding frequency for each SW was taken as the inverse of the duration, then the mean and standard deviation were computed based on the distribution of these frequency values, and the coefficient of variation (CV) was calculated as the ratio of the standard deviation to the mean (following El Kanbi et al., 2023).

To evaluate the effect of aging on the simulated SW EEG sleep-like activity, we focused on key parameters, including average frequency of the slow oscillations (SO), average up and down-state duration, CV of the SO and average amplitude of the SO. The data features were calculated for the EEG sensor time-series in the same way as described above for the source-level signals. Results are reported as averages across the simulated EEG channels.

On the source level, we report both the averages across all nodes of the brain network, and for the individual nodes (in a form of a spatial map), in order to account for the potential differential effects of aging across the network nodes. We also explored how the change through the synthetic aging in the above-mentioned features of the slow waves relates to the graph-theoretical measures of node significance in the structural network (node strength and eigenvector centrality). Briefly, node strength is quantified as the aggregate of the weights of all edges connected to a node, offering a measure of its significance in a weighted network. Eigenvector centrality, on the other hand, assigns scores to nodes relative to the quality of their connections, where links to nodes with high scores are more important in determining a node's score than links to nodes with lower scores. Consequently, a node with high eigenvector centrality indicates that many of its connections are to other nodes that also have high eigenvector scores.

Phase synchrony

In order to characterize the phase synchrony between the different nodes, the phase locking value (PLV) was calculated. PLV was originally introduced by Lachaux et al. (1999), and it was previously used in the analysis of resting state connectivity in magnetoencephalography (MEG) (Ghuman et al., 2011), as it provides a tool to analyse temporal relationships between two neural signals without considering the amplitude of the signal. PLV expresses the absolute value of the mean phase difference between two signals and can be described as follows:

$$\mathrm{PLV} = \left| \frac{1}{N} \sum_{t=1}^{N} e^{i(\phi_i(t) - \phi_j(t))} \right|,$$

where i and j the indices of nodes, $\phi(t)$ the phase of the time series extracted by the Hilbert transform at time t and N is the total number of time points, so that the metric was computed for each pair of node i, j and averaged over time. PLV values range between 0 and 1 for random and fixed phase relationships, respectively. Thus, higher values describe higher degree of synchrony. In our case, we apply PLV at the source-level of the simulated data—that is directly to the time-series of the state

Table 2. Listing of the frontal areas included in the frontal areas synchrony exploration in Figure 5

Hemisphere	Network	Acronym
LH	LimbicB	OFC
LH	ContA	PFCl
LH	ContB	PFClv
LH	DefaultA	PFCm
LH	DefaultB	PFCv
LH	DefaultB	PFCv
RH	SalVentAttnB	PFCl
RH	LimbicB	OFC
RH	ContA	PFCl
RH	ContB	PFClv
RH	DefaultA	PFCm
RH	DefaultB	PFCv
RH	DefaultB	PFCv

variables of the AdEx model in each of the nodes—hence avoiding any volume conduction biases common in EEG applications (Stam et al., 2007).

The metric was calculated by definition for each pair of nodes, for the two types of populations (excitatory and inhibitory) resulting in a nodes × nodes symmetric matrix *M*. The mean of the matrix excluding the diagonal elements was averaged over all trials to provide an estimation of whole-brain synchrony across different degrees of virtual aging. The intra- and inter-hemispheric synchrony (per hemisphere) was also explored separately, by averaging over the relevant submatrices of *M* (top-right for interhemispheric, top-left for right intrahemispheric and bottom-right for left interhemispheric synchrony). Additionally, the synchrony of frontal brain regions was calculated (see Table 2 and Fig. 5-1 for details on the regions), motivated by the frontal position of the electrodes in the experimental data (El Kanbi et al., 2023).

Code accessibility

Codes implementing the simulation and analysis steps described above are publicly available as Extended Data 1 and in the following repository https://gitlab.ebrains.eu/fousekjan/vab-sleep.

Results

The virtual aging brain model replicates the age-related changes of sleep slow waves

Simulated SW characteristics along the virtual aging trajectory (reduction in inter-hemispheric connections) show the same trends of changes as the reported empirical observations. In particular, with age, the frequency of the SW decreases (Fig. 2*a*), the coefficient of variation increases (Fig. 2*d*), and the amplitude of the SW decreases (Fig. 2*e*). The shape of the SW also changes, namely the down-states become longer with age (Fig. 2*c*) while up-states remain almost unchanged (Fig. 2*b*). All panels of Figure 2 show the variability of the average channel characteristics of the SW across 16 different realizations of the stochastic process. We refer to Extended Data Figure 2-1 for the parameter differences assessed with Kruskal–Wallis for each degradation level α.

To simulate other reported effects of the aging process (Coelho et al., 2021; Petkoski et al., 2023), particularly affecting the fronto-parietal connections, the left fronto-parietal connections (Extended Data Fig. 3-3, lobes defined by FSL MNI atlas Collins et al., 1995) were reduced similarly as described in Section 3.1, with the degree of connectome degradation represented by the parameter $\beta \in [0.1, 0.6]$. The results, reported in the Extended Data Figure 3-2, well align with those in Figure 3, showing that the additional decrease in connectivity further amplifies the effects observed after the reduction of inter-hemispheric connections.

Network changes have spatially differential impact

The computational model provides access to the activity on the level of individual nodes in addition to the simulated EEG. There, the age-related trends of the main characteristics of the EEG slow oscillations described in the previous

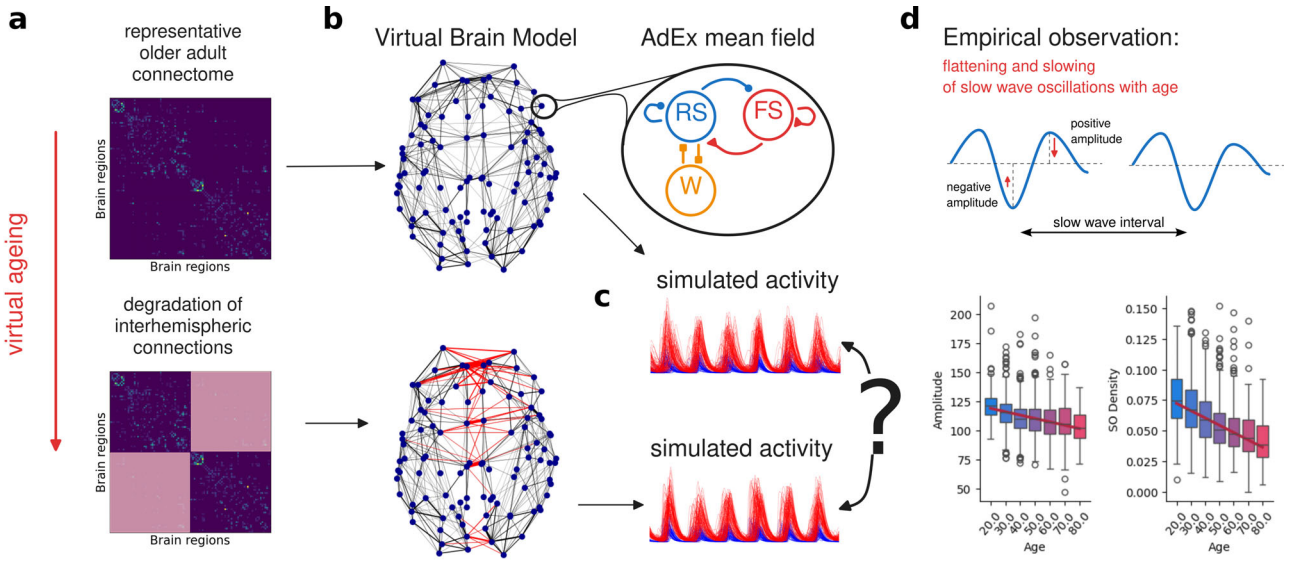

Figure 1. Overview of the approach. ***a***, The age-related deterioration of the interhemispheric connections is captured as a gradual decrease in the respective elements in the structural connectivity (SC) matrix representative of an older adult. ***b***, Virtual Brain model is constructed from the SCs along the virtual aging trajectory using the AdEx mean field model to govern the nodes' dynamics. ***c***, The brain network model is used to simulate the sleep-like activity both on the source-level and on the EEG sensors, which is then compared across the virtual aging trajectory and against the empirical data with respect to the selected data features. ***d***, Empirical observations of interest (El Kanbi et al., 2023): flattening of the slow oscillations (decrease in amplitude) and decrease in density (fewer SO per time unit).

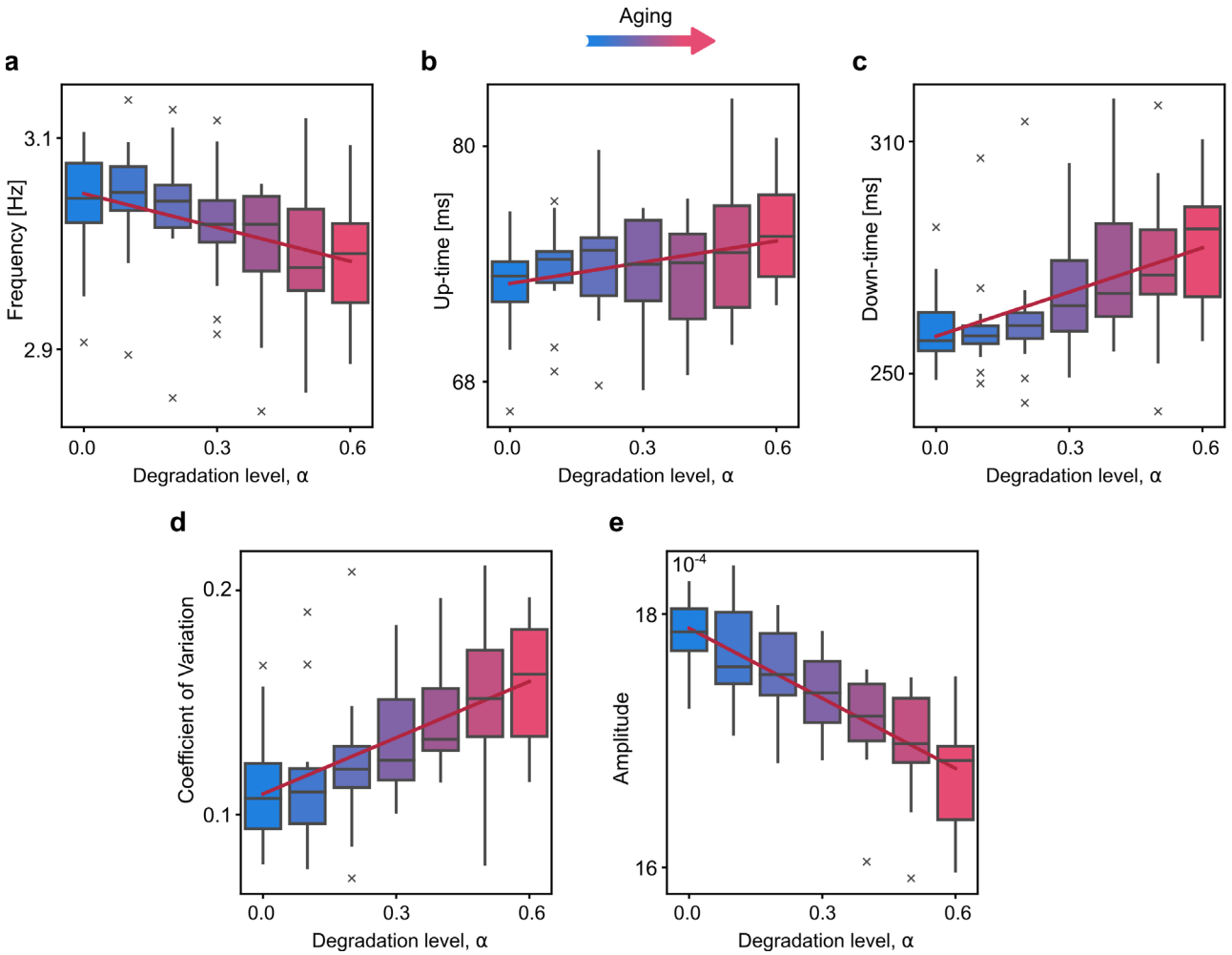

Figure 2. Slow oscillation (SO) changes along the virtual aging trajectory in the simulated EEG data. A value of 50 ms is taken for the spike temporal length and 0.5 for the amplitude threshold. The boxplots represent the variability of the average network characteristics for 16 different realizations of the OU process. The following effects are observed: Decrease in SO frequency ***a***, Slight increase in up-state duration ***b***, Increase in down-state duration ***c***, Increase in coefficient of variation (CV) of the SO ***d***, Decrease in amplitude of the SO ***e***, Extended Data Figure 2-1 provides the statistical evaluation of the differences. Extended Data Figure 2-2 details the robustness of the results with respect to the choice of the up-state threshold. Extended Data Figure 2-3 shows the position of the EEG electrodes.

section were preserved when averaged over the nodes of the network: the frequency decreased (Fig. 3*a*) and the coefficient of variability increased (Fig. 3*d*). In agreement with the spiking neural network (El Kanbi et al., 2023), the duration of the down state increased while the duration of the up state slightly decreased (Fig. 3*b*,*c*). At a node-specific level, instead, different nodes exhibited different rates of change of the SW characteristics along the virtual aging trajectory (Fig. 3*e*–*h*). When evaluating the linear relationship between nodal SW characteristics and alterations in graph properties of the SC along the virtual aging trajectory (Fig. 4 and Extended Data Fig. 4-1), we observed a reduction in nodal frequency and up-time duration with diminishing nodal strengths, and an increase in nodal down-time and CV with reducing nodal strengths. Lastly, we explored whether there was a change across the aging trajectory in terms of initiation of the individual slow waves–that is which nodes arrive first to the up-state within the synchronous wave. While certain nodes initiated the slow wave more frequently than others, this didn't change significantly across the ageing trajectory (Extended Data Figs. 4-2 and 4-3).

Decrease in EEG amplitude reflects decrease in inter-region synchrony

The decrease in amplitude is observed both in the empirical EEG data (El Kanbi et al., 2023; Fig. 1*d*) and in our simulated EEG data (Fig. 2*e*). However, no such decrease was observed on the network level. In order to explain this discrepancy, we turned to synchrony on the network level as the desynchronized oscillations would translate to smaller amplitudes on the EEG level due to linear mixing of the network-level signals through the leadfield matrix (Section 3.3.1). Indeed, the synchrony between the nodes, quantified by the PLVs, decreased as a function of increased virtual aging (Fig. 5*a*) for both

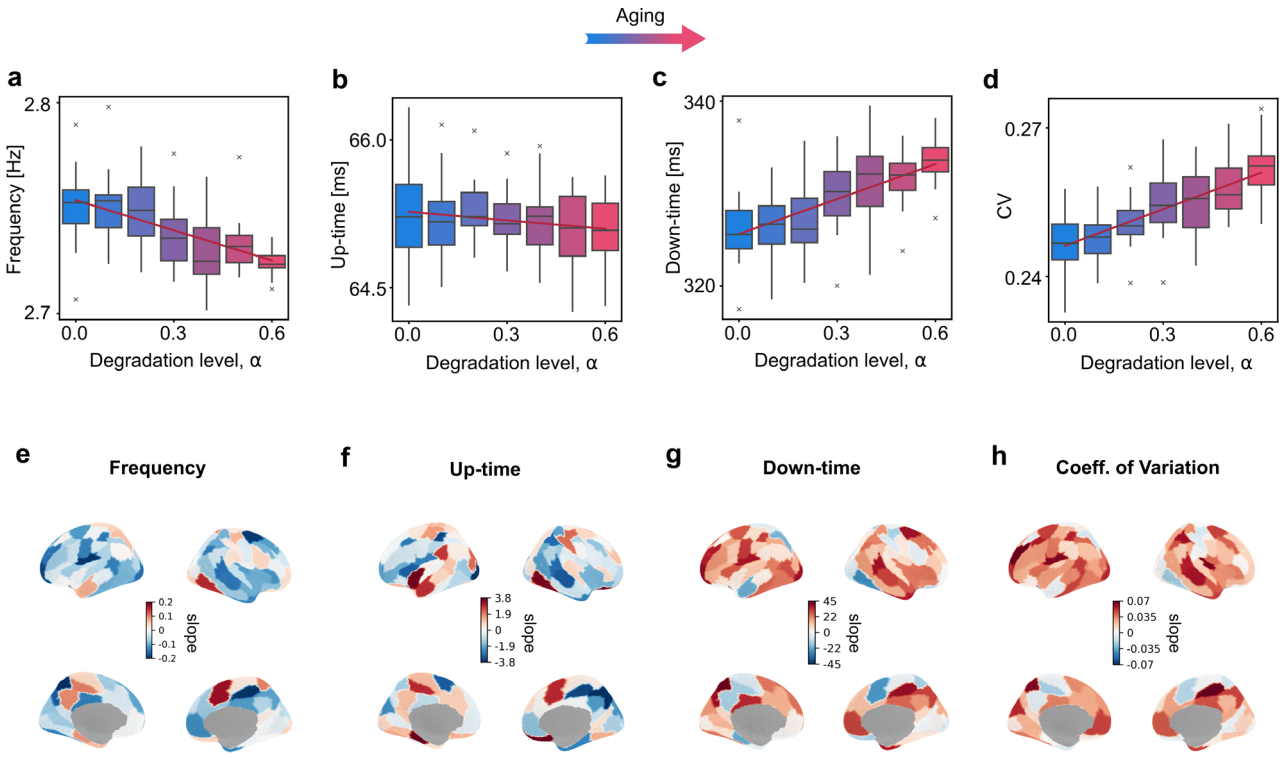

Figure 3. Relationship between degradation level (increasing synthetic aging) and slow wave oscillation characteristics across all nodes (first row) and at a single-node level (second row) for frequencies ***a, e***, (Freq.) average up–***b, f***, and down-state duration ***c, g***, and coefficient of variation ***d, h***, (CV). In the first row ***a-d***, each box-and-whisker plot represents the distribution of the considered value (e.g., frequency) across 16 realizations of noise averaged over all nodes, obtained for each single weight used to scale the structural connectivity matrix on 30 s simulations. The red line in each graph represents the linear fit across the mean values for each synthetic age (e.g., each weight). The second row ***e-h***, shows a brain surface—for the 100 regions of the Schaefer atlas—colored proportionally to the slopes of change of each single node, showing if the considered value (e.g., Frequency) increases (positive values) or decreases (negative values) along the synthetic aging process for that node. Extended Data Figure 3-1 details the robustness of the results with respect to the choice of the up-state threshold. Extended Data Figure 3-2 shows the complementary effect of the additional deterioration of the fronto-parietal tracts. Extended Data Figure 3-3 shows the location of the frontal and parietal areas.

excitatory and inhibitory neural populations. Moreover, this decrease was driven by the decrease of synchrony between inter-hemispheric pairs of nodes (Fig. 5*b*,*c*).

Discussion

In this study, we aimed to investigate whether alterations in SW characteristics observed with aging derive from a reduction in nodal excitatory drives due to diminished inter-hemispheric connectivity. To assess this, we simulated SW oscillations by using a mean field whole-brain network model of sleep-like activity (AdEx) (Zerlaut et al., 2018; Di Volo et al., 2019; Goldman et al., 2022), where nodal activities were coupled by an underlying structural connectivity matrix. We employed the "virtual-aging" framework (Lavanga et al., 2023a), and, starting from a representative structural connectome (at the beginning of the aging trajectory), we synthetically reduced only the inter-hemispheric connections to simulate aging.

First, we were able to qualitatively reproduce, in our simulations, the age-related changes in SW characteristics observed in real empirical EEG recordings (El Kanbi et al., 2023). Notably, the simulated SW successfully mirrored the decreased SW frequency and duration of Up-states, increased variability and prolonged duration of Down-states observed at the EEG-level with aging (Van Cauter et al., 2000; Landolt and Borbély, 2001; El Kanbi et al., 2023). Similar effects were observed for slow-waves in an early-aging model in mice (Castano-Prat et al., 2017). Inter-hemispheric connections are well-known to decrease with aging (Puxeddu et al., 2020; Lavanga et al., 2023a) and our results align with previous literature showing their importance in influencing both awake resting state activity (Lavanga et al., 2023a) and sleep SW characteristics (Avvenuti et al., 2020). Previous work has hypothesized that a reduction in the neural cortical excitatory drive underlies many of the SW alterations observed with aging (Castano-Prat et al., 2017; El Kanbi et al., 2023). In particular, both electrophysiological findings on a mouse model of aging (Castano-Prat et al., 2017) and simulations from a computational model (El Kanbi et al., 2023) suggested that slower speed of propagation and diminished frequency of SW were linked to reduced cortical excitability. Here, by characterizing inter-hemispheric connections as

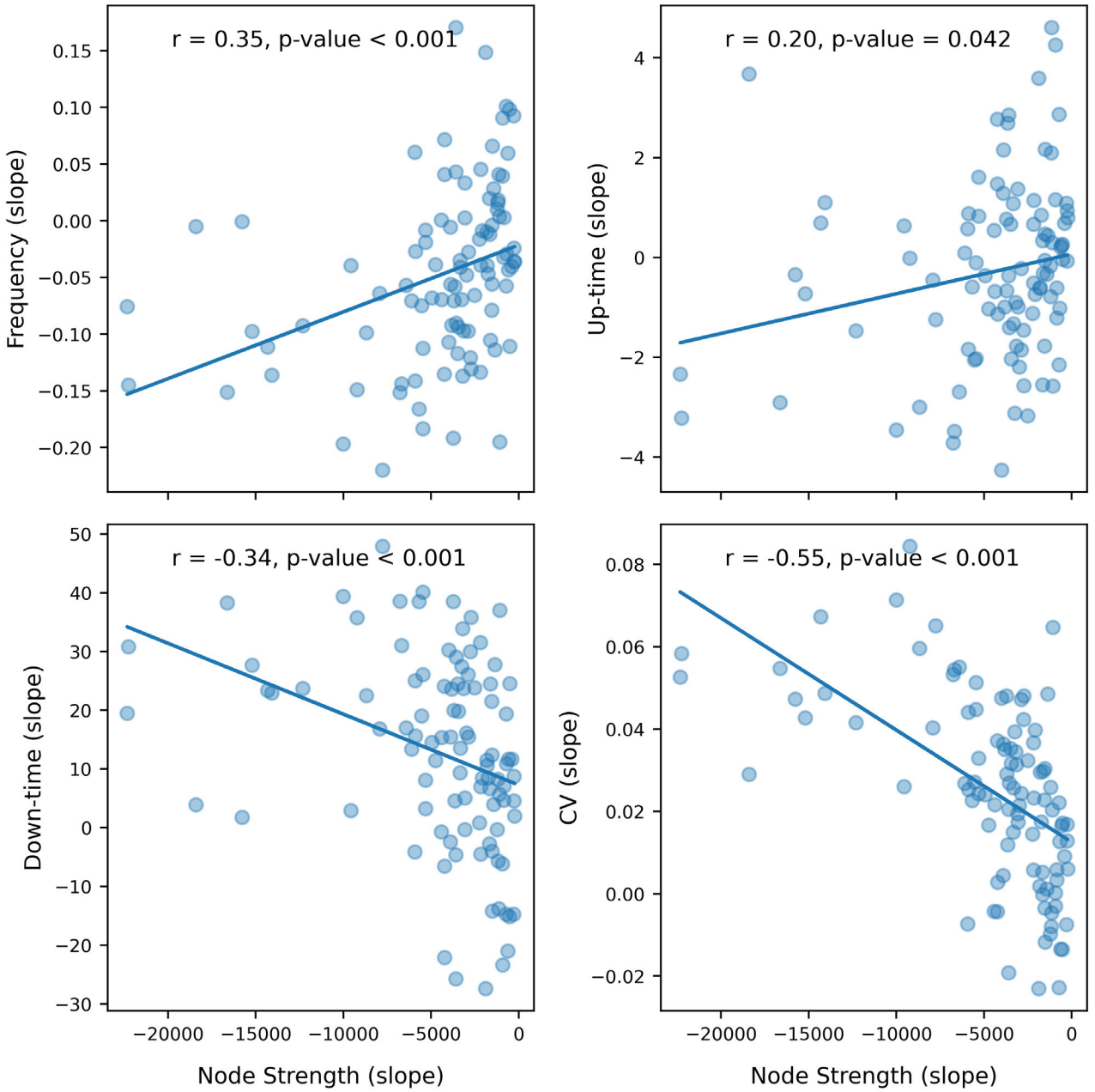

Figure 4. Regional association between rates of change (slope) in SW features and rates of change (slope) in graph theory metrics–node strength–across different levels of synthetic aging for each node of the 100-Schaefer atlas. The slope in all cases is the rate of change of the given metric over the levels of synthetic aging. Each point represents an average value across different noise realizations. Extended Figure 4-1 shows the rate of change of the SW features with respect to eigenvector centrality. Extended Figure 4-2 provides an overview of which nodes initiate the slow waves across the ageing trajectory. Extended Figure 4-3 shows the summary statistic for the SW initiation.

only excitatory, we were able to provide evidence for the network origin of this reduced excitatory drive. In fact, diminishing inter-hemispheric connections in the model is equivalent to a reduction in the external excitatory drive for each connected node. Even though the nodes of the network were identical in their mean field model parameters, the effect of the reduced interhemispheric connections was spatially heterogeneous. Such heterogeneous age-related changes in structure-function coupling have been previously reported in awake fMRI data (Zamani Esfahlani et al., 2022), and together with our results suggest an intriguing direction for future empirical cohort studies of sleep EEG data. Given that previous studies have reported that the effects of aging also include the reduction of certain specific intra-hemispheric connections, we also investigated changes in slow-wave characteristics by selectively reducing the left fronto-parietal connections (Coelho et al., 2021; Petkoski et al., 2023). By applying the same “virtual aging” procedure, we showed that these alterations only strengthen the observed effects determined by the reductions in inter-hemispheric connections.

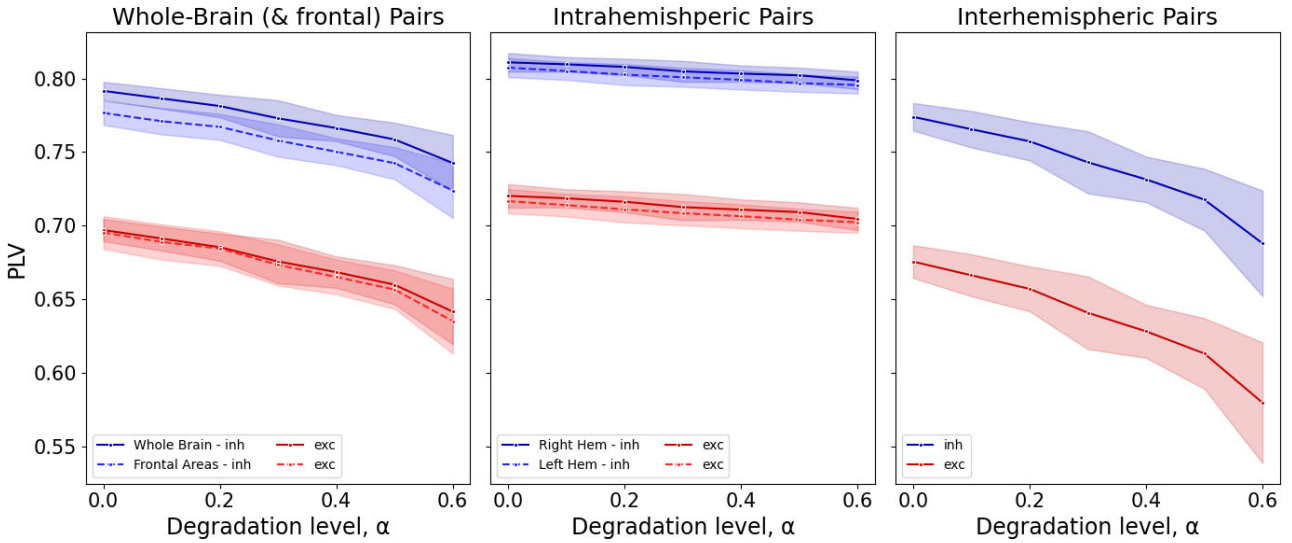

Figure 5. Mean PLVs, averaged over all trials (n = 15), as a metric for phase synchronization between the different nodes. Increasing degradation level denote virtual aging, which is characterized by a decrease in synchrony. The observed decrease of synchrony in the level of whole-brain ***a***, is driven by a decrease in the interhemispheric synchrony ***c***, as a minimal effect is detected in the synchrony within the same hemisphere ***b***. The frontal areas (*a*—dotted line) reflect the same tendency in synchrony as the whole brain. Extended Figure 5-1 shows the selected frontal areas and their connections. Extended Figure 5-2 shows an example time-course of the SW dynamics.

In empirical data, aging is also consistently linked with a decline in EEG amplitude (El Kanbi et al., 2023), suggesting a potential reduction in synchrony among brain regions. Notably, our virtual aging simulations revealed a more pronounced reduction in inter-hemispheric synchrony compared to intra-hemispheric synchrony. We thus suggest that reduced inter-hemispheric structural connections might also yield reduced inter-hemispheric synchrony and reduced EEG amplitude. SW are commonly conceptualized as traveling waves (Massimini et al., 2004), with propagation mainly via cortico-cortical white matter connections. Our results align with previous studies that demonstrated a direct association between parameters reflecting slow-wave synchronization and the microstructure (Buchmann et al., 2011; Piantoni et al., 2013) and structural integrity (Avvenuti et al., 2020) of the corpus callosum. In this view, inter-hemispheric connections likely serve as the primary pathway for cross-hemispheric propagation of slow waves (Avvenuti et al., 2020). Furthermore, the loss of slow-wave synchrony may further impact the high-frequency activity related to plastic processes such as memory consolidation, which is modulated by the slow-wave activity and potentially relying on the synchronous slow-waves for efficient inter-area communication (Helfrich et al., 2018; Staresina et al., 2023).

It should be noted that our simulations were performed only on one representative connectome, drawn from the embedding of connectomes of adults aged 55–63, that was "virtually aged." Thus, future studies could aim at extending our results to empirical cohorts in order to address the inter-individual variability. In particular, virtual brain models with model parameters personalized with respect to individual EEG data would allow for relating the structural and functional changes to the decline in cognitive performance and other factors (Lavanga et al., 2023a). While the starting point of the virtual aging trajectory falls into the middle-aged adult bracket, it reflects the starting point of both the white matter changes (Schilling et al., 2022), and changes in the slow wave characteristics of the sleep (Mander et al., 2017; El Kanbi et al., 2023).

Furthermore, in this study, we only focused on inter-hemispheric connectivity, thus we cannot exclude that other factors known to be associated with aging (e.g., age-related neuromodulatory changes or grey matter atrophy) might also play a role in shaping SW characteristics. In particular, the role of aging-associated cholinergic reduction (Muir, 1997), which can be modeled as a variation of the adaptation parameter of the AdEx model (Brette and Gerstner, 2005; Zerlaut et al., 2018), should be further explored in future studies. While the local and network contributions to the reduced excitatory drive are difficult to disentangle, the respective hypotheses can be implemented in the virtual model of the mouse brain and augment the interpretation of the data on age-related changes of the slow wave characteristics of brain activity in animal models of aging (Melozzi et al., 2017; Sacha et al., 2024), including interventional studies (Spiegler et al., 2020).

The understanding of the age-related changes in sleep is important also due to sleep being implied as an intervention target in the neurodegenerative diseases (Tatulian, 2022). In fact, the disease can accelerate the age-related changes of the sleep processes reflected in the EEG features, such as the decrease in amplitude of the slow wave power (for review see Romanella et al., 2021). Moreover, the mechanistic models have recently provided explanations of the characteristic frequency slowing of the spontaneous awake brain activity in terms of local changes of the neural mass parameters due to the neurotoxicity (Alexandersen et al., 2023; Cabrera-Àlvarez et al., 2024). Integrating these models with the model of the aging sleep brain state presented in this paper constitutes an intriguing area of future work.

Conclusion

In conclusion, our study sheds light on the potential role of inter-hemispheric connectivity in shaping age-related changes in SW sleep. By bridging the gap between mechanistic modeling and empirical observations, our findings pave the way for further research aimed at understanding and improving sleep quality in the aging population.

References

Abbott LF, van Vreeswijk C (1993) Asynchronous states in networks of pulse-coupled oscillators. Phys Rev E 48:1483–1490.

Alexandersen CG, de Haan W, Bick C, Goriely A (2023) A multi-scale model explains oscillatory slowing and neuronal hyperactivity in Alzheimer's disease. J R Soc Interface 20:20220607.

Antonenko D, Flöel A (2014) Healthy aging by staying selectively connected: a mini-review. Gerontology 60:3–9.

Arnal PJ, et al. (2020) The dreem headband compared to polysomnography for electroencephalographic signal acquisition and sleep staging. Sleep 43:zsaa097.

Avvenuti G, et al. (2020) Integrity of corpus callosum is essential for the cross-hemispheric propagation of sleep slow waves: a high-density EEG study in split-brain patients. J Neurosci 40:5589–5603.

Bethlehem RAI, et al. (2022) Brain charts for the human lifespan. Nature 604:525–533.

Brette R, Gerstner W (2005) Adaptive exponential integrate-and-fire model as an effective description of neuronal activity. J Neurophysiol 94:3637–3642.

Brunel N, Hakim V (1999) Fast global oscillations in networks of integrate-and-fire neurons with low firing rates. Neural Comput 11:1621–71.

Buchmann A, Kurth S, Ringli M, Geiger A, Jenni OG, Huber R (2011) Anatomical markers of sleep slow wave activity derived from structural magnetic resonance images. J Sleep Res 20:506–513.

Cabrera-Àlvarez J, Stefanovski L, Martin L, Susi G, Maestú F, Ritter P (2024) A multiscale closed-loop neurotoxicity model of Alzheimer's disease progression explains functional connectivity alterations. eNeuro 11:ENEURO.0345–23.2023.

Carrier J, Viens I, Poirier G, Robillard R, Lafortune M, Vandewalle G, Martin N, Barakat M, Paquet J, Filipini D (2011) Sleep slow wave changes during the middle years of life. Eur J Neurosci 33:758–766.

Caspers S, et al. (2014) Studying variability in human brain aging in a population-based German cohort—rationale and design of 1000brains. Front Aging Neurosci 6:00149.

Caspers S, Schreiber J (2021) 1000brains study, connectivity data (v1.1).

Castano-Prat P, Perez-Zabalza M, Perez-Mendez L, Escorihuela RM, Sanchez-Vives MV (2017) Slow and fast neocortical oscillations in the senescence-accelerated mouse model SAMP8. Front Aging Neurosci 9:141.

Coelho A, et al. (2021) Signatures of white-matter microstructure degradation during aging and its association with cognitive status. Sci Rep 11:4517.

Collins DL, Holmes CJ, Peters TM, Evans AC (1995) Automatic 3-d model-based neuroanatomical segmentation. Hum Brain Mapp 3:190–208.

Damoiseaux JS (2017) Effects of aging on functional and structural brain connectivity. NeuroImage 160:32–40.

Debellemaniere E, Chambon S, Pinaud C, Thorey V, Dehaene D, Léger D, Chennaoui M, Arnal PJ, Galtier MN (2018) Performance of an ambulatory dry-EEG device for auditory closed-loop stimulation of sleep slow oscillations in the home environment. Front Hum Neurosci 12:88.

Deco G, Corbetta M (2011) The dynamical balance of the brain at rest. Neurosci: Rev J Bringing Neurobiol Neurol Psychiatry 17:107–123.

Di Volo M, Romagnoni A, Capone C, Destexhe A (2019) Biologically realistic mean-field models of conductance-based networks of spiking neurons with adaptation. Neural Comput 31:653–680.

Dubé J, Lafortune M, Bedetti C, Bouchard M, Gagnon JF, Doyon J, Evans AC, Lina J-M, Carrier J (2015) Cortical thinning explains changes in sleep slow waves during adulthood. J Neurosci 35:7795–7807.

El Kanbi K, Tort-Colet N, Benchenane K, Destexhe A (2023) "Eeg and computational aspects of how aging affects sleep slow waves." *bioRxiv*.

Ghosh A, Rho Y, McIntosh AR, Kötter R, Jirsa VK (2008) Noise during rest enables the exploration of the brain's dynamic repertoire. PLOS Comput Biol 4:e1000196.

Ghuman AS, McDaniel JR, Martin A (2011) A wavelet-based method for measuring the oscillatory dynamics of resting-state functional connectivity in meg. Neuroimage 56:69–77.

Giorgio A, Santelli L, Tomassini V, Bosnell R, Smith S, De Stefano N, Johansen-Berg H (2010) Age-related changes in grey and white matter structure throughout adulthood. Neuroimage 51:943–951.

Goldman JS, Kusch L, Aquilue D, Yalçınkaya BH, Depannemaecker D, Ancourt K, Nghiem T -AE, Jirsa V, Destexhe A (2022) A comprehensive neural simulation of slow-wave sleep and highly responsive wakefulness dynamics. Front Comput Neurosci 16:1058957.

Helfrich RF, Mander BA, Jagust WJ, Knight RT, Walker MP (2018) Old brains come uncoupled in sleep: slow wave-spindle synchrony, brain atrophy, and forgetting. Neuron 97:221–230.e4.

Knight BW (2000) Dynamics of encoding in neuron populations: some general mathematical features. Neural Comput 12:473–518.

Lachaux J-P, Rodriguez E, Martinerie J, Varela FJ (1999) Measuring phase synchrony in brain signals. Hum Brain Mapp 8:194–208.

Landolt HP, Borbély AA (2001) Age-dependent changes in sleep EEG topography. Clin Neurophysiol: Off J Int Fed Clin Neurophysiol 112:369–377.

Lavanga M, et al. (2023a) The virtual aging brain: causal inference supports interhemispheric dedifferentiation in healthy aging. NeuroImage 283:120403.

Lavanga M, et al. (2023b) The virtual aging brain (v1.0.0).

Mander BA, Winer JR, Walker MP (2017) Sleep and human aging. Neuron 94:19–36.

Massimini M, Huber RR, Ferrarelli F, Hill S, Tononi G (2004) The sleep slow oscillation as a traveling wave. J Neurosci 24:6862.

Mattia M, Del Giudice P (2002) Population dynamics of interacting spiking neurons. Phys Rev E 66:051917.

Melozzi F, Woodman MM, Jirsa VK, Bernard C (2017) The virtual mouse brain: a computational neuroinformatics platform to study whole mouse brain dynamics. eNeuro 4:ENEURO.0111-17.2017.

Muir JL (1997) Acetylcholine, aging, and Alzheimer's disease. Pharmacol Biochem Behav 56:687–696.

Petkoski S, Ritter P, Jirsa VK (2023) White-matter degradation and dynamical compensation support age-related functional alterations in human brain. Cereb Cortex 33:6241–6256.

Piantoni G, Poil S-S, Linkenkaer-Hansen K, Verweij IM, Ramautar JR, Van Someren EJW, Van Der Werf YD (2013) Individual differences in white matter diffusion affect sleep oscillations. J Neurosci: Off J Soc Neurosci 33:227–233.

Puxeddu MG, Faskowitz J, Betzel RF, Petti M, Astolfi L, Sporns O (2020) The modular organization of brain cortical connectivity across the human lifespan. NeuroImage 218:116974.

Romanella SM, Roe D, Tatti E, Cappon D, Paciorek R, Testani E, Rossi A, Rossi S, Santarnecchi E (2021) The sleep side of aging and Alzheimer's disease. Sleep Med 77:209–225.

Sacha M, Goldman JS, Kusch L, Destexhe A (2024) Asynchronous and slow-wave oscillatory states in connectome-based models of mouse, monkey and human cerebral cortex. Appl Sci (Basel) 14:1063.

Sanz-Leon P, Knock SA, Spiegler A, Jirsa VK (2015) Mathematical framework for large-scale brain network modeling in the virtual brain. NeuroImage 111:385–430.

Sarvas J (1987) Basic mathematical and electromagnetic concepts of the biomagnetic inverse problem. Phys Med Biol 32:11.

Schaefer A, Kong R, Gordon EM, Laumann TO, Zuo X-N, Holmes AJ, Eickhoff SB, Yeo BTT (2018) Local-global parcellation of the human cerebral cortex from intrinsic functional connectivity MRI. Cereb Cortex 28:3095–3114.

Schilling KG, et al. (2022) Aging and white matter microstructure and macrostructure: a longitudinal multi-site diffusion MRI study of 1218 participants. Brain Struct Funct 227:2111–2125.

Schirner M, et al. (2022) Brain simulation as a cloud service: the virtual brain on EBRAINS. NeuroImage 251:118973.

Spiegler A, Abadchi JK, Mohajerani M, Jirsa VK (2020) In silico exploration of mouse brain dynamics by focal stimulation reflects the organization of functional networks and sensory processing. Netw Neurosci 4:807–851.

Stam CJ, Nolte G, Daffertshofer A (2007) Phase lag index: assessment of functional connectivity from multi channel EEG and MEG with diminished bias from common sources. Hum Brain Mapp 28:1178–1193.

Staresina BP, Niediek J, Borger V, Surges R, Mormann F (2023) How coupled slow oscillations, spindles and ripples coordinate neuronal processing and communication during human sleep. Nat Neurosci 26:1429–1437.

Steriade M, Nunez A, Amzica F (1993) A novel slow (<1 hz) oscillation of neocortical neurons in vivo: depolarizing and hyperpolarizing components. J Neurosci: Off J Soc Neurosci 13:3252–3265.

Tatulian SA (2022) Challenges and hopes for Alzheimer's disease. Drug Discov Today 27:1027–1043.

Treves A (1993) Mean-field analysis of neuronal spike dynamics. Network 4:259–84.

Van Cauter E, Leproult R, Plat L (2000) Age-related changes in slow wave sleep and REM sleep and relationship with growth hormone and cortisol levels in healthy men. JAMA 284:861–868.

Zamani Esfahlani F, Faskowitz J, Slack J, Mišić B, Betzel RF (2022) Local structure-function relationships in human brain networks across the lifespan. Nat Commun 13:2053.

Zerlaut Y, Chemla S, Chavane F, Destexhe A (2018) Modeling mesoscopic cortical dynamics using a mean-field model of conductance-based networks of adaptive exponential integrate-and-fire neurons. J Comput Neurosci 44:45–61.

4. Discussion with references

In this thesis I contribute to advancing neuroimaging-based brain network models for neurodegenerative diseases in two main ways. First, my results increase our understanding of the multifactorial nature of AD, the most common neurodegenerative disease, particularly regarding CSVD co-pathologies. In a genetic ADAD cohort, I showed that PVS alterations may be intrinsic to AD pathogenesis. Additionally, in aging-associated AD I found that WMH are linked to cortical thinning in AD-vulnerable temporal regions - further supporting the idea that CSVD is an integral part of AD pathology. Second, my findings contribute to building more biologically informed brain network models allowing for a more detailed investigation into how CSVD and WM damage affect brain dynamics in wakefulness and sleep. Using these models, I found that the global burden of WMH affect wakeful resting-state activity in early AD by reducing the global coupling of brain regions (e.g., their synchrony). Additionally, reductions in inter-hemispheric WM connections are responsible for sleep slow-wave activity changes commonly observed in aging and AD.

4.1 CSVD contributes to AD pathogenesis

My first two projects investigated the role of CSVD in AD. These results challenge the conventional view of CSVD as only a secondary, age-related co-pathology in late-onset AD. They further suggest the importance of considering CSVD and the related WM damage to fully account for the pathophysiological complexity of AD.

Since CSVD is usually associated with confounders, such as aging and cardiovascular risk factors, in Project 1 (Leone et al., 2025), I focused on individuals with a genetic form of AD, which typically manifests between ages 30 and 50. Here, I investigated PVS alterations as a biomarker of CSVD. A novel, fully automated MRI method (Barisano et al., 2025), allowed us to quantify PVS metrics, in terms of count and mean diameter, across the whole brain. This approach overcame the limitations of traditional, manually rated scales of PVS restricted to a single MRI slice. In this project, I found that mutation carriers had fewer but enlarged PVS compared to non-carrier relatives, with changes emerging

up to 18 years before dementia onset. Given that PVS visibility on MRI reflects normal perivascular fluid flow, reduced visibility may indicate small vessel dysfunction. This is consistent with prior findings of CSVD in post-mortem ADAD cases (Littau et al., 2022), reduced cerebral blood flow in ADAD (McDade et al., 2014), and recent studies reporting lower PVS volume in individuals with mild cognitive impairment and in subjects at-risk for dementia in late-onset AD (Barisano et al., 2025). While PVS count was reduced earlier, enlargement occurred a few years later. I speculate that this suggests a two-phase process where initial small vessel dysfunction alters perivascular fluid dynamics, later leading to a compensatory enlargement of still patent PVS. When comparing the trajectories of PVS alterations along the disease course with those of established biomarkers such as cerebrospinal fluid (CSF) Aβ and tau, I observed a temporal overlap. Both PVS metrics and CSF biomarkers exhibited increasingly abnormal values closer to the onset of dementia, potentially suggesting that changes in PVS occur in a similar time frame as classical AD pathology. Similarly, when I assessed the regional distribution of PVS alterations, I observed a spatial overlap with common sites of pathology in ADAD, such as the basal ganglia and temporal lobe (Bateman et al., 2012). These findings reinforce the hypothesis that PVS alterations are linked to AD-specific mechanisms. These results are in line with previous findings on WMH in ADAD, where mutation carriers had greater WMH volume, increasing approximately 6 years before expected symptom onset (Lee et al., 2016; Schoemaker et al., 2022). A limitation of this study was that amyloid and tau CSF and PET data were not available for our cohort, so we could only compare the temporal and spatial distribution of PVS alterations with a reference cohort (Bateman et al., 2012). Although the accumulation of amyloid and tau in ADAD is more stereotypical than late-onset AD (Bateman et al., 2012), future studies should aim to directly compare PVS alterations with amyloid and tau CSF and PET data within the same cohort. Overall, these results suggest an intrinsic involvement of small brain vessels and their surrounding PVS in the pathophysiology of ADAD.

Having provided evidence for a direct link between CSVD and AD pathology in a cohort without confounders, in Project 2 (Leone & Kobeleva, 2025), I further analyzed the effects of CSVD on early neurodegeneration in late-onset, sporadic, AD. In this study, I tested whether WMH were associated with cortical thinning in AD-vulnerable temporal regions (Jack et al., 2015) in addition to amyloid and tau, and whether global (cerebrovascular disease) or focal (axonal degeneration) processes explained this association. To estimate axonal degeneration, I used a disconnectome approach (Griffis et al., 2021). By evaluating the location of WMH within the brain and by combining it with a reference tractography atlas, this approach allowed me to trace the focal burden of WMH both to the specific WM tracts affected and to the cortical regions connected to those tracts. This study demonstrated that the global burden of WMH, namely the total volume of WMH, is linked with cortical thinning in AD-vulnerable regions of the temporal lobe, also when correcting for regional tau and amyloid deposition. The global burden of WMH explained a substantial proportion of variance in cortical thickness, exceeding that of amyloid. Periventricular WMH showed the strongest associations with reduced cortical thickness in AD-vulnerable temporal regions. The associations between WMH and cortical thinning were generally stronger in amyloid-positive individuals and were largely confined to AD-vulnerable temporal regions, with no strong associations observed in other brain regions. These findings align with recent evidence that vascular pathology may contribute to AD-related atrophy beyond classical AD mechanisms, for example via hypoxic damage or blood-brain-barrier dysfunction (Barisano et al., 2022). The absence of associations between the focal burden of WMH and cortical thinning suggests that diffuse processes, rather than axonal degeneration, may drive early WMH-related neurodegeneration. However, this could differ from later stages of the disease, since WMH-connected regions have lower cortical thickness compared to WMH-unconnected regions in later dementia stages (J. Zhang et al., 2024). In this study, I did not find any longitudinal associations between WMH and cortical thinning, possibly due to the relatively short follow-up or dominant tau-related degeneration. It is worth noting that this study used a population-based reference tractography atlas to quantify the focal burden of WMH. This choice was

performed to reduce false positive WM connections that are often observed in single-subject diffusion tractography. However, this prevented the assessment of WM tract variability between individuals. Therefore, future studies using individual subjects' tractography data will be crucial to further confirm our findings and to fully clarify the mechanisms linking WMH and neurodegeneration in AD. Overall, the findings of this study further highlight the role of CSVD in shaping structural brain changes in AD, setting the stage for exploring how such pathology influence brain dynamics during wakefulness and sleep.

4.2 White matter co-pathologies influence brain dynamics during wakefulness and sleep

Results from the previous projects set the stage to evaluate the effects of CSVD-related WM damage, such as WMH, on brain network activity. In Project 3 (Leone et al., 2024), I developed a brain network model and combined it with a disconnectome (Griffis et al., 2021) approach to study the pathological effects of WMH on brain dynamics. As in Project 2, the disconnectome framework enabled me to map focal WMH-related damage both to the affected WM tracts and to the cortical regions connected to those tracts. Incorporating this information into the brain network model allowed me to simulate the resulting alterations in brain dynamics, thereby providing a "mechanistic" link between WM damage and its functional consequences. In line with the approach used in Project 2, here I again investigated whether the impact of WMH on brain dynamics depended on global versus focal effects. In this study, I showed that the pathological effects of WMH are linked to WMH-associated reductions in global coupling, leading to diminished overall synchronization of the brain. Alterations of local regional dynamics through disconnections are less relevant and present only at higher stages of WMH damage. Exploratory analyses suggested that education might play a beneficial role in counteracting the reduction in global coupling associated with WMH. Previous associational studies on the effects of WMH on inter-regional functional connectivity are mixed (Schulz et al., 2021), but results from my study are in line with the prevailing idea that WMH mostly reduce long-distance functional connectivity (Quandt et al., 2020). The association with global rather than focal

damage further supports the hypothesis that CSVD induces widespread damage to WM tracts. This damage, although not directly observable with structural MRI, could already impair brain communication in widespread networks (Ter Telgte et al., 2018). Future studies could incorporate more advanced diffusion tensor imaging metrics, such as fractional anisotropy, in brain network models. These metrics may already be altered within the normal appearing white matter, possibly providing an additional characterization of the effects of CSVD-related damage on brain function. Overall, this study bridged the structural and functional alterations observed in subjects with WMH using a biophysical ("mechanistic") brain network model. These results provide a needed foundation for future work aiming to build more biologically realistic brain network models in AD by combining the effects of WMH with those of amyloid and tau.

In Project 4 (Lupi et al., 2024), I contributed to a study investigating how inter-hemispheric WM damage, a common feature of both aging and AD, exacerbated by CSVD, impacts the dynamics of SWS. We initially developed a brain network model using a reference structural connectome of middle-aged adults. Then, we simulated a progressive reduction of inter-hemispheric WM connections ("virtual aging"), mimicking the evolution of structural disconnections observed in empirical aging (Lavanga et al., 2023). Our model demonstrated that this loss of structural connectivity alone induced characteristic alterations in SWS, namely a reduction in slow-wave frequency and amplitude, alongside increased temporal variability. These simulated outcomes not only recapitulate the well-documented changes to SWS observed in aging (Kanbi et al., 2023) but also mirror the SWS disturbances that are hallmarks of AD (Zhang et al., 2022). Although our study was based on theoretical simulations, it provides a powerful mechanistic hypothesis: that the integrity of inter-hemispheric WM tracts is critical for sustaining the cortical synchrony necessary for normal SWS. This suggests that WM damage, as a common underlying pathology, could be a direct driver of the SWS disruptions seen in both aging and AD. Understanding this link is clinically significant, as impaired SWS may in turn accelerate neurodegeneration by hindering processes like metabolic waste clearance along PVS (Tatulian, 2022). It is worth noting that

this work relied on a “virtual aging” model rather than empirical data. Future studies, possibly in a longitudinal setting, should combine empirical structural connectivity data of the aging brain with electrophysiological sleep recordings to properly validate our synthetic findings in vivo. Nevertheless, the findings of this study provide crucial information that build a strong foundation to investigate the combined effects of WM damage, amyloid, and tau pathologies on sleep architecture in aging and AD.

4.3 Conclusion

In conclusion, this work deepens our understanding of how WM co-pathologies, such as CSVD, affect brain structure and function in AD. Moreover, by incorporating this information into brain network models, it brings them closer to biologically realistic representations that better capture the full complexity of the disease. More biologically realistic models may support earlier and more precise detection of subtle brain functional alterations in AD and other neurodegenerative diseases. Additionally, by simulating how an individual’s brain responds to specific interventions, such as drugs or stimulation, brain network models have the potential to help tailor treatments to each patient’s unique brain activity profile. These advancements may enable interventions to be applied at earlier disease stages and more effectively, ultimately improving patient care and outcomes.

4.4 References

Barisano, G., Iv, M., Choupan, J., Hayden-Gephart, M., Weiner, M., Aisen, P., Petersen, R., Jack, C. R., Jagust, W., Trojanowki, J. Q., Toga, A. W., Beckett, L., Green, R. C., Saykin, A. J., Morris, J., Shaw, L. M., Liu, E., Montine, T., Thomas, R. G., … Raj, B. A. (2025). Robust, fully-automated assessment of cerebral perivascular spaces and white matter lesions: A multicentre MRI longitudinal study of their evolution and association with risk of dementia and accelerated brain atrophy. eBioMedicine, 111, 105523. https://doi.org/10.1016/j.ebiom.2024.105523

Barisano, G., Montagne, A., Kisler, K., Schneider, J. A., Wardlaw, J. M., & Zlokovic, B. V. (2022). Blood–brain barrier link to human cognitive

impairment and Alzheimer's disease. Nature Cardiovascular Research, 1(2), Article 2. https://doi.org/10.1038/s44161-021-00014-4

Bateman RJ, Xiong C, Benzinger TLS, Fagan AM, Goate A, Fox NC, et al. Clinical and biomarker changes in dominantly inherited Alzheimer's disease. N Engl J Med. 2012 Aug 30;367(9):795–804.

Griffis, J. C., Metcalf, N. V., Corbetta, M., & Shulman, G. L. (2021). Lesion Quantification Toolkit: A MATLAB software tool for estimating grey matter damage and white matter disconnections in patients with focal brain lesions. NeuroImage: Clinical, 30, 102639. https://doi.org/10.1016/j.nicl.2021.102639

Jack, C. R., Wiste, H. J., Weigand, S. D., Knopman, D. S., Mielke, M. M., Vemuri, P., Lowe, V., Senjem, M. L., Gunter, J. L., Reyes, D., Machulda, M. M., Roberts, R., & Petersen, R. C. (2015). Different definitions of neurodegeneration produce similar amyloid/neurodegeneration biomarker group findings. Brain: A Journal of Neurology, 138(Pt 12), 3747–3759. https://doi.org/10.1093/brain/awv283

Kanbi, K. E., Tort-Colet, N., Benchenane, K., & Destexhe, A. (2023). EEG and computational aspects of how aging affects sleep slow waves (p. 2023.12.28.573547). bioRxiv. https://doi.org/10.1101/2023.12.28.573547

Lavanga, M., Stumme, J., Yalcinkaya, B. H., Fousek, J., Jockwitz, C., Sheheitli, H., Bittner, N., Hashemi, M., Petkoski, S., Caspers, S., & Jirsa, V. (2023). The virtual aging brain: Causal inference supports interhemispheric dedifferentiation in healthy aging. NeuroImage, 283, 120403. https://doi.org/10.1016/j.neuroimage.2023.120403

Lee, S., Viqar, F., Zimmerman, M. E., Narkhede, A., Tosto, G., Benzinger, T. L. S., Marcus, D. S., Fagan, A. M., Goate, A., Fox, N. C., Cairns, N. J., Holtzman, D. M., Buckles, V., Ghetti, B., McDade, E., Martins, R. N., Saykin, A. J., Masters, C. L., Ringman, J. M., … Network, for the D. I. A. (2016). White matter hyperintensities are a core feature of Alzheimer's disease: Evidence from the dominantly inherited Alzheimer network. Annals of Neurology, 79(6), 929–939. https://doi.org/10.1002/ana.24647

Leone, R., Geysen, S., Deco, G., & Kobeleva, X. (2024). Beyond Focal Lesions: Dynamical Network Effects of White Matter Hyperintensities. Human Brain Mapping, 45(17), e70081. https://doi.org/10.1002/hbm.70081

Leone, R., & Kobeleva, X. (2025). White matter hyperintensities contribute to early cortical thinning in addition to tau in aging. Neurobiology of Aging, 155, 66–77. https://doi.org/10.1016/j.neurobiolaging.2025.07.007

Leone R, Kobeleva X, Rowe B, Choupan J, Ringman JM, Barisano G. Alterations in MRI-visible perivascular spaces precede dementia diagnosis by 18 years in autosomal dominant Alzheimer's disease. Alzheimer's & Dementia. 2025;21(8):e70588.

Littau, J. L., Velilla, L., Hase, Y., Villalba-Moreno, N. D., Hagel, C., Drexler, D., Osorio Restrepo, S., Villegas, A., Lopera, F., Vargas, S., Glatzel, M., Krasemann, S., Quiroz, Y. T., Arboleda-Velasquez, J. F., Kalaria, R., & Sepulveda-Falla, D. (2022). Evidence of beta amyloid independent small vessel disease in familial Alzheimer's disease. Brain Pathology (Zurich, Switzerland), 32(6), e13097. https://doi.org/10.1111/bpa.13097

McDade, E., Kim, A., James, J., Sheu, L. K., Kuan, D. C.-H., Minhas, D., Gianaros, P. J., Ikonomovic, S., Lopez, O., Snitz, B., Price, J., Becker, J., Mathis, C., & Klunk, W. (2014). Cerebral perfusion alterations and cerebral amyloid in autosomal dominant Alzheimer disease. Neurology, 83(8), 710–717. https://doi.org/10.1212/WNL.0000000000000721

Quandt, F., Fischer, F., Schröder, J., Heinze, M., Lettow, I., Frey, B. M., Kessner, S. S., Schulz, M., Higgen, F. L., Cheng, B., Gerloff, C., & Thomalla, G. (2020). Higher hite matter hyperintensity lesion load is associated with reduced long-range functional connectivity. Brain Communications, 2(2), fcaa111. https://doi.org/10.1093/braincomms/fcaa111

Schoemaker, D., Zanon Zotin, M. C., Chen, K., Igwe, K. C., Vila-Castelar, C., Martinez, J., Baena, A., Fox-Fuller, J. T., Lopera, F., Reiman, E. M., Brickman, A. M., & Quiroz, Y. T. (2022). White matter hyperintensities are a prominent feature of autosomal dominant Alzheimer's disease that emerge prior to dementia. Alzheimer's Research & Therapy, 14(1), 89. https://doi.org/10.1186/s13195-022-01030-7

Schulz, M., Malherbe, C., Cheng, B., Thomalla, G., & Schlemm, E. (2021). Functional connectivity changes in cerebral small vessel disease—A systematic review of the resting-state MRI literature. BMC Medicine, 19, 103. https://doi.org/10.1186/s12916-021-01962-1

Tatulian, S. A. (2022). Challenges and hopes for Alzheimer's disease. Drug Discovery Today, 27(4), 1027–1043. https://doi.org/10.1016/j.drudis.2022.01.016

Ter Telgte, A., Van Leijsen, E. M. C., Wiegertjes, K., Klijn, C. J. M., Tuladhar, A. M., & De Leeuw, F.-E. (2018). Cerebral small vessel disease: From a focal to a global perspective. Nature Reviews Neurology, 14(7), 387–398. https://doi.org/10.1038/s41582-018-0014-y

Zhang, J., Chen, H., Wang, J., Huang, Q., Xu, X., Wang, W., Xu, W., Guan, Y., Liu, J., Wardlaw, J. M., Deng, Y., Xie, F., & Li, B. (2024). Linking white matter hyperintensities to regional cortical thinning, amyloid deposition, and synaptic density loss in Alzheimer's disease. Alzheimer's & Dementia, 20(6), 3931–3942. https://doi.org/10.1002/alz.13845

Zhang, Y., Ren, R., Yang, L., Zhang, H., Shi, Y., Okhravi, H. R., Vitiello, M. V., Sanford, L. D., & Tang, X. (2022). Sleep in Alzheimer's disease: A systematic review and meta-analysis of polysomnographic findings. Translational Psychiatry, 12(1), 136. https://doi.org/10.1038/s41398-022-01897-y

5. Statement on own contribution

Project 1 was designed by me in collaboration with Dr. Giuseppe Barisano (Instructor in Medicine, Stanford University). The data used for the evaluation was acquired by Prof. John Ringman (Clinical Professor of Neurology at the Memory and Aging Center at the Keck School of Medicine of University of Southern California) and the image pre-processing was performed by Dr. Barisano. I personally wrote the code for all statistical analyses. I made all figures, wrote the first draft of the manuscript, and provided revisions after reviewers' comments.

Project 2 was designed by me in collaboration with Prof. Dr. Med. Xenia Kobeleva (Head of Computational Neurology group at the Ruhr University Bochum). The raw data used for this study was generated by the Alzheimer's Disease Neuroimaging Initiative (ADNI, https://adni.loni.usc.edu/). I personally wrote all the code needed for the preprocessing of imaging data and independently performed all statistical analyses. I made all figures, wrote the first draft of the manuscript, and provided revisions after reviewers' comments.

Project 3 was designed by me in collaboration with Prof. Dr. Med. Xenia Kobeleva (Head of Computational Neurology group at the Ruhr University Bochum). The raw data used for this study was generated by the Alzheimer's Disease Neuroimaging Initiative (ADNI, https://adni.loni.usc.edu/). The image preprocessing was performed by a research assistant, Steven Geysen, under my and Prof. Kobeleva's supervision. I personally wrote all the code needed for building brain network models and for statistical analyses. I made all figures, wrote the first draft of the manuscript, and provided revisions after reviewers' comments.

The idea for Project 4 was originally designed by Dr. Jan Fousek (Junior Staff Scientist, CEITEC, Masaryk University Brno) and further developed by me, together with Gabriele di Antonio, Eleonora Lupi, and Marianna Angiolelli (PhD students, as part of the European Institute for Theoretical Neuroscience (EITN) 2023 Fall School). For this project, I wrote code for the brain network model and

for “virtually aging” the connectome, I performed statistical analyses needed for and made the following figures: Fig. 3, 4, Suppl. Figure 4.1, 4.2. I personally wrote the following parts of the first draft: introduction (full), methods (section: virtually aged structural connectome), results (section: network changes have spatially different impact), discussion (full) and reviewed and edited the full manuscript. I also provided many revisions after the reviewers’ comments.

In preparing this thesis, I used ChatGPT to improve the readability, logical flow and language of the manuscript. After using this tool, I reviewed and edited the relevant passages and take full responsibility for the content of the published dissertation.

I hereby confirm that my thesis complies with the Statement by the Executive Committee of the Deutsche Forschungsgemeinschaft (DFG, German Research Foundation) on the Influence of Generative Models of Text and Image Creation on Science and the Humanities and on the DFG’s Funding Activities.